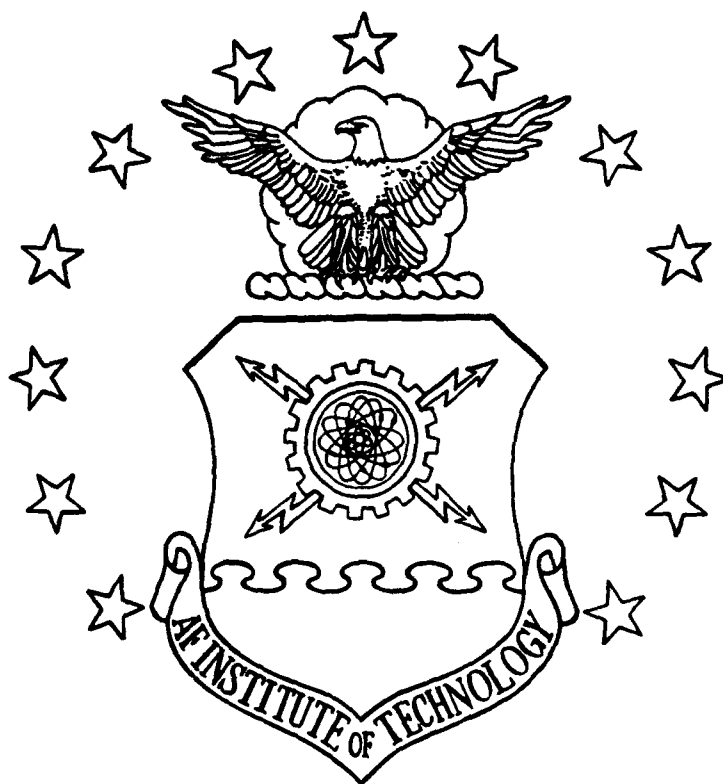


AD-A248 093



DTIC
ELECTE
APR 1 1992
S C D

NUMERICAL ANALYSIS OF PLASMA
TRANSPORT IN TANDEM VOLUME
MAGNETIC MULTICUSP
ION SOURCES

THESIS

Todd Roland Vitko
Captain, USAF

AFIT/GEP/ENP/92M-01

DISTRIBUTION STATEMENT A

Approved for public release;
Distribution Unlimited

92-08143



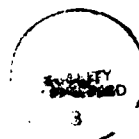
DEPARTMENT OF THE AIR FORCE
AIR UNIVERSITY
AIR FORCE INSTITUTE OF TECHNOLOGY

Wright-Patterson Air Force Base, Ohio

02 3 31 094

AFIT/GEP/ENP/92M-01

Accession For	
DTIC Tab	<input checked="checked" type="checkbox"/>
DTIC Tab	<input type="checkbox"/>
Unpublished	<input type="checkbox"/>
Justification	
By	
Distribution	
Availability Codes	
Dist	Avail and/or Special
A-1	



NUMERICAL ANALYSIS OF PLASMA
TRANSPORT IN TANDEM VOLUME
MAGNETIC MULTICUSP
ION SOURCES

THESIS

Todd Roland Vitko
Captain, USAF

AFIT/GEP/ENP/92M-01

Approved for public release; distribution unlimited.

AFIT/GEP/ENP/92M-01

NUMERICAL ANALYSIS OF PLASMA
TRANSPORT IN TANDEM VOLUME
MAGNETIC MULTICUSP
ION SOURCES

THESIS

Presented to the Faculty of the School of Engineering
of the Air Force Institute of Technology

Air University

In Partial Fulfillment of the
Requirements for the Degree of
Master of Science (Physics)

Todd Roland Vitko, B.S.

Captain, USAF

March, 1992

Approved for public release; distribution unlimited.

Preface

This thesis is a part of an on-going study of the modelling of man-made plasmas under Dr. William F. Bailey at the Air Force Institute of Technology. It is only a small part of the larger effort to which Jones [19], Hilbun [13], Seger [30], Bell [2], Minor [27], and many others have made important contributions.

Because this work is part of a larger on-going study, I have included in it two items that are not essential to this project itself, but should be of help as a reference to those who will come along later. First, the detailed derivation of the moment equations in Appendix A has been included to provide a ready reference to the topic. This appendix began life as an eight-page, handwritten summary in Dr. Bailey's introductory plasma physics course (which in turn was based on a similar derivation in Holt and Haskell [16:151-176]), and I hope that it will make the full circle back to being a class handout; it answers most of the questions that I had as I was trying to learn the material. The second example of extra detail is the taxonomy of reactions in a hydrogen ion source in Appendix B. Although the list there is not new in content, I hope that it will be handier in form than what I have found in most other reports, although I do heartily recommend Janev *et al.* [17] as a complete and thorough source for reaction data. Above all, I hope that others after me will be able to find some foundation here upon which to build, as I have built upon the foundation laid by others before me. To this end, more information about the model [35], not included in this thesis, is available from the physics department.

A special thanks goes of course to Dr. William F. Bailey, who has been a constant source of help and inspiration throughout this project. It would be impractical to make a bibliographical reference:

Bailey, W. F. Personal Interview.

because it would appear almost everywhere in this work, so I gratefully acknowledge his ubiquitous presence here. I especially appreciate his patience with a student who probably should have been a music major during a term that seemed much more like a race against the clock than a time for thoughtful pondering. This has been a challenging project for me, which has included learning from scratch FORTRAN, L^AT_EX, emacs, UNIX, ftp, *etc.*—not to mention learning a lot more about plasma physics in ion sources. Without Dr. Bailey's willingness to go back to basic principles time and time again when I didn't understand what was going on, it would have been impossible.

Finally, I owe another special thanks to my new wife, Ruth. Since our marriage she has known nothing other than AFIT widowhood, yet she has always remained patient and supportive, a help and an inspiration. With the thanks comes a promise that things will get better soon.

This thesis was typeset in L^AT_EX resident on AFIT's UNIX VAX computer 129.92.1.3, nicknamed "Galaxy." The model, the positive ion source code *pos*, ran on Galaxy in UNIX Fortran. The *MetaLib* library of FORTRAN routines resident on Galaxy provided the basis of the graphics modules that graphed the results of the model. The MacIntosh program *SuperPaint* drew the original figures, and the MacIntosh program *CricketGraph* redrew the experimental data plots from Johnson [18].

Todd Roland Vitko

Table of Contents

	Page
Preface	ii
Table of Contents	iv
List of Figures	viii
List of Tables	ix
List of Symbols	x
Abstract	xii
 I. Introduction	 1
1.1 Negative Ion Sources	3
1.1.1 Vapor Sources.	3
1.1.2 Surface Sources.	5
1.1.3 Volume Sources.	7
1.2 Problem Statement and Objectives	8
1.3 Overview of Thesis	10
1.4 The Model	11
1.5 Notation	15
 II. The Kinematics of Negative Ion Sources	 18
2.1 Plasma Production at the Cathode	19
2.2 Wall Losses	21
2.3 The Magnetic Filter Field	22
2.4 The Formation of Negative Ions	23
2.5 Summary of Kinematics	25

	Page
III. The Plasma Balance	27
3.1 Ionization	28
3.2 Recombination	29
3.3 The Plasma Balance	30
IV. The Behavior of the Unmodified Model	33
4.1 Replication of the Results in the Original Article	33
4.2 Plasma Density	37
4.3 Drift Velocity	41
4.4 Electron Temperature	42
4.5 Ion Temperature	44
4.6 Results of Multiple Runs of the Code (Irreproducible Results)	45
4.7 Summary of the Results of the Unmodified Model	46
V. The Boundary Energy Flux	49
5.1 Dependence of Density on the Left Initial Condition	49
5.2 Left Boundary Condition for the Temperature	51
5.3 Summary	52
VI. The Derivation of the Equations of the Model	54
6.1 Development of the Transport Equations	54
6.2 The Continuity Equation	55
6.3 The Momentum Equation	56
6.4 The Energy Equation	60
6.5 Differential Equations	60
6.6 Numerical Approach	61
6.7 Conclusion to Derivation of the Equations	61

	Page
VII. Inconsistencies in the Derivation of the Equations	62
7.1 Omitted Momentum Term in the Model	62
7.2 Extra Temperature Gradient in the Model	62
7.3 Extra Velocity Gradient in the Model	63
7.4 Attempts to Correct Inconsistencies in the Equations	64
7.5 Results of Modifications to Terms in the Equations	66
7.6 Conclusions from the Results of Modifications	67
VIII. Enhancements to the Model.	68
8.1 Electron Flux	68
8.2 The Electric Field	69
8.3 The Potential	73
8.4 The Electron Pressure	75
IX. Conclusions and Recommendations	77
9.1 Conclusions	77
9.2 Recommendations	79
9.2.1 Reproducible Results.	79
9.2.2 Boundary Conditions.	79
9.2.3 Stability Terms.	79
9.2.4 Wall Losses.	79
9.2.5 Energy Input.	79
9.2.6 Inclusion of a B-Field Term.	80
Appendix A. Derivation of the Moment Equations	81
A.1 Introduction	81
A.2 Definitions	81
A.3 The Generalized Equation of Change	84
A.4 The Zeroth Velocity Moment (The Continuity Equation)	91

	Page
A.5 The First Velocity Moment (The Momentum Equation)	92
A.6 The Second Velocity Moment (The Energy Equation)	101
Appendix B. Collision Processes in Hydrogen Ion Sources	107
B.1 Reactions That Release Electrons	107
B.2 Reactions That Capture Electrons	108
B.3 Reactions That Produce H^- Ions	108
B.4 Reactions That Destroy H^- Ions	109
B.5 Reactions That Produce H Atoms	109
B.6 Reactions That Destroy H Atoms	110
B.7 Reactions That Produce H_2 Molecules	110
B.8 Reactions That Destroy H_2 Molecules	111
B.9 Reactions That Release H^+ Ions	111
B.10 Reactions That Capture H^+ Ions	112
B.11 Reactions That Produce H_2^+ Ions	112
B.12 Reactions That Destroy H_2^+ Ions	112
B.13 Reactions That Produce H_3^+ Ions	113
B.14 Reactions That Destroy H_3^+ Ions	113
B.15 Elastic Scattering Reactions	113
B.16 Excitation and De-excitation Reactions	114
Appendix C. Glossary of Variables	115
C.1 Roman Letters	115
C.2 Greek and Hebrew Letters	117
Bibliography	118
Vita	121

List of Figures

Figure	Page
1. Neutral Beam Injection	4
2. Surface Source	5
3. Tandem Volume Source	7
4. Rod Filter Configuration of the Lawrence Berkeley Laboratory Volume Source . . .	9
5. Tandem Volume Source with Virtual Magnetic Filter	10
6. Block Diagram of the <i>pos</i> Code	13
7. The Heart of the Physics of the <i>pos</i> Code.	14
8. Overlap of Typical Cross Sections and the Electron Energy Distribution Function .	20
9. Collision History of an Idealized Primary Electron	21
10. Kinematics of a Tandem Volume Hydrogen Ion Source	26
11. Replication of the Results of the Model Presented in Glasser and Smith	34
12. Replication of the Node Positions in the Finite Elements Method as Functions of Time	35
13. Density, Drift Velocity, Electron Temperature, and Ion Temperature at the Outflow Boundary	36
14. Axial Variation of Plasma Density: Experimental Measurement <i>vs.</i> the Model . . .	38
15. Axial Variation of Electron Temperature: Experimental Measurement <i>vs.</i> the Model	43
16. Difference Between a One-Population and a Two-Population Model of the Electron Energy Distribution	44
17. Non-converging Run of the Model with Standard Parameters	47
18. Tandem Volume Source Geometry	57
19. Charged Particle Flux.	69
20. The Electric Field	72
21. Plasma Potential: Experiment <i>vs.</i> the Model	74
22. Electron Pressure (Energy Density): Experiment <i>vs.</i> the Model	76

List of Tables

Table	Page
1. The Seven Species in a Hydrogen Ion Source.	18
2. The Seven Reactions Used in the Numerical Model.	27
3. Comparison of Rates for Ionization Reactions 19 and 24	29
4. Reaction Rates for Representative Recombination Reactions	30
5. Variation of the Maximum Final Values of the Plasma Density with Changes to the Initial Values.	39
6. Irreproducible Results	46

List of Symbols

Symbol	Page
n	1
V_i^α	1
α	2
u_i^α	2
v''	18
α^*	18
e^{lary}	19
ϵ_{th}	19
e^{2ary}	19
ϵ_{beam}	20
ϵ_{kinet}	20
r_L	22
k_N	27
σ_N	27
T^e	42
T^i	44
$\Gamma_{z=0}^\epsilon$	49
Γ_0^ϵ	50
τ^e	50
ν^e	50
x^e	50
$P(x)$	50
ω_c^e	50
κ^α	50
η_j^α	57

Symbol	Page
$[\ell]$	62
$[m]$	62
$[t]$	62
Γ_i^e	68
j	70
E_i	73
Φ	73
p^e	75
$f^\alpha(\mathbf{v}, \mathbf{x}, t)$	81
v	82
Z	84
ξ	85
$\frac{d}{dt}$	92
δ_{ij}	93
A_j^α	94
A	96
$\Gamma(\zeta)$	97
ψ_{ij}^α	98
Π_{ij}^α	99
R_j^α	100

Abstract

A one-dimensional fluid model of plasma transport in tandem volume magnetic multicusp ion sources is explored. The model, the positive ion source code *pos*, by Glasser and Smith, calculates plasma density, drift velocity, electron temperature, and ion temperature in an ion source. The usefulness of the model is limited: (1) The plasma density trend runs opposite to experimental results, and electron temperatures are an order of magnitude higher than experimentally observed. (2) Simplification of the reaction chemistry leads to a plasma balance between ionization and outflow instead of the correct balance between ionization and recombination. (3) Wall losses are neglected. (4) There are inconsistencies in the derivations of some equations. (5) The final solution depends on the choice of the initial estimated solution. (6) Results of the model are not totally reproducible. (7) Numerical instabilities develop upon modification of terms or variation of initial conditions outside of a narrow range. Calculations of the plasma potential from the results of the model are qualitatively correct.

NUMERICAL ANALYSIS OF PLASMA TRANSPORT IN TANDEM VOLUME MAGNETIC MULTICUSP ION SOURCES

I. Introduction

The purpose of a neutral particle beam is to transfer energy from the source device onto a target. One of the primary proposed uses of neutral particle beams is use as a weapon, in which case the transfer of energy is designed to destroy the target, whether it be an incoming nuclear warhead or a hostile space platform. The other principal proposed use of neutral particle beams is for the injection of high-energy neutral particles into a tokamak¹, where the transfer of energy is designed to heat the plasma inside the tokamak to achieve thermonuclear fusion. Since interest in the use of particle beams as weapons has waned in favor of other options, this introduction will motivate the present study in terms of the fusion applications.

For a hydrogen plasma to achieve fusion, it must satisfy the Lawson condition:

$$\left. \begin{array}{ll} n\tau > 10^{16} & d-d \text{ reactions} \\ n\tau \geq 10^{14} & d-t \text{ reactions} \end{array} \right\} T > 10 \text{ keV} \quad (1)$$

with sufficiently high density n , confinement time τ , and temperature T [21:265]. One way to heat the plasma to achieve the Lawson condition is through radiofrequency radiation; another way is to inject particles at high velocity. The high directed velocity V_i^α of the injected particles of species α

¹From the Russian *tokamak*, an acronym for *toroidal'naya kamera s magnitnym polem* "toroidal chamber with a magnetic field." [28]

α is transformed (thermalized) to a random (thermal) velocity u_i^α through collisions with particles of the plasma. To make injection most efficient, a beam of neutral particles is injected.

Injecting neutral particles maintains the quasineutrality of the plasma and thus avoids driving thermal ions to the wall. However, because neutral particles are uncharged, they can't be accelerated by electric or magnetic fields. The solution to this impasse is to accelerate charged particles and then convert the accelerated particles into neutrals without significantly reducing their average velocity.

There is a choice between two types of charged particles to accelerate: positive ions or negative ions. Negative ions are the better choice for three reasons.

One advantage that negative ion beams have over positive ion beams is that the negative ion beams are more easily made uniform. For fusion applications, the injected beam should ideally be uniform. Without using a scheme to sort by mass, any beam of positive ions will contain the species H_2^+ and H_3^+ in addition to H^+ . Each species of positive ion has the same charge and therefore experiences the same force in a given electromagnetic field. However, because each species has a different mass, each will accelerate at a different rate and take a different length of time to traverse a given distance. So any unsorted beam of positive ions will have three components. On the other hand, H_2^- ions are unstable and spontaneously decay into their constituent components [18:35], so a negative ion beam contains only H^- ions and is thus uniform.

Another advantage of negative ion beams over positive ion beams is that it is easier to turn a negative ion beam into a stream of neutral particles than it is to transform a positive ion beam in the same way. Since in the negative ion beam the electrons are only loosely bound to the hydrogen atoms, they are relatively easy to strip off of the atoms. By contrast, it is relatively difficult to get a fast-moving positive ion to capture an electron. Moreover, the cross section for the reaction $H^+ + e \rightarrow H + h\nu$ decreases with increasing energy [19:1-2], so the more energy desired to be input

into the tokamak, the more difficult it will be to neutralize the positive ion beam that carries the energy.

A third advantage of negative ion beams over positive ion beams is that negative ion beams propagate more readily through the drift space between the negative ion source and the user device. To see why this is so, consider a beam of negative ions propagating through a low density gas. Some of the ions will collide with the atoms of the gas, producing positive ions and free electrons. Because the electrons have a much lower mass than the positive ions, the random velocities of the electrons will be higher than those of the ions, and the electrons will tend to leave the path of the negative ion beam sooner. The departing electrons leave behind the positive ions, which form a sheath of positive charge around the negative ion beam. This sheath of positive charge serves as a conduit for the negative ion beam. Thus the negative ion beam is said to be "self-focusing" [18:19].

Figure 1, from Johnson [18:20], shows a schematic diagram of how a negative ion beam could be used to heat a tokamak. Extraction electrodes extract the negative ions formed in the source and accelerate them towards an accelerator, which brings them to their maximum velocity. Before the negative ions enter the tokamak, they pass through a plasma neutralizer which strips the extra electrons, transforming the beam of negative ions into a beam of neutral particles (H atoms). A magnetic field, located just past the neutralizer, deflects any negative ions remaining in the beam into an ion dump.

1.1 Negative Ion Sources

The majority of negative ion sources may be classified into three categories: vapor sources, surface sources, and volume sources.

1.1.1 Vapor Sources. A *vapor source* transforms a beam of positive ions into a beam of negative ions by sending them through a vapor of alkali metal atoms. Because the alkali metals have an electron weakly bound in the outermost shell, this electron is easily stripped. After two captures, a positive ion in the incident beam is transformed into a negative ion in the exiting beam.

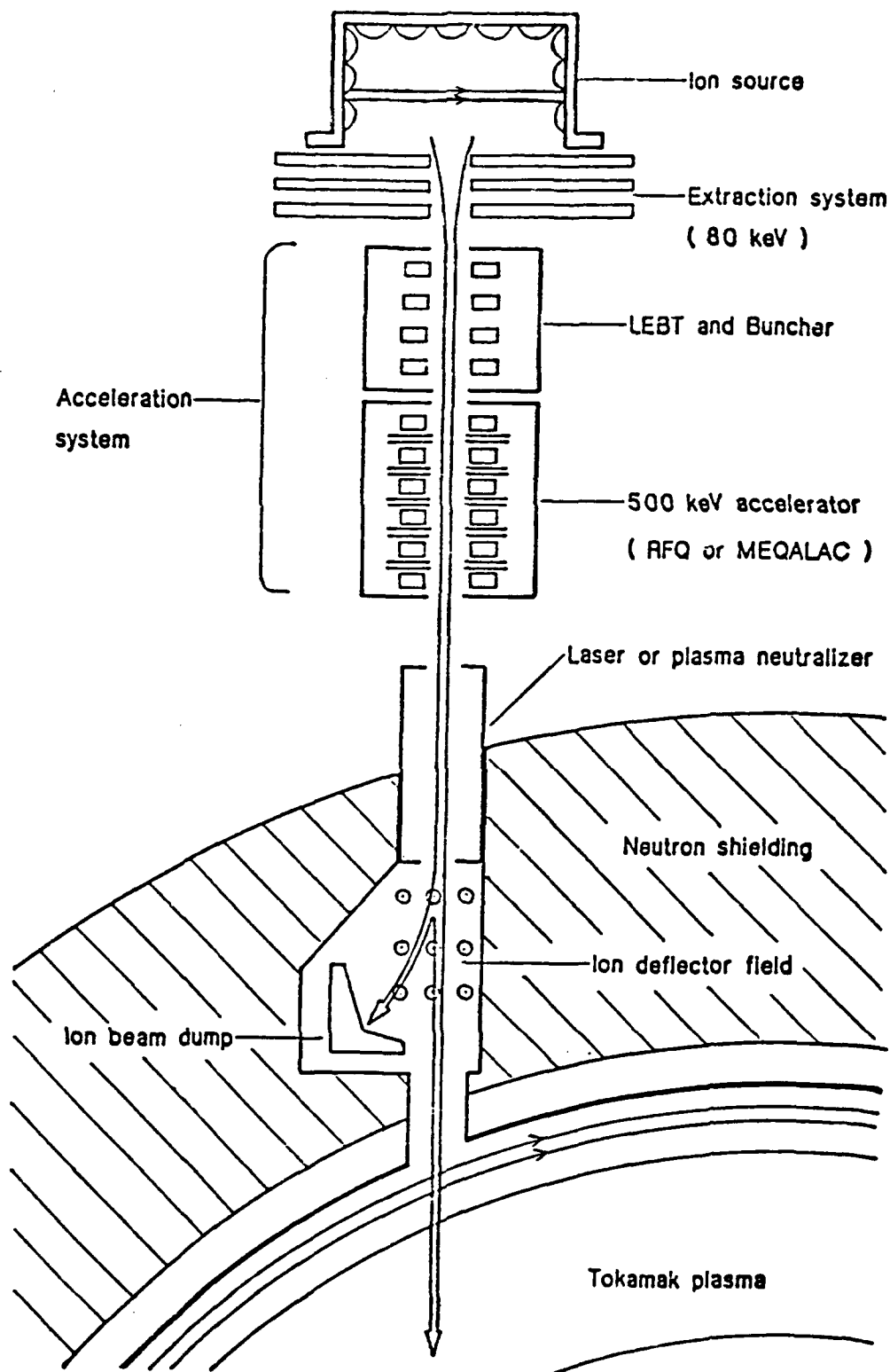


Figure 1. Neutral Beam Injection (from Johnson [18:20]).

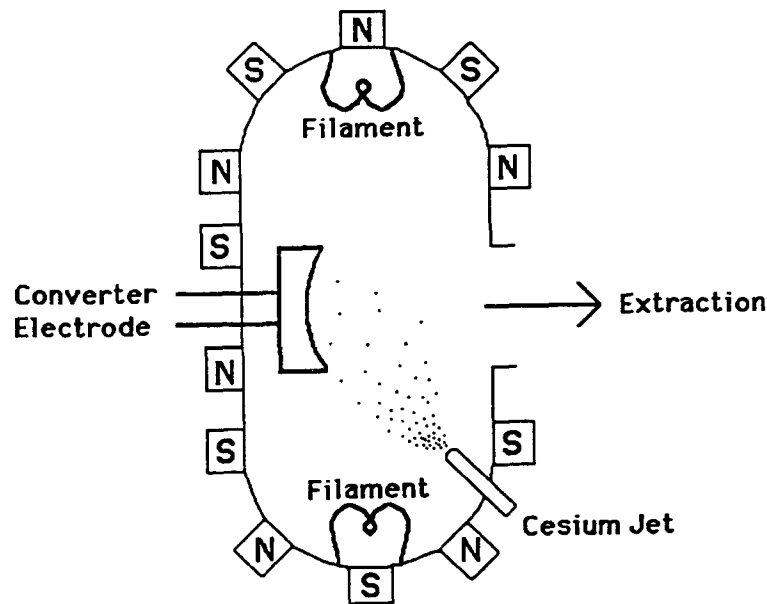


Figure 2. Surface Source, after Leung and Ehlers [22:804].

However, there are several problems with this kind of negative ion source. First, after the incident ion captures its first electron and before it captures its second, it is a neutral atom. There will be a space in the vapor where the traversing beam will be made up mostly of neutral particles. This neutral beam will diverge before the second capture turns the neutral atoms into negative ions [18:21-22]. A second problem with the vapor source is high-voltage breakdown [18:22]. The beam of positive ions is by nature an electrical current, and the alkali vapor is a metal. If the currents are too high, the metal vapor can "short out" the current and production will break down. The third problem is that collisions with alkali atoms will impart momentum so that some of them are carried along with the exiting negative particle beam. These impurities can contaminate the plasma in the tokamak [18:22].

1.1.2 Surface Sources. A second source of negative ions is the cesiated surface source. In this source, negative ions are created on the surface of a cesiated converter electrode. Figure 2 shows a simplified schematic of the classical surface source of Leung and Ehlers [22:804].

In the surface source, electrons emitted from hot filaments form a plasma in the vacuum vessel. A converter electrode in the center of the vessel maintains a large negative potential (~ 200 V) on its curved front face and a small positive potential (~ 40 V) on its sides and support column. A jet injects cesium vapor onto the surface of the converter electrode. Attracted by the negative converter potential, the positive ions in the plasma accelerate toward it until they impact the converter surface. Through a process that is not well understood, the interaction of hydrogen and cesium ions on the surface produces negative hydrogen ions. These newborn negative ions are now repelled by the same converter potential that attracted them as positive ions. Since the surface of the converter electrode is curved, the ions tend to accelerate in a direction perpendicular to the center of the converter electrode and are thus "focused" geometrically onto the extractor electrode. Before reaching the extractor electrode, the ions encounter a relatively weak (~ 80 Gauss) magnetic filter field which returns the electrons to the plasma while deflecting the negative ions only slightly.

There are also several problems associated with the surface converter source. First, because the velocities imparted to the negative ions accelerating away from the converter electrode vary significantly, the beam of negative ions is strongly divergent [18:22]. Second, running the converter electrode potential requires an additional supply of power [18:22]. Third, the relatively large amounts of cesium deposited onto the converter surface and onto the walls of the vessel create a hazard to the extraction and acceleration system [12:384].

The primary reaction in the surface source depends on a synergistic interaction between the cesium and the hydrogen. The H^- production by bombardment with both cesium and hydrogen is much greater than the production due to either process alone [31:432]. Yet even though the primary process is at the surface of the converter electrode, no less than 25% of the H^- ions are produced, not at the surface of the converter electrode, but in the volume of the device [18:23]. With such a high production in the volume of a device that is not optimized for volume production,

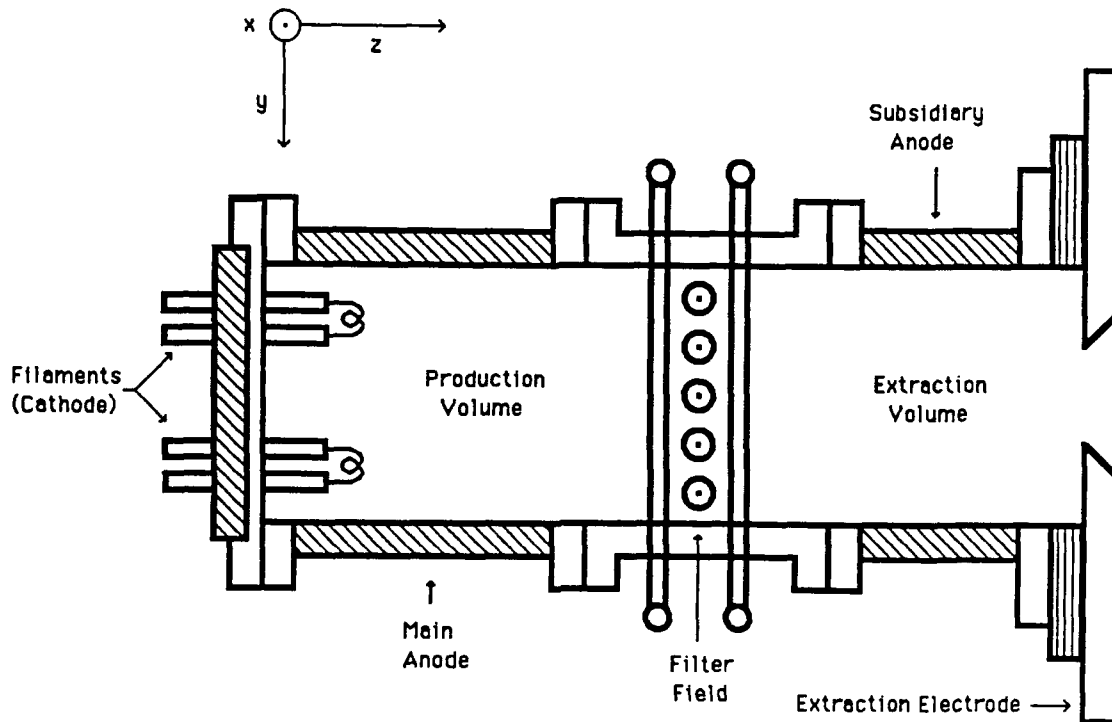


Figure 3. Schematic Diagram of a Tandem Volume Source, after Glasser and Smith [9:411].

the natural inclination would be to dispense with the surface converter and optimize the volume production itself, thus creating a *volume source*.

1.1.3 Volume Sources. The source of interest to this study is the tandem volume source, or *multipole source*, depicted in Figure 3. A volume source generally consists of a cylindrical vacuum vessel, of approximately 20 to 30 cm in length and 20 to 30 cm in diameter, divided into two tandem chambers by a magnetic filter field. A multipolar array of permanent magnets surround the vessel to conceal the walls of the vessel from the plasma, limiting losses of plasma to the wall to the cusps between magnets [20]. These magnets typically have strengths of about 3.6 kilogauss (*kG*) [23:56]. The inner chamber, called the *source*, *production*, or *driver* region, contains hot filaments that emit fast primary electrons (the *discharge*). These filaments form the cathode of the device, and the walls form the anode. Typical discharge parameters are ~ 80 volts potential and ~ 10 amps of current [8:1425], but the JET-type positive ion source at the Culham laboratory in England uses discharge

currents of ~ 1000 amps to optimize H^- production [18:24]. The fast primary electrons from the discharge ionize the neutral gas in the source chamber, forming a plasma. The magnetic filter field confines the fast electrons to the source region but allows cold secondary electrons to diffuse to the second chamber [8:1423], which is called the *extraction region* because extraction electrodes at the far end can extract ions from it. The volume source can produce either negative ions or positive ions, depending on the gas mixture used and whether the extraction electrode supplies a positive or negative potential relative to the plasma potential.

There are two means of generating the magnetic filter field [18:61]. Figure 4 shows a photograph of the tandem volume source at Lawrence Berkeley Laboratory, taken from Stevens [33:272]. This source is an example of the "rod-filter" configuration, where magnetic rods physically intrude across the interior of the source to generate the magnetic filter field. The other means of generating the filter field is by rearranging the multipolar array of magnets on the outside of the vessel to extend a pair of cusps so that they cross the volume, creating a "virtual" magnetic filter field. Figure 5, from McAdams [26:303], shows a line drawing of a tandem volume source with a virtual magnetic filter.

Chapter II discusses the kinematics of tandem volume ion sources in greater detail.

1.2 Problem Statement and Objectives

The purpose of this thesis is to investigate the utility of a one-dimensional plasma fluid model in the study of tandem volume magnetic multicusp ion sources. The objectives were: (1) Investigate the kinematics of hydrogen ion sources and apply what was learned to understand the model under study. (2) Determine the origin and the validity of the equations on which the model is based. (3) Examine the results of the model, especially the effect of the magnetic filter field. (4) Compare the results from the model to what would be expected theoretically and experimentally from a positive ion source. (5) Where the results differ from what would be expected, propose a reason

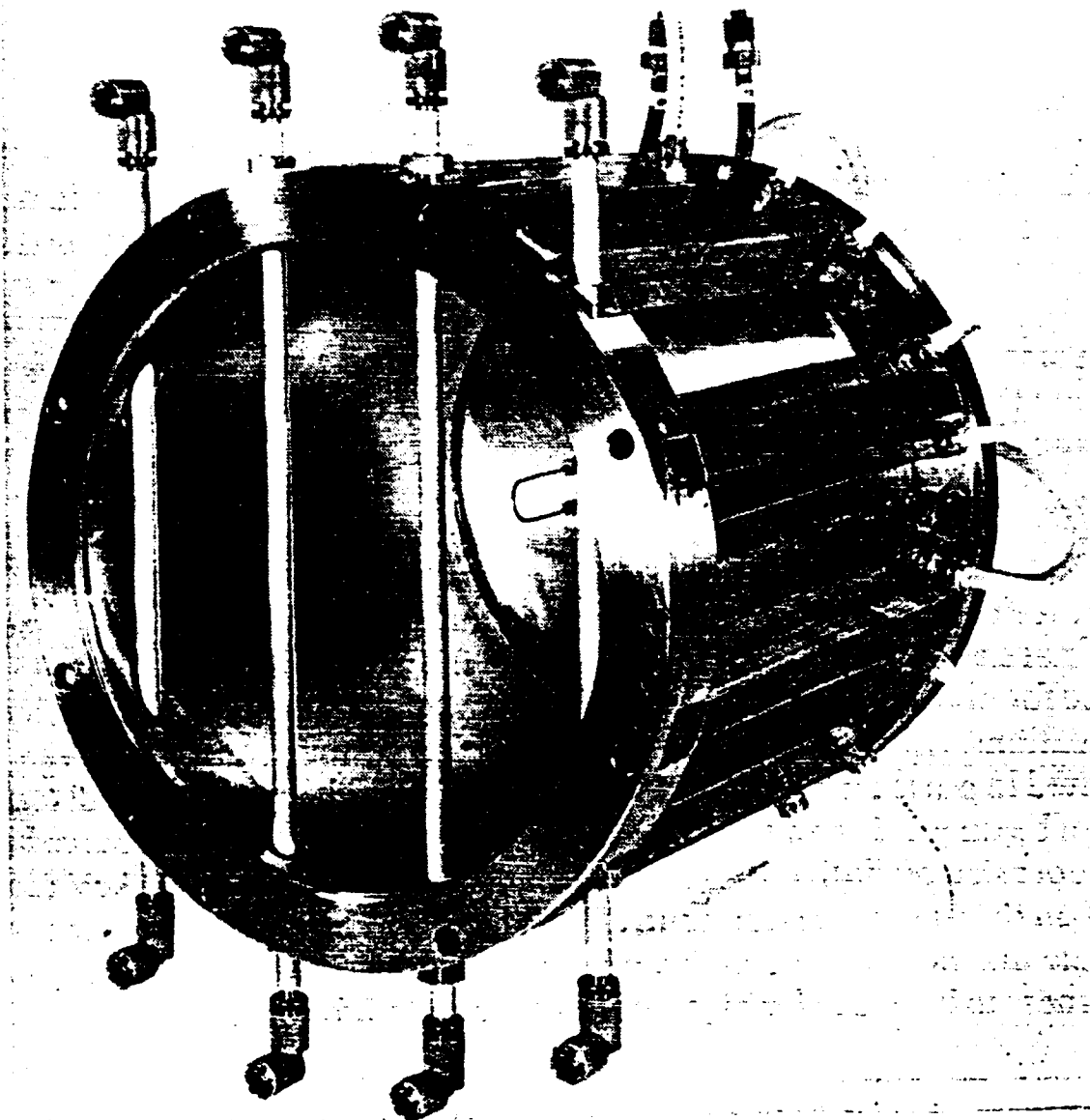


Figure 4. Photograph of the Production Chamber of the Lawrence Berkeley Laboratory Volume Source, Showing a Rod Filter Configuration (from Stevens) [33:272].

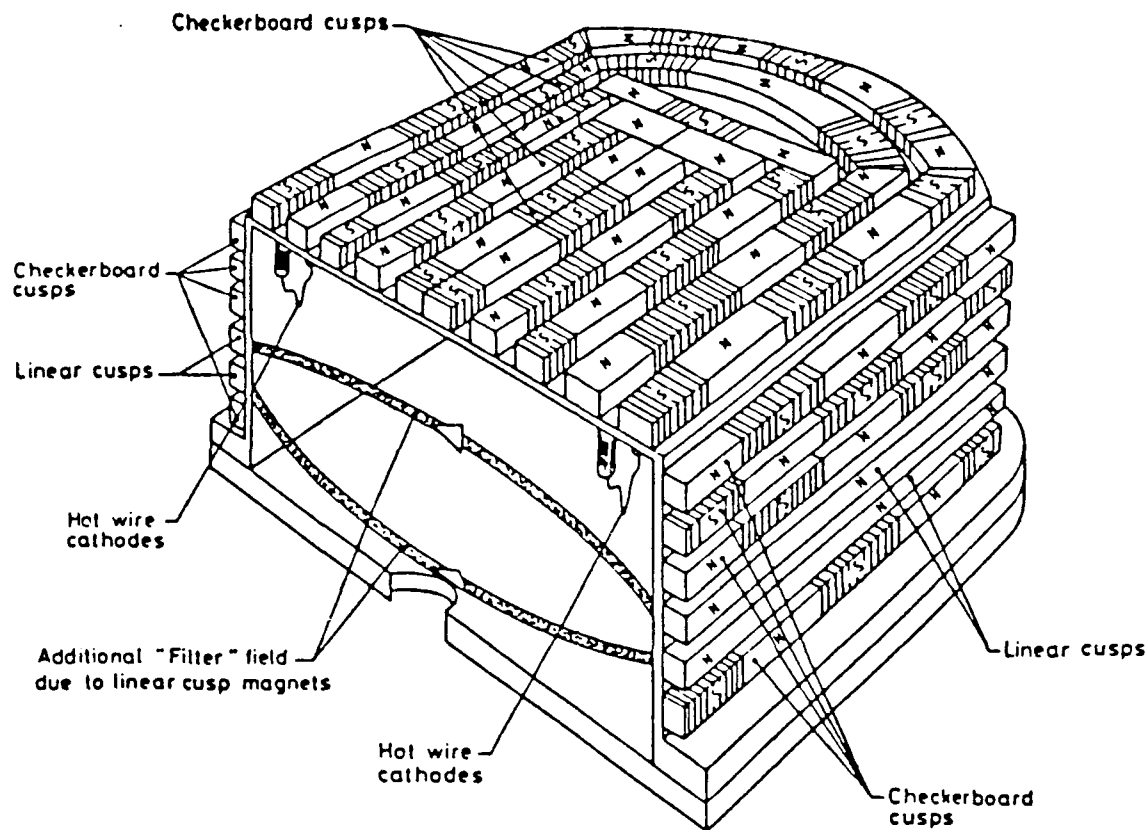


Figure 5. Line Drawing of Tandem Volume Source with a Virtual Magnetic Filter Field (from McAdams) [26:303].

why. (6) Propose modifications to the model to bring it more in line with what is expected. (7) Implement modifications to the model and verify that the results from the modified version are more in line with the expected results.

1.3 Overview of Thesis

The organization of this thesis differs somewhat from what is traditional. Because this investigation is modular, consisting of several independent but interrelated topics, the traditional organization into chapters for theory, implementation, results, and conclusions would fragment the topics discussed. To avoid this fragmentation, this thesis allocates a chapter to each topic so as to group together the theory, implementation, results, and conclusions that are appropriate for

each topic (some topics are more heavily weighted to one category than another). This introductory chapter concludes with a short presentation of the salient features of the model and an explanation of the notation used in this thesis. Chapter II contains a brief general and theoretical exposition of the kinematics of hydrogen ion sources. Chapter III applies the kinematics discussed in Chapter II to evaluate the plasma balance in the model. Chapter IV examines the results of the model's published "test case" [9:422-423] and identifies behavior not mentioned in the original article. Chapter V attempts to explain some of the behavior discussed in Chapter IV in terms of the numerical processes occurring in the model. Chapter VI summarizes the development of the equations used in the model. Chapter VII identifies some apparent inconsistencies in the derivation outlined in Chapter VI and presents the results of modifications to the model designed to remove the inconsistencies. Chapter VIII describes four enhancements to the model. The chapter for overall conclusions and recommendations for further study comes in the usual position. The mathematical details of the derivation of the moment equations discussed in Chapter VI are relegated to Appendix A. Appendix B gives one possible taxonomy of reactions in a hydrogen plasma, based on the presentation in Smith and Glasser [32:393-394]. Appendix C is a glossary of symbols.

1.4 The Model

The model used in this investigation is the positive ion source code *pos*, developed in 1987 by Alan H. Glasser and Kenneth Smith at the Los Alamos National Laboratory, which applies fluid equations to solve for the time evolution of plasma density, drift velocity, electron temperature, and ion temperature in a positive ion source. It is one step in a program to develop a "realistic computer model of H^- ion sources" [9:410]. Although the physical setup of the negative ion source is identical to that of the positive ion source, the number of reacting species and the equation set that the model uses to describe the positive ion source is smaller than that required to model a negative ion source. Specifically, the model considers only four interacting species: e , H^+ , H , and H_2 . Thus it does not model a negative ion source because it excludes H^- ions altogether.

The *pos* code can be described as a physics “chassis” built around the numerical engine *dirk2*. The *dirk2* code, written by Neil Carlson and Keith Miller of the University of California at Berkeley in 1984, solves a system of first-order, linearly-implicit, ordinary differential equations of the form

$$A(y) \frac{dy}{dt} = g(y)$$

using a diagonally implicit Runge-Kutta method of 2nd order and Miller’s method of moving finite elements [5]. The *pos* code establishes the physics and casts the differential equations in a form that *dirk2* can solve.

As FORTRAN code, the *pos* code is well-written, well-documented, and portable. Although the code was written for a Cray supercomputer, it compiled without error in UNIX FORTRAN on the UNIX VAX “Galaxy.” Even the extremely sensitive VMS FORTRAN compiler on the VMS VAX “Hercules” detected only one small error during compilation: the local counter variable *ireac* in the module *chrates* has the same name as the array *ireac(nreac)* in the *common* block *ksrates*. This *common* block is available to the *chrates* module, but the array *ireac(nreac)* is not used in *chrates*.

Figure 6 shows a block diagram of the subroutines of the *pos* code. These subroutines may be divided into two groups. The first group consists of those subroutines which are either provided with the *dirk2* code or required by it. The *dirk2* code provides the routines *dirk2*, *drkpfl*, *bce*, and *intrp*, and it requires the user to supply the routines *resdl*, *jac*, *yprime*, *linsol*, *norm*, *setbus*, *solchk*, and *step*. Also numbered among this first group are the subroutines *vdec*, *vsol*, *scopy*, *solbt*, *decbt*, *amazaf*, *display*, *timer*, and *exit*, which are required by *norm*, *linsol*, and *jac*. The second group of subroutines are those which establish the physics of the ion source. This second group is comprised of those subroutines that either input and initialize the physical parameters (*rates*, *xsecn*, and *init*) or actually compute the physics (*arrays*, *fluxes*, *brag*, *chem*, *chrates*, *reloss*, and *crosec*). This thesis deals almost exclusively with the second group of subroutines, which are diagrammed separately in Figure 7.

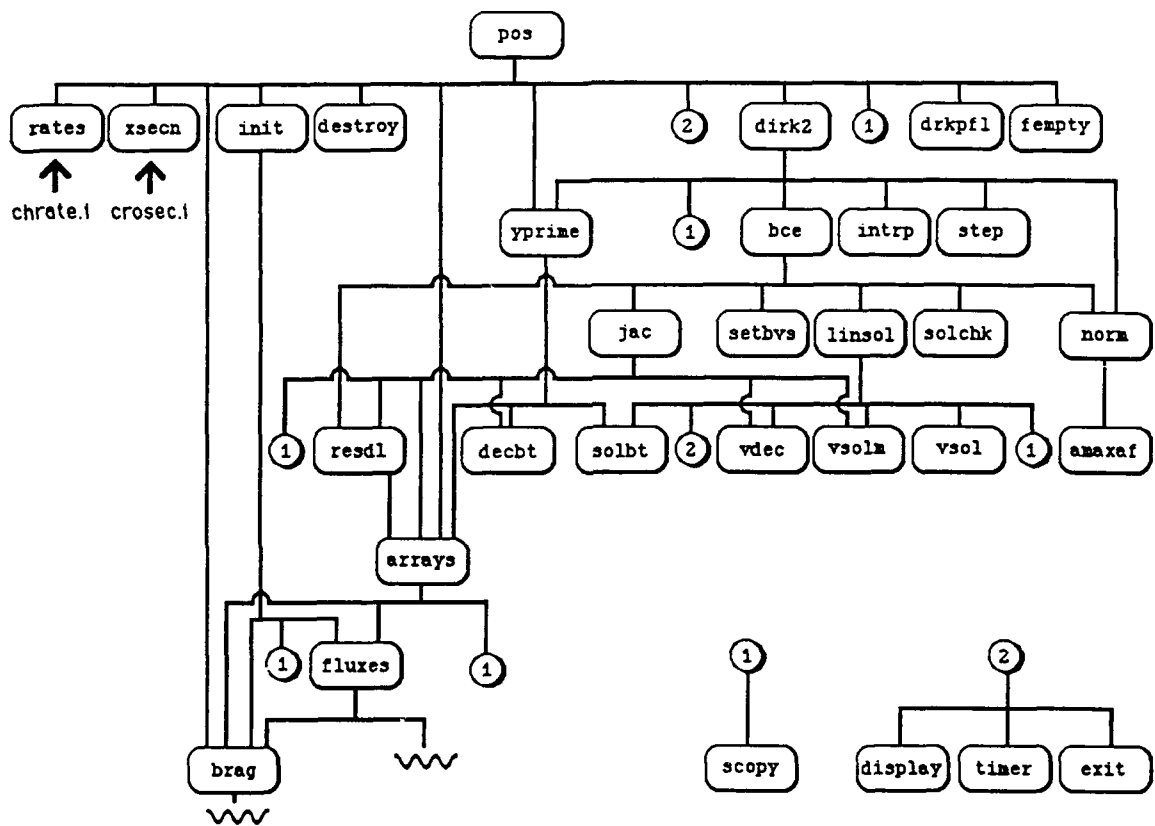


Figure 6. Block Diagram of the *pos* Code, Showing Subroutine Calls.

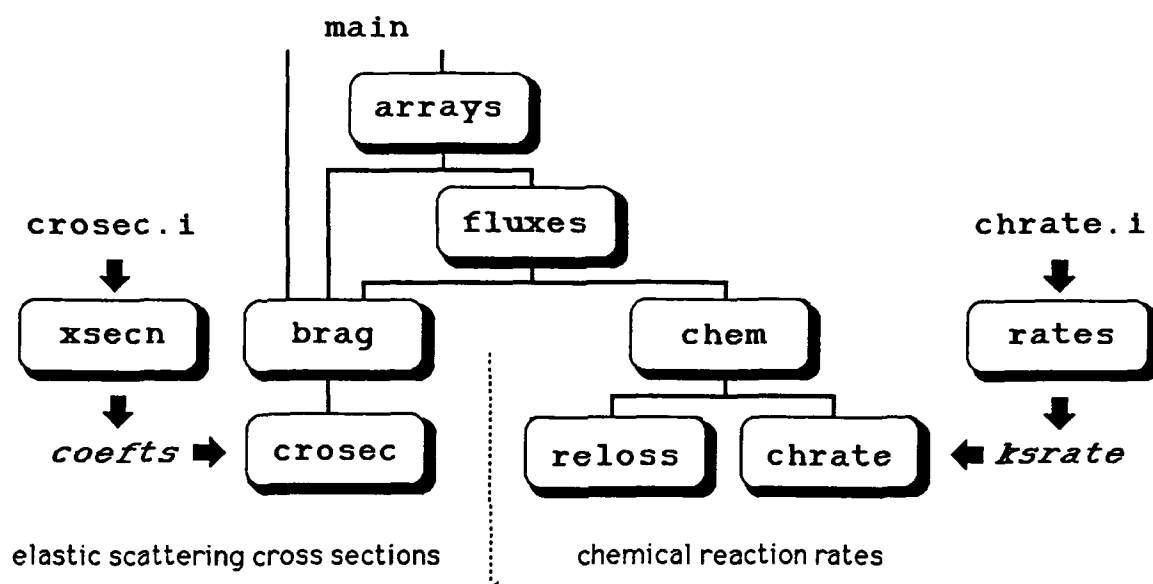


Figure 7. The Heart of the Physics of the *pos* Code.

The *main* module of *pos* reads the initial conditions stored in the file *pos.in*, defines the initial parameters required by *dirk2*, initializes and scales the variables, and writes the output to the file *pos.out*. It also contains a loop of subroutine calls that accomplish the actual calculation.

As part of the process of initialization, *pos* calls the module *rates*, a subroutine that reads the chemical reaction rate data stored in the file *chrates.i* and stores it into the *common* block *ksrates*, and the module *xsecn*, a subroutine that reads the elastic cross section data stored in the file *crosec.i* and stores it into the *common* block *coefts*. These two input files begin two parallel calculations, one for the chemical reaction rates, the other for the elastic cross sections, which converge in the module *fluxes*.

The module *chrates* is a subroutine that uses the variables stored in the *common* block *ksrates* to calculate the reaction rates for the chemical reactions modelled by *pos*. It stores these reaction rates in the variable array *rates* to pass to the module *chem*.

The parallel module *crosec* is a subroutine that uses the variables stored in the *common* block *coefst* to calculate the elastic scattering cross sections with neutral particles. It passes these cross sections to the module *brag* in the variable array *sigma*.

The *chem* module uses the reaction rates it receives from the *chrates* to calculate the collisional source terms S , R^{en} , R^{in} , Q^{en} , and Q^{in} , which it stores in positions 1 through 5 of the variable array *sc*, which it passes to *fluxes*.

The parallel calculation in the *brag* module uses the elastic scattering cross sections it receives from the *crosec* a number of plasma parameters and coefficients, which are stored in arrays in the *common* block *coef*, which is available to the module *fluxes*.

The two parallel streams of calculations now converge in the module *fluxes*. The subroutine *fluxes* uses the collisional source terms from *chem* and the plasma parameters and transport coefficients from *brag* to calculate convective and dissipative flux and source terms that are components of the fluid equations.

The *fluxes* module feeds these terms to the module *arrays*, which is a subroutine that builds the arrays that will be manipulated by the matrix arithmetic modules and eventually solved by *dirk2*.

All of the subroutines are further documented in the source code [5], in the original article [9], or in an additional report [35].

1.5 Notation

Notation is a difficult subject in plasma physics. There are too few letters in the Latin and Greek alphabets to denote the many different quantities that can be defined. Moreover, notation is not quite standard, and sources differ considerably. This thesis attempts to fulfill the (not always consistent) twin goals of (1) using notation that is widely recognized and (2) using the same representation throughout for any given quantity.

This thesis uses indicial notation throughout. On the few occasions where a vector is not written with indices, it is put into bold type: \mathbf{H} , \mathbf{V}_\perp^α . Instead of the Greek letters α and β that Braginskii uses for indices [3:205], this thesis uses the Latin letters i , j , and k as in Holt and Haskell [16] and in Golant [10]. Each index represents the principal coordinate directions x , y , and z . The ion source geometry, depicted in Figure 3, defines these principal coordinate directions. Moving from the production region to the extraction region along the axis of the ion source defines the positive z direction, with zero at the filament end. The positive direction of the magnetic filter field defines the positive direction of the x axis. The right-hand rule determines the positive sense of the y axis.

Subscripts are reserved for (1) vector indices and (2) integration bin numbers. Thus v_i denotes a component of velocity in the i^{th} direction, and n_j the plasma density in the j^{th} integration bin. The context makes clear which convention is which.

To avoid confusion with the subscripts for indices and integration bin numbers, species designations are superscripts. In the two-fluid derivations, i designates ions and e electrons. Otherwise, species are designated with their chemical identifications, e , H^- , H , H_2 , H^+ , H_2^+ , and H_3^+ . Thus n^H is the density of hydrogen atoms, V_z^i the component of average ion velocity in the z direction, and T^e the electron temperature. Instead of the Latin letter a that Braginskii uses [3:205] or the Latin letter j that Glasser and Smith use [9:412] to designate a general (charged) species, this thesis uses the Greek letter α in accordance with Krall and Trivelpiece [21:79] and Golant [10]. Thus n^α is the density of particles of species α . As in Golant [10:315], the Greek letter β designates a second general (charged) species: for example, the general momentum exchange term $\pm R^{\alpha\beta}$ represents the momentum transferred from ions to electrons, $+R^{ie}$, in the ion equation (where α represents species i , so β represents the *other* charged species e), but it represents the momentum transferred from electrons to ions $-R^{ei}$ in the electron equation (where the general charged species α is e , and the other charged species β becomes i).

Unfortunately, superscript species designations look confusingly like standard notation for exponents (which are seldom used in this thesis). To mitigate confusion where it could arise, exponents are written outside of parentheses. Thus the square of the velocity vector would be $(\mathbf{v})^2$. However, in keeping strictly with indicial notation, this thesis uses the notation $v_i v_i$ instead of $(\mathbf{v})^2$ whenever possible.

Since reaction rates and cross sections are never subscripted with integration bin numbers or vector directions, the chemical reaction numbers in Appendix B are written as subscripts. The Hebrew letter \aleph (aleph) denotes the general reaction. Thus k_{19} designates the reaction rate for Reaction 19 and σ_{\aleph} the cross section for Reaction \aleph .

For clarity, partial derivatives are written out in full, not abbreviated with commas. Hence, the time derivative of the mean velocity in the i^{th} direction is $\frac{\partial V_i^\alpha}{\partial t}$, not $V_{i,t}^\alpha$.

Lastly, Braginskii denotes a cross product with square brackets, $[\mathbf{vB}]_\alpha$ [3:205]. This thesis uses the indicial convention for the alternating unit tensor defined in Appendix A, $\epsilon_{ijk} v_j B_k$, but as a concession to Braginskii, all cross products will also be enclosed in brackets for clarity: $[\epsilon_{ijk} v_j B_k]$.

Appendix C summarizes the nomenclature used in this thesis.

II. The Kinematics of Negative Ion Sources

In the hydrogen plasma in the ion source, there are seven interacting species, which are listed in Table 1.

	mass →			
charge	e	H^-		
↓		H	H_2	
		H^+	H_2^+	H_3^+

Table 1. The Seven Species in a Hydrogen Ion Source.

There are 28 possible pairwise interactions among the seven species. In addition, each pairwise interaction can in general generate several different possible combinations of reaction products—the more subatomic components in the reactants, the greater the possible variety of products of a given interaction. Moreover, all of the reactant species except H^+ and e have internal energy states [34:15], such as the vibrationally excited states $H_2(4 \leq v'' \leq 11)$ of H_2 or the electronically excited state $H^*(2p)$ of H . The symbol v'' denotes a vibrationally excited state, and the symbol α^* denotes an electronically excited state of species α . In calculating the reaction chemistry, most of the excited states must be treated as separate particles because the cross sections, and thus the chemical reaction rates, differ from those of the unexcited particles [34:17]. All things considered, the taxonomy of reactions in even the simplest hydrogen plasma is quite complex. Appendix B contains basic lists, after Smith and Glasser [32:393-394], of the principal reactions that form and destroy the seven species under consideration.

Although tandem magnetic multicusp ion sources were originally developed as positive ion sources [18:23], with the magnetic filter field serving to alter the species ratio ($H^+:H_2^+:H_3^+$) of the positive ions extracted [25:1], currently most are constructed to optimize the production of H^- ions.

The kinematics of the tandem ion source (and hence the production of H^- ions) are determined to a large extent by (1) the production of plasma through ionization at the hot filament

cathode, (2) the losses of plasma (a) to the walls of the chamber, (b) through recombination in the volume, and (c) out the extraction end of the device, and (3) the properties of diffusion through the magnetic filter field.

2.1 Plasma Production at the Cathode

To provide the material with which to form a plasma, a gas jet admits neutral hydrogen gas into the chamber. A cathode consisting of hot filaments ($\sim 100\text{ eV}$) supplies energy to the gas in the source chamber in the form of fast electrons emitted from the filaments. These fast primary electrons, e^{1ary} , form what is probably an offset ("drifting") Maxwellian distribution [18:28] of energies and velocities around the injection potential of the filaments. The primary electrons ionize molecules of neutral hydrogen gas, losing energy in each collision until they cross ϵ_{th} , the threshold energy for the cross section for ionization, where they join a Maxwellian population of thermal secondary electrons, e^{2ary} . Because the fast primary electrons give up their energies to the discharge and join the population of secondary electrons much more rapidly than the secondary electrons are lost to the walls or are extracted out of the device, the population of thermal secondary electrons grows to be several orders of magnitude larger than the population of primary electrons.

Ionization is not the only process that redistributes the energy of the primary electrons. Electron excitation and vibrational excitation also redistribute energy, and each has its associated cross section. Figure 8 shows a schematic diagram of the interaction of the electron energy distribution function (EEDF) with the various cross sections. This diagram shows that primary electrons accomplish most of the ionization of the neutral gas to form a plasma.

Primary electrons may have energies up to the discharge potential [18:28], which is commonly of the order of 100 V [4:379]. The higher the energy of the primary electron, the more electron-ion pairs it can produce before it joins the population of thermal electrons [24:365]. Suppose that a narrow beam of electrons impinges on a plasma so that the incident electrons have a narrow range

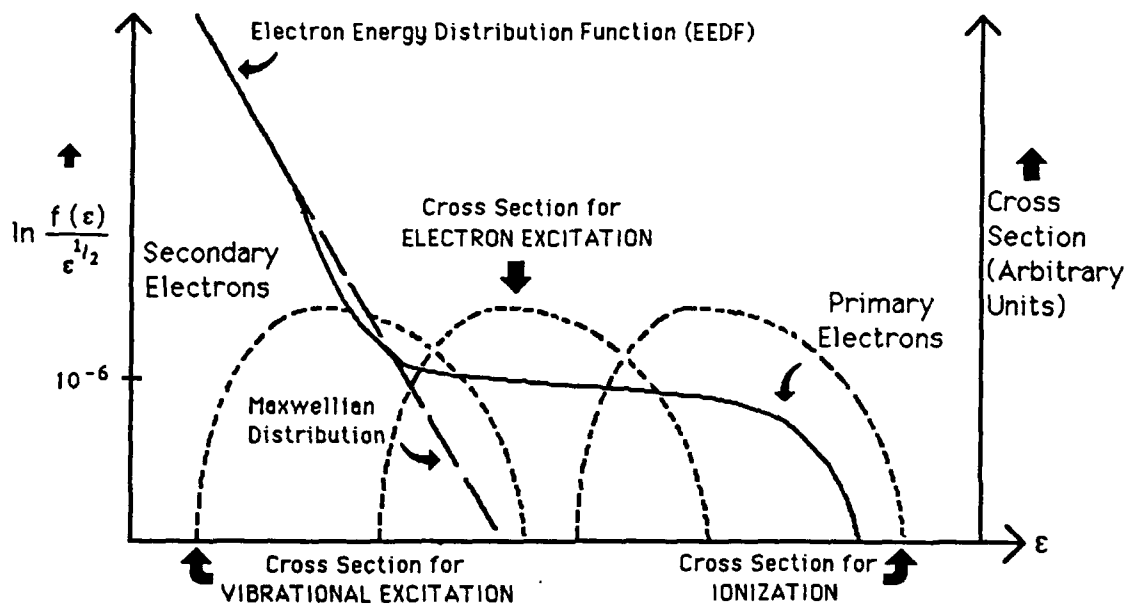


Figure 8. Schematic Diagram of the Relative Range of Overlap of Typical Cross Sections and the Electron Energy Distribution Function.

of energies centered around ϵ_{beam} , as depicted in Figure 9. Then an electron in the beam will lose energy through collisions, mainly with neutral particles. Often it will ionize these particles in the course of the interaction. The greatest possible number of secondary electrons would be produced if (1) every interaction caused an ionization and (2) each of the secondary electrons thus produced were born at rest (a, b, c, d, e, f, and g in the diagram). In this case, all of the energy lost by the primary electron goes into breaking the electron bond and none is carried away by the secondary electron as kinetic energy. Thus the primary electron would produce the greatest number of electron-ion pairs before its energy falls below the threshold energy ϵ_{th} , at which the collision cross section effectively goes to zero. A 100 eV primary electron could accomplish seven "generations" of 13.58 eV ionizations before falling below the 13.58 eV threshold energy. On the other hand, if the ionized secondary electrons were born with a substantial kinetic energy ϵ_{kinet} (α , β , γ , and δ in the diagram), then the number of ionizations that the primary electron could accomplish before joining the population of thermal secondary electrons would be much smaller (≈ 4 for $\epsilon_{\text{kinet}} \approx 10$ eV). The truth apparently lies somewhere between the two extremes: modeling by

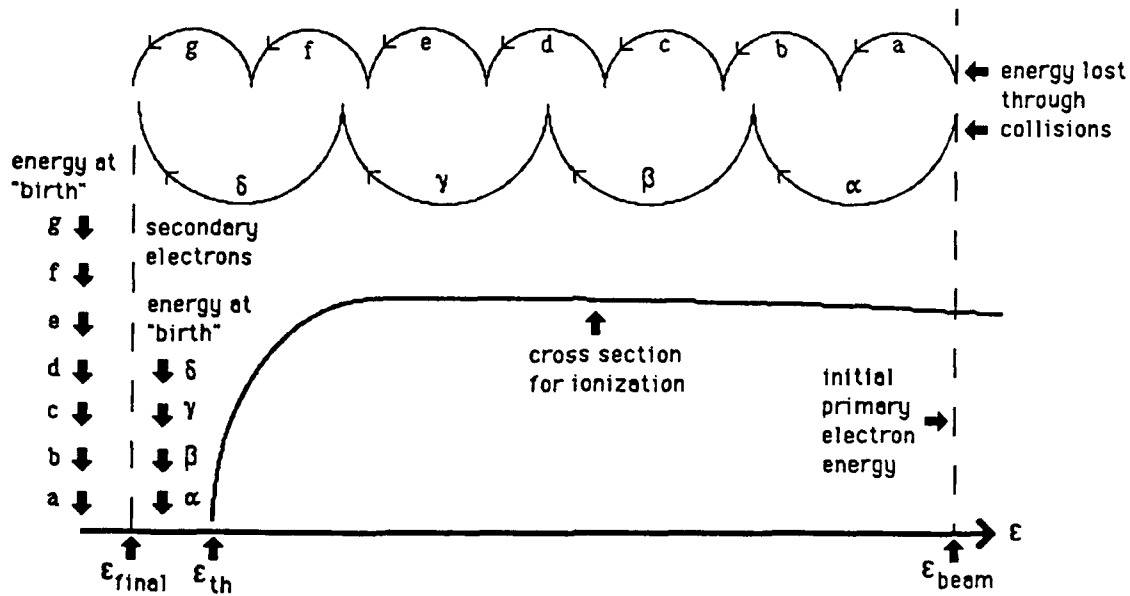


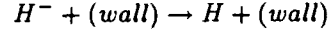
Figure 9. Schematic Diagram of the Collision History of an Idealized Primary Electron.

Chan, Burrell, and Cooper shows that the first generation of primary electrons accomplish roughly half of the ionizations [7:6124], yet it takes a full five generations to convert a population of primary electrons born at $\Phi \approx 60 \text{ V}$ into secondary electrons [7:6123].

2.2 Wall Losses

Wall losses and recombination are the two principal losses of charged particles in a tandem volume multicusp ion source [7:6124]. As ions reach the wall, which also serves as the anode of the discharge, they are generally neutralized. Although the wall is protected with a short-range multipole magnetic field, ions are lost to the cusps between the magnets. The apparent width of the cusps varies according to species, appearing the smallest to the fast-moving primary electrons, rather larger to the slow secondary electrons, and larger still to the ions [18:31]. Notwithstanding the apparent size of the cusps, the higher the energy of the primary electrons, the higher their loss rate to the walls [24:365].

In addition to neutralizing electrons and H ions, the walls will also neutralize H^- ions. Johnson [18:42] estimates the rate constant k_{wall} for neutralization of H^- in the reaction



in terms of the plasma potential Φ_{plasma} and the negative ion temperature $T^{H^-} \approx 0.4 \text{ eV}$ to be

$$k_{wall} = 2.4 \times 10^4 \sqrt{T^{H^-}} \exp \left\{ \frac{\Phi_{plasma}}{T^{H^-}} \right\} \quad (2)$$

One could argue that a one-dimensional model would lose plasma to the wall only at the inner boundary $z = 0$. However, losses at the wall along the entire length of a real ion source lower the plasma density near the wall, and the high random thermal velocity of the plasma quickly transmits the effect of this lowered density near the wall throughout the volume. Therefore, a rigorous model must account for wall losses in some fashion.

2.3 The Magnetic Filter Field

The magnetic filter field divides the tandem ion source into driver and extraction chambers. In the axial direction, its profile is approximately Gaussian, with an intensity almost two orders of magnitude lower than the multipolar field protecting the walls ($\sim 80 \text{ Gauss}$ vs. $\sim 3600 \text{ Gauss}$). The $v \times B$ force that the charged particles experience in the field causes them to orbit around a "guiding center" at a distance equal to their Larmor radius, r_L , given by

$$r_L = \frac{m^\alpha v^\alpha}{|Z^\alpha| e B}$$

Because the ions have much greater mass, their gyroradius in the weak magnetic filter field is so large that they are deflected only slightly as they pass through it [23:56]. Electrons, on the other

hand, are either deflected by the filter field and returned to the extraction region discharge (if their energies are sufficiently high) or are trapped by the magnetic field lines. As these trapped electrons orbit, they collide with other particles in the volume. Each collision causes the guiding center of the electron's orbit to be displaced randomly, so the electron begins a "random walk" diffusion in the magnetic filter. The electrons that reach the extraction chamber through diffusion are all thermalized (cold) from collisions. Thus the magnetic filter effectively creates a barrier that stops hot primary electrons but allows cold secondary electrons to pass through readily [8:1423], limiting the mean electron temperature in the extraction chamber to about 0.4 eV [23:56]. A magnetic filter field of strength $B \gtrsim 30\text{ Gauss}$ is sufficient to prevent the primary electrons from reaching the extraction region [18:295-296].

2.4 *The Formation of Negative Ions*

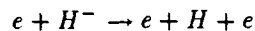
Negative ions are formed in a two-step process. In the first step, fast primary electrons excite electronic states of precursor molecules, which spontaneously relax to vibrationally excited states. In the second step, slow electrons produce negative ions from the vibrationally excited molecules through dissociative attachment reactions. The tandem multicusp volume source, with two chambers separated by a magnetic field, is ideally suited to meet these inherently incompatible production requirements.

The primary route of formation of negative ions in a volume of plasma is through dissociative attachment of an electron to a vibrationally excited gas molecule [18:38]:



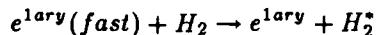
where v'' signifies a vibrationally excited state of H_2 . This reaction is labelled Reaction 56 in Appendix B. Reaction 56 obviously requires a large population of $H_2(v'')$ to create a significant amount of H^- . This is where the tandem volume source has its great advantage. Creating sufficient

amounts of $H_2(v'')$ requires a population of fast electrons; however, these same fast electrons that form $H_2(v'')$ neutralize H^- ions at a high rate by way of the collisional detachment reaction:

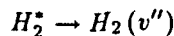


which is Reaction 7 in Appendix B. In the tandem volume source, the driver region is populated with fast primary electrons that can excite the vibrational modes of H_2 , and the extraction region is free from these same fast electrons that would dissociate H^- . According to Hiskes [14:3], there are three sources of $H_2(v'')$: (1) relaxation of H_2^* electronically excited by collisions with primary electrons, (2) neutralization of H_2^+ at the wall, and (3) relaxation of H_2^* electronically excited by collisions with the wall.

The sequence of events runs roughly as follows: In the driver region, a primary electron, e^{1ary} , gives up kinetic energy to excite an H_2 molecule electronically [15:34]:



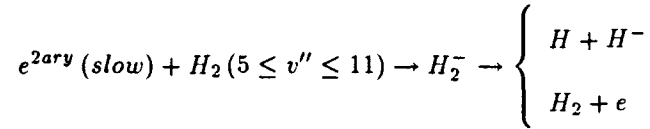
The electronically excited H_2^* molecule next relaxes to a vibrationally excited state $H_2(v'')$ [18:35]



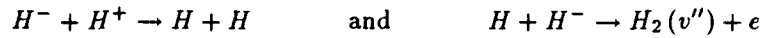
Approximately 90% of the H^- ions extracted from the source are derived from H_2 ($5 \leq v'' \leq 11$) [14:6]. Because the cross sections are smaller for the lower vibrational states, and because the probability of an electron spontaneously detaching from the ion increases significantly at vibrational excitation levels above $v'' = 9$ [18:36], the most important vibrational states are $6 \leq v'' \leq 9$ [18:36]. The increase in probability of reaction with vibrational states is significant: the cross section for Reaction 56 in Equation 3 increases about four orders of magnitude from $v'' = 0$ to $v'' = 4$ [18:36]. The excitation may actually proceed in a two- or three-step process, since the probability for the

H_2 molecule to reach $5 \leq v'' \leq 11$ through collision with an electron is much greater when it begins from the vibrational population at $v'' = 1$ or $v'' = 2$ instead of the one at $v'' = 0$ [15:34].

The magnetic filter field is transparent to neutral H_2 molecules, so they readily reach the extraction region, where they collide with slow secondary electrons e^{slow} and can form H^- by way of the intermediate unstable molecular ion H_2^- [18:35]:



In the extraction region, the principal loss processes for H^- are the mutual neutralization Reaction 11 with H^+ ions and the associative detachment Reaction 58 with H atoms [14:6]:



The chain of reactions that produce H^- appears to be quite successful because in the extraction region the density of H^- can approximate the density of electrons [18:35-36].

2.5 Summary of Kinematics

Figure 10 summarizes the relevant kinematic processes in a tandem multicusp volume hydrogen ion source. A jet admits hydrogen gas into the chamber, and a cathode inputs fast primary electrons into the driver region. These primary electrons ionize the hydrogen gas, forming a plasma. Recombination reactions among the reactants and with the wall limit the plasma density and produce vibrationally excited gas molecules. The magnetic filter field transmits neutral atoms and molecules, positive ions, and cold secondary electrons, while acting as a barrier to fast primary electrons. In the extraction region, interactions between cold electrons and vibrationally excited gas molecules create negative ions while other interactions with the reactants tend to destroy them.

III. The Plasma Balance

Glasser and Smith based the model on a two-fluid (H^+ and e) derivation of the plasma transport equations, enhanced by the effect of collisions with neutral species (H and H_2) [9:409]. Thus of the seven species in Table 1 in Chapter II, the model considers only four (e , H^+ , H , and H_2) and reduces the number of reactions to seven, as given in Table 2.

Inelastic Chemical Reactions					$k_N = \langle \sigma_N v \rangle$	
N	j	reaction	name	ε_{th}	$T^j = 1 \text{ eV}$	$T^j = 10 \text{ eV}$
19	e	$e + H \rightarrow H^+ + 2e$	ionization	13.6	3.4×10^{-15}	5.7×10^{-9}
23	i	$H + H^+ \rightarrow H^+ + H$	charge exchange	0.0	9.1×10^{-9}	3.2×10^{-8}
26	e	$e + H^+ \rightarrow H + h\nu$	radiative capture	0.0	1.6×10^{-12}	3.2×10^{-13}
Elastic Scattering Reactions					σ_N	
N	j	reaction	name	ε_{th}	$T^j = 1 \text{ eV}$	$T^j = 10 \text{ eV}$
34	e	$e + H_2 \rightarrow e + H_2$	elastic	0.0	1.7×10^{-15}	1.0×10^{-15}
48	e	$e + H \rightarrow e + H$	elastic	0.0	4.7×10^{-15}	1.6×10^{-15}
36	i	$H^+ + H_2 \rightarrow H^+ + H_2$	elastic	0.0	5.0×10^{-15}	7.9×10^{-16}
49	i	$H^+ + H \rightarrow H^+ + H$	elastic	0.0	1.4×10^{-14}	1.1×10^{-14}

Table 2. The Seven Reactions Used in the Numerical Model.

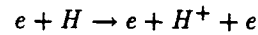
Table 2 also gives representative reaction rates k_N for the inelastic chemical reactions and representative cross sections σ_N for the elastic scattering reactions. These representative rates and cross sections are those that the model calculates for temperatures of 1 eV and 10 eV.

Because the model reduces the number of interacting species to four and the number of interactions to seven, most of the complexity of the hydrogen ion source is lost. Unfortunately, the dominant reactions in a hydrogen plasma at the energies of interest are among those discarded. The model does not consider the dominant path of ionization at the electron temperature that it calculates, nor does it consider the dominant paths for recombination. As a result, the model calculates a charged particle balance between production and outflow instead of the correct balance between production and loss.

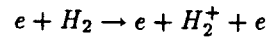
3.1 Ionization

The model considers only the ionization reaction between electrons and neutral hydrogen atoms. Its standard initial conditions [9:422] assume that the density of neutral molecules is larger than the density of neutral atoms by over an order of magnitude. Since the reaction rate for the ionization of neutral molecules is approximately the same as the rate for the ionization of neutral atoms at the electron temperature calculated by the model, the model therefore underestimates the ionization by about an order of magnitude.

Because the model considers chemical reactions among only the species H , H^+ , and e , it produces plasma in the volume by way of Reaction 19 in Table 2 and in Appendix B:



which is Reaction 2.1.5 in Janev *et al.* [17:3]. Since the density of molecular hydrogen H_2 is roughly an order of magnitude larger than the density of atomic hydrogen H , it is natural to consider the contribution of the ionization reaction between electrons and molecular hydrogen:



which is Reaction 24 in Appendix B and Reaction 2.2.9 in Janev *et al.* [17:3]. Table 3 compares the H ionization reaction rate k_{19} for Reaction 19 with the H_2 ionization reaction rate k_{24} for Reaction 24 over a range of energies. The reaction rates given for Reaction 19 are those calculated by the model [35], which agree well with those given in Janev *et al.* [17:26], and the reaction rates for Reaction 24 are from Janev *et al.* [17:52].

Both of these reaction rates show a sharp increase with electron temperature. Because the threshold energy for Reaction 19 with H ($\epsilon_{th} = 13.6 \text{ eV}$) is lower than the threshold energy for Reaction 24 ($\epsilon_{th} = 15.4 \text{ eV}$), the rate of Reaction 19 tends to dominate somewhat at lower tem-

T^e (eV)	$k_N = \langle \sigma_N v^e \rangle$ (cm ³ /sec)	
	k_{19} (H)	k_{24} (H ₂)
1	3.4×10^{-15}	$\ll 10^{-11}$
3	1.2×10^{-10}	6.0×10^{-11}
7	2.7×10^{-9}	2.4×10^{-9}
10	5.3×10^{-9}	6.3×10^{-9}
100	3.2×10^{-8}	5.0×10^{-8}

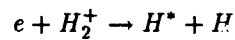
Table 3. Comparison of Reaction Rates for Ionization Reaction 19 [35] and Ionization Reaction 24 [17:52].

peratures ($\lesssim 3$ eV). However, at the electron temperature that the model calculates (~ 7 eV), the reaction rates for both reactions are approximately equal, so the higher density of molecular hydrogen causes the principal ionization path to be Reaction 24. By this measure, the model underestimates the rate of ionization by an order of magnitude.

3.2 Recombination

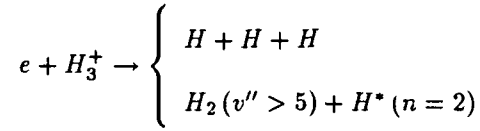
Plasma is lost in the volume through recombination reactions and wall losses. The primary electron recombination path is not the radiative recombination reaction with H^+ (Reaction 26 in Table 2 and Appendix B) upon which the model is based, but rather the dissociative recombination reactions with H_2^+ and H_3^+ . Because these reactions have multiple products to carry away momentum and energy, they are fast reactions. On the other hand, Reaction 26 with H^+ emits a photon to conserve energy and is thus a slow reaction [34:18-19].

The principal electron recombination reaction with H_2^+ is Reaction 2.2.14 in Janev [17:62]:



where H^* represents an electronically excited state of hydrogen. Appendix B lists a less specific form of this dissociative recombination reaction as Reaction 16. The principal recombination reaction

with H_3^+ has two possible paths:



which are Reactions 2.2.15a and 2.2.15b in Janev [17:64]. This dissociative recombination reaction corresponds roughly to Reaction 17 in Appendix B.

Table 4 compares the reaction rate k_{26} for Reaction 26 with the reaction rates k_{16} and k_{17} for Reactions 16 and 17. All data in the Table 4 are estimated from the curves given in Janev *et al.* [17]. The table shows that the electron recombination rate with H_2^+ is faster from 1 to 3 eV,

T^e (eV)	$k_R = \langle \sigma_R v^e \rangle$ (cm ³ /sec)		
	k_{26}	k_{16}	k_{17}
1	1.4×10^{-13}	5.5×10^{-8}	4.2×10^{-8}
3	8.0×10^{-14}	2.8×10^{-8}	2.6×10^{-8}
7	4.7×10^{-14}	1.7×10^{-8}	2.0×10^{-8}
10	3.6×10^{-14}	1.3×10^{-8}	1.5×10^{-8}

Table 4. Reaction Rates [17] for Representative Recombination Reactions.

and the rate with H_3^+ is fastest from 7 to 10 eV. Either path for neutralizing electrons by way of reactions with H_2^+ or H_3^+ is more probable than the path with H^+ used in the model by almost six orders of magnitude. Reaction 26 with H^+ is clearly inadequate as the sole loss mechanism. The result of the lack of a correct loss mechanism is that the model achieves an incorrect charged particle balance in the continuity equation.

3.3 The Plasma Balance

The plasma balance is described by the continuity equation. Equation 46 in Appendix A gives a form of the continuity equation:

$$\frac{\partial}{\partial t}(n^\alpha) + \frac{\partial}{\partial x_i^\alpha}(n^\alpha V_i^\alpha) = S_{production}^\alpha - S_{loss}^\alpha$$

Since the final solution is in a steady state, the time derivative is zero, and the particle balance along the axial direction becomes

$$\frac{\partial}{\partial z}(n^\alpha V_i^\alpha) = n^e n^0 \sum_{\mathbf{R}} \langle \sigma_{\mathbf{R}} v \rangle_{\text{ionization}} - n^e n^i \sum_{\mathbf{R}} \langle \sigma_{\mathbf{R}} v \rangle_{\text{recombination}}$$

Under the assumptions and reduced reaction set of the model, this balance reduces to

$$\frac{\partial n V_i}{\partial z} = n n^0 k_{19} - (n)^2 k_{26}$$

Using the model's published standard "test case" data [9:422], $n \approx 4 \times 10^{11} \text{ cm}^{-3}$, $n^0 \approx n^H \approx 3 \times 10^{12} \text{ cm}^{-3}$, and $T^e \approx 7.5 \text{ eV}$. At $T^e = 7.5 \text{ eV}$, the model computes reaction rates of $k_{19} \approx 3 \times 10^{-9} \text{ cm}^{-3} \text{ sec}^{-1}$ and $k_{26} \approx 5 \times 10^{-13} \text{ cm}^{-3} \text{ sec}^{-1}$, so the particle balance becomes

$$\frac{8 \times 10^{16} \text{ cm}^{-2} \text{ sec}^{-1}}{20 \text{ cm}} \approx (4 \times 10^{11})(3 \times 10^{12})(3 \times 10^{-9}) - (4 \times 10^{11})(4 \times 10^{11})(5 \times 10^{-13})$$

$$\underbrace{4 \times 10^{15} \text{ cm}^{-3} \text{ sec}^{-1}}_{\text{flux}} \approx \underbrace{4 \times 10^{15} \text{ cm}^{-3} \text{ sec}^{-1}}_{\text{production}} - \underbrace{8 \times 10^{10} \text{ cm}^{-3} \text{ sec}^{-1}}_{\text{loss}}$$

Thus the production (ionization) is not balanced by loss (recombination) as would be expected, but by flow out of the extraction region. Since all of the plasma that the source produces is extracted, this type of balance would be ideal for an ion source; however, because production is underestimated by an order of magnitude and because loss is underestimated by several orders of magnitude, it is not realistic. This incorrect particle balance is a significant limitation of the model.

In simplifying the kinematics of the hydrogen ion source, the model discards some of the dominant reaction paths. It underestimates plasma production by about an order of magnitude and plasma loss by almost six orders of magnitude. The resulting incorrect balance between production and outflow instead of production and loss significantly limits the usefulness of the model.

Section 4.4 shows that the model has to raise the electron temperature by almost an order of magnitude to make up for the underestimate of ionization.

IV. The Behavior of the Unmodified Model

Running the model with the published inputs for the test case reproduced the results in Glasser and Smith [9:422] as accurately as could be determined from the published graphs. However, the calculated behavior of the primary variables differs from what would be expected from intuition and is obtained by experiment. Moreover, results differ from run to run, even when the initial inputs are identical.

4.1 Replication of the Results in the Original Article

Figure 11 shows the temporal evolution of the four primary variables (charged particle density, drift velocity, electron temperature, and ion temperature). These results reproduce those in Figures 3 through 6 in Glasser and Smith [9:422]. Each graph displays the value of one of the primary variables as a function of the axial dimension of the ion source. The graphics routine plots one curve at each time cycle ($\sim 3 \times 10^{-5}$ sec), with 25 cycles displayed. Clustering of the curves indicates convergence to an equilibrium solution.

Figure 12 reproduces the results of Figure 7 in Glasser and Smith [9:423], showing the movement of the node positions used in the method of moving finite elements as functions of time. The horizontal axis plots time, and the vertical axis plots the axial dimension of the source. Node positions tend to cluster where the second derivatives of the primary variables are the greatest, which occurs in this case at inflection points on either side of the magnetic filter field. Convergence to the final positions is rapid, being essentially complete by the seventh cycle.

The time order of the plots in Figure 11 isn't completely obvious. For this reason, Figure 13 shows the values of the primary variables at the outflow boundary (position $z = 25$ cm, integration bin $j = 40$). These graphs provide a means to verify the convergence of solutions and to identify other phenomena, such as limit cycles.

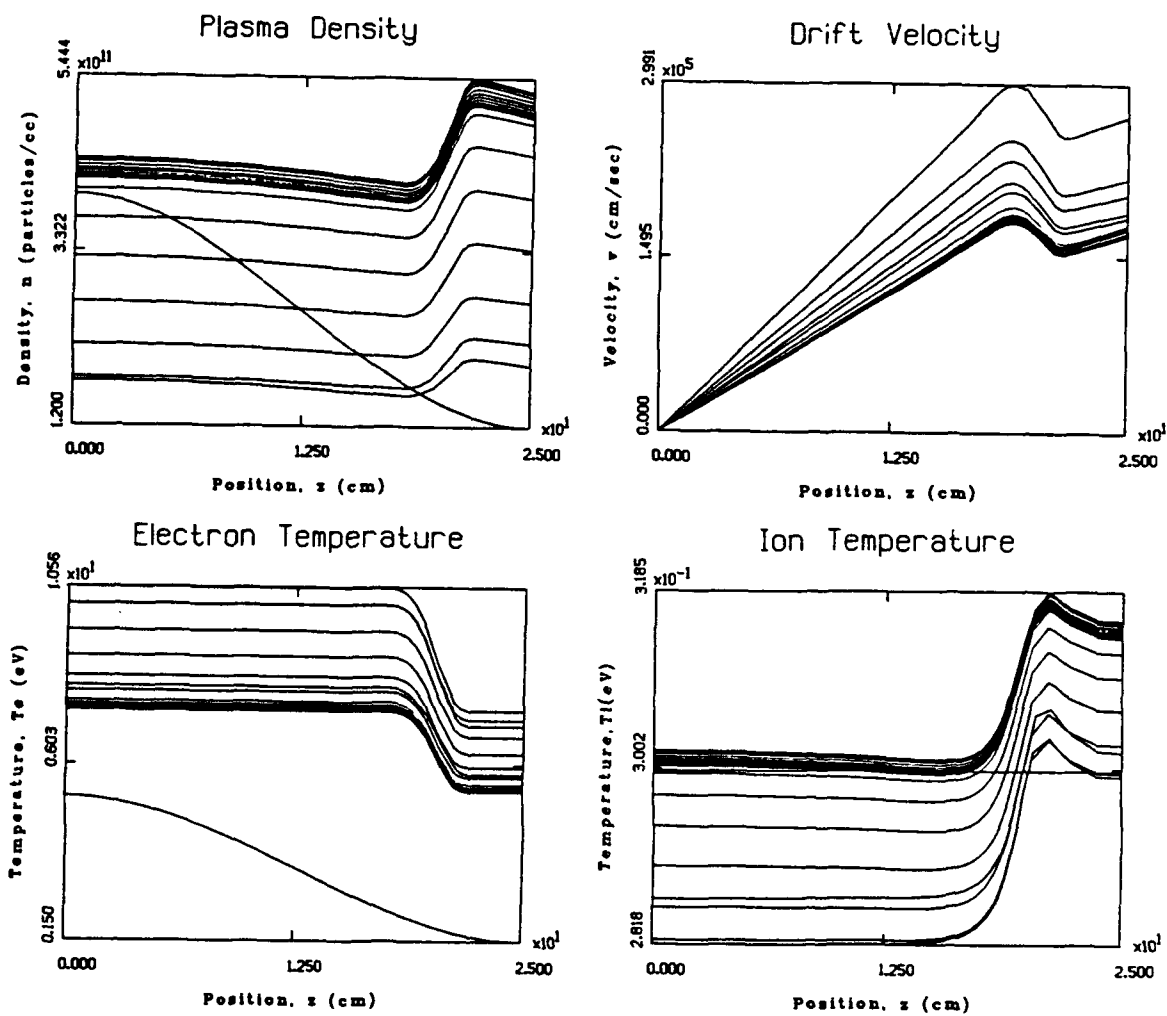


Figure 11. Replication of the Results of the Model Presented in Glasser and Smith [9:422].

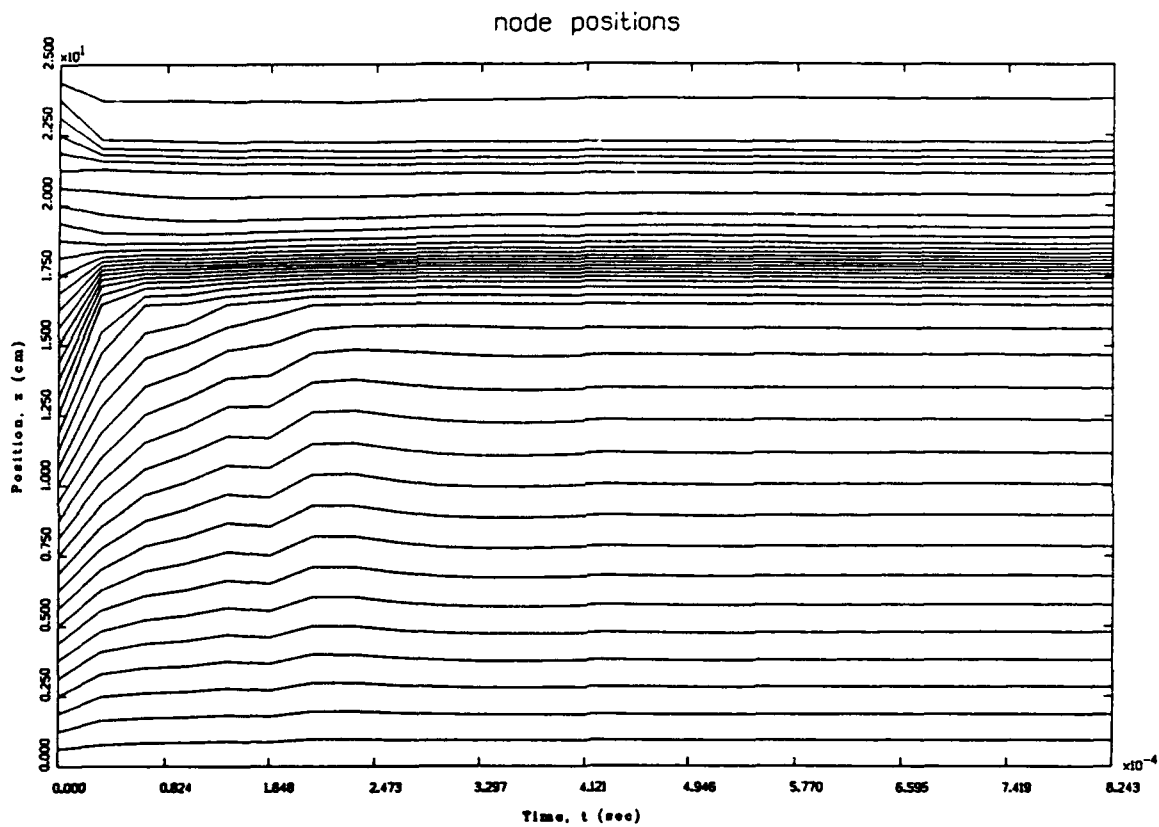


Figure 12. Replication of the Node Positions in the Finite Elements Method as Functions of Time as Presented in Glasser and Smith [9:423].

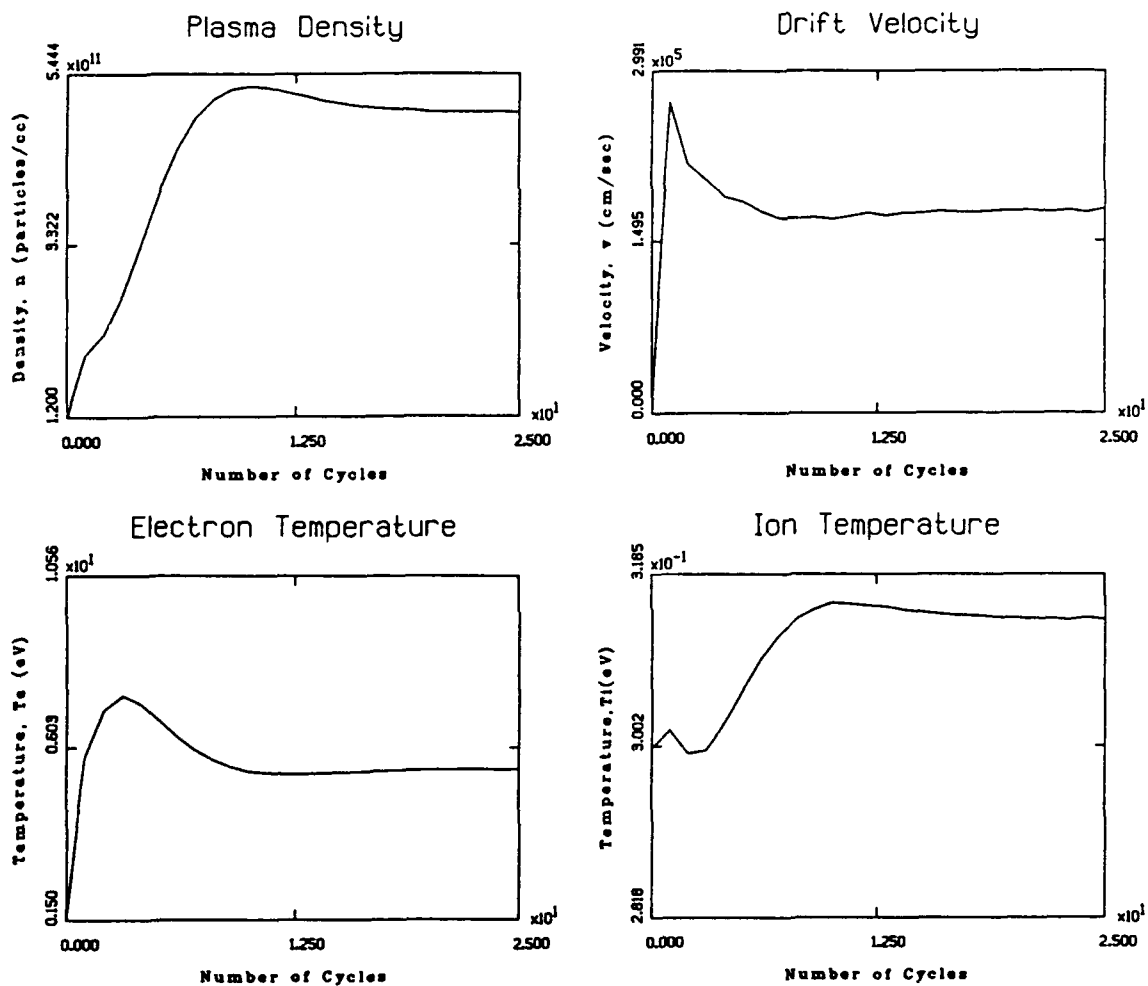


Figure 13. Values of the Density, Drift Velocity, Electron Temperature, and Ion Temperature at the Outflow Boundary as Functions of Time.

4.2 Plasma Density

The upper left graph in Figure 11 shows multiple plots of the calculated values of the plasma density, n , as a function of the axial dimension of the ion source. The lower graph in Figure 14 shows the equilibrium state of the plasma density after 25 integration cycles (about $8 \times 10^{-4} \text{ sec}$). The plasma density is greatest in the extraction region. This result seems counterintuitive: since in a real ion source the magnetic filter field acts as a barrier to ionizing fast electrons, confining them to the production region, and since electrons and ions recombine in and flow out of the extraction region, one would expect the density in the extraction region to be *lower* than in the production region, rather than higher. Moreover, the plasma flows along the axis from the production region to the extraction region, and particles should flow from high to low density, rather than from low to high. Experimentally, according to Ehlers and Leung, "the plasma density in the extraction chamber is always less than in that in the source chamber" [8:1423]. Johnson [18:162] gives experimental values of the axial variation of plasma density that confirm the observation of Ehlers and Leung. The upper graph in Figure 14 reproduces Johnson's data for an ion source with a magnetic filter field of strength 80 Gauss centered at 15 cm. Apparently the initial guess at the plasma density in the input to the test case, shown in the graph of density in Figure 11, is roughly correct; however, the model takes this correct solution and immediately distorts it, as early as the first cycle ($\sim 3 \times 10^{-5} \text{ sec}$), into one very similar to the final output.

Another troubling result is that the final values of the plasma density depend upon the value of the initial guess used in its calculation. This is troubling because there is no physical significance to the initial guess used. The *path* to the final answer should reflect the character of the initial guess, but the final answer should depend only on the actual physical parameters. After this behavior became apparent, the model was run with several different combinations of initial densities at the right and left boundaries. Three initial densities were chosen to match the "test case" initial conditions in the original article [9:422]: 4.0×10^{11} , 2.5×10^{11} , and $1.2 \times 10^{11} \text{ cm}^{-3}$ as the respective

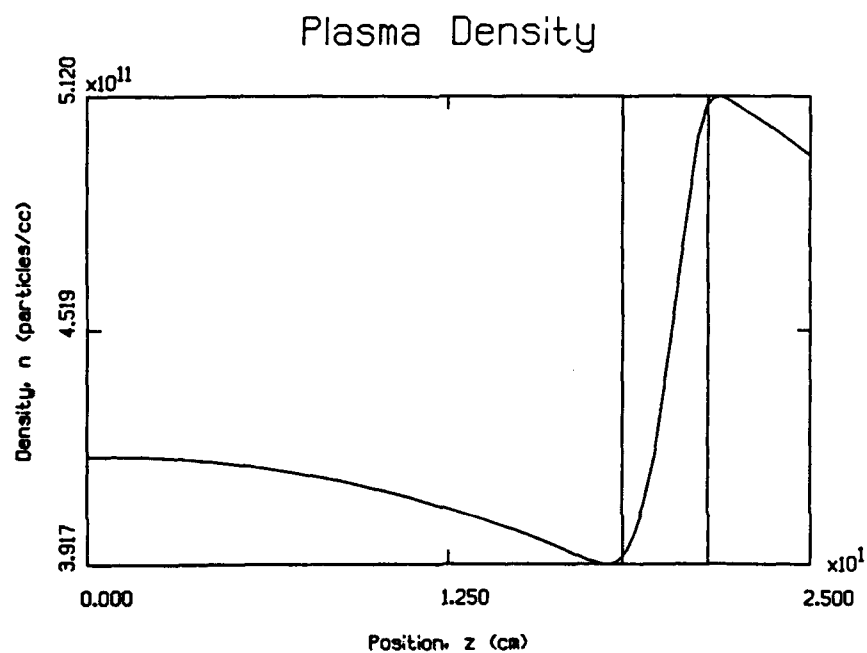
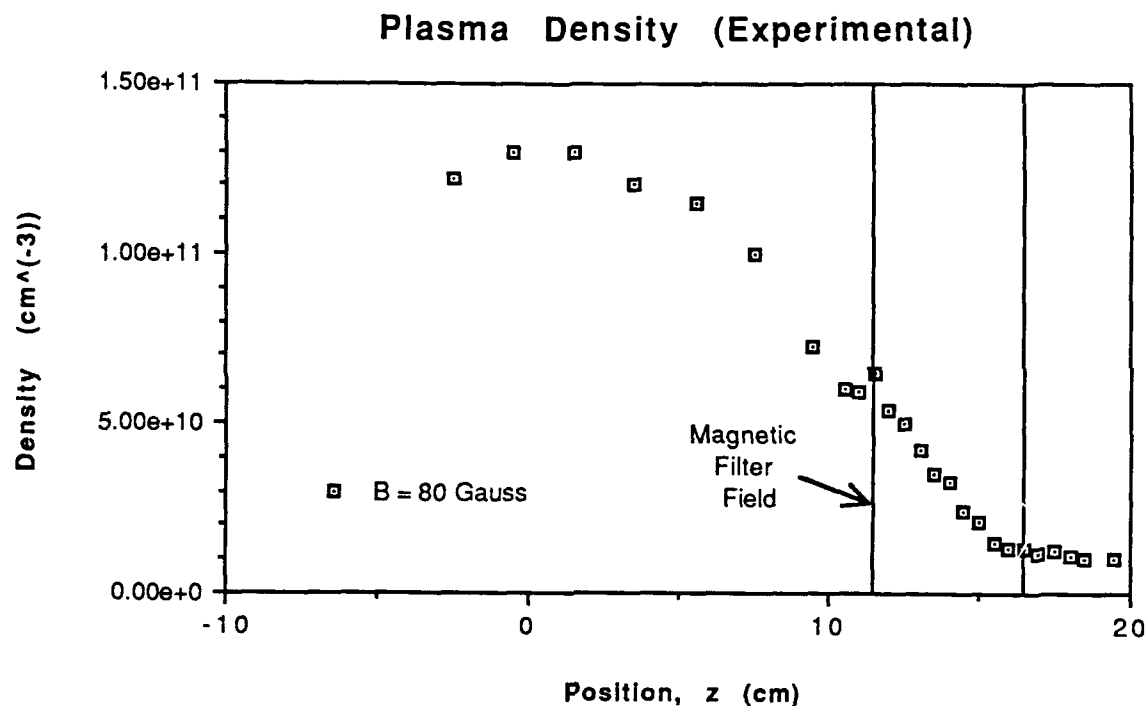


Figure 14. Axial Variation of Plasma Density: Experimental Measurement (Top) from Johnson [18:162] Compared to Calculations by the Model (Bottom). In both graphs, the filament cathodes are located at $z = 0$, and vertical lines mark the $1/e$ points of the magnetic filter field.

high, medium, and low densities. The high density was the left initial density (at the filaments) in the standard run, the low density was the right initial density (at extraction), and the medium density was roughly in the middle. The model was run with flat initial density profiles at all three values, with the standard initial profile, and with a reversed initial profile. Table 5 gives the results for the maximum final density resulting from these runs of the model, grouped by the initial density at the left boundary:

initial density at left boundary	initial density at right boundary	maximum final density
4.0×10^{11}	4.0×10^{11}	5.326×10^{11}
4.0×10^{11}	1.2×10^{11}	5.867×10^{11}
2.5×10^{11}	2.5×10^{11}	3.466×10^{11}
2.5×10^{11}	1.2×10^{11}	3.406×10^{11}
1.2×10^{11}	4.0×10^{11}	1.645×10^{11}
1.2×10^{11}	1.2×10^{11}	1.143×10^{11}

Table 5. Variation of the Maximum Final Values of the Plasma Density with Changes to the Initial Values.

Table 5 shows that the final value of the density depends strongly upon the value assumed for the density at the left boundary, n_0^e , and hardly at all upon the value at the right boundary, $n_{z_{max}}^e$. Section 5.1 shows that this dependence occurs because of the way that the model defines the energy flux.

Another feature of the calculated density profile is the apparently parabolic decrease in density in the production region. It is possible to derive this parabolic decrease analytically. Beginning with the one-dimensional momentum equation implemented in the model, Equation 9 in Section 6.1 and Equation 3.4 in Glasser and Smith [9:412]

$$\begin{aligned} \frac{\partial V_z}{\partial t} + V_z \frac{\partial V_z}{\partial z} + \frac{1}{m} \sum_{\alpha} \frac{p^{\alpha}}{(n)^2} \frac{\partial n}{\partial z} - \frac{4}{3m(n)^2} \frac{\partial V_z}{\partial z} \sum_{\alpha} \eta^{\alpha} \tau^{\alpha} p^{\alpha} \frac{\partial n}{\partial z} \\ + \frac{1}{m} \frac{\partial}{\partial z} \sum_{\alpha} \left[\frac{p^{\alpha}}{n} \left(1 - \frac{4}{3} \eta^{\alpha} \tau^{\alpha} \frac{\partial V_z}{\partial z} \right) \right] + \frac{1}{nm} (-R_z^{en} - R_z^{in} + mV_z S_{coll}) + dV_z = 0 \end{aligned}$$

and discarding all but the two dominant terms, Term 3 and Term 9 [35] identifies an approximate balance between these two terms:

$$\frac{1}{m} \sum_{\alpha} \frac{p^{\alpha}}{(n)^2} \frac{\partial n}{\partial z} + dV_z = 0$$

Substituting $p^{\alpha} = nT^{\alpha}$ and solving for $\frac{\partial n}{\partial z}$ gives

$$\frac{\partial n}{\partial z} = -\frac{md}{\sum_{\alpha} T^{\alpha}} nV_z = -\frac{md}{\sum_{\alpha} T^{\alpha}} \Gamma$$

where $\Gamma = nV_z$ is the particle flux. Figure 15 shows that the model calculates a constant temperature in the production region, and Figure 19 shows that it calculates a flux in the production region that varies approximately linearly with position. Denoting the slope of the graph of the flux by A , the relation $\Gamma = Az$ then describes this linear variation. Substituting this linear relation for the flux into the simplified momentum equation gives a differential equation in z :

$$\frac{\partial n}{\partial z} = -\frac{Amd}{\sum_{\alpha} T^{\alpha}} z$$

Integrating this differential equation with respect to z yields an explicit expression for the plasma density:

$$n = -\frac{Amd}{2\sum_{\alpha} T^{\alpha}} (z)^2 + z_0$$

where z_0 is the constant of integration. Define the constant c_0 to be the coefficient of the $(z)^2$ term; then the expression for the density takes the form

$$n = z_0 - c_0(z)^2$$

which describes a parabolic decrease in the plasma density as the distance from the filament cathode increases. Figure 14 shows a similar but larger decrease in the plasma density in the experimental

values from Johnson [18:162]. However, Chapter III shows that the plasma balance in the model does not correspond to that in a real source. For this reason, the assumptions of the derivation above may not apply, and the density profile in the production region of a real source may decrease for a different reason.

Therefore, even though the model calculates a density profile that appears to be qualitatively correct in the production region, it calculates a profile through the magnetic filter field that is opposite to that expected from intuition and observed by experiment. Moreover, the final values of the density depend on the initial guess at a solution. Both of these features severely limit the utility of the model in predicting the behavior of an ion source.

4.3 Drift Velocity

The upper right graph in Figure 11 shows multiple plots of the time evolution of calculated values for the velocity V_i^α as a function of the axial dimension of the ion source. Since the model assumes that the plasma is initially stationary, the initial (zeroth-cycle) plot of the drift velocity in Figure 11 is uniformly zero across the bottom of the graph. The second (first-cycle) plot of the drift velocity overshoots the eventual equilibrium value, to which it converges rapidly. By the seventh cycle, subsequent curves cannot be distinguished from one another on the scale of the plot. The upper right graph of Figure 13 shows this overshooting and rapid convergence for the drift velocity at the outflow boundary.

The average drift velocity is held to zero at $z = 0$ by a boundary condition applied in the module *arrays*. The physical interpretation of the plot is as follows: Plasma is "born" at rest in the vicinity of the filaments at $z = 0$. The linear increase in velocity in the driver region in Figure 11 shows that the acceleration of the plasma is constant there. The magnetic filter retards the electrons as they diffuse across it, causing a reduction in the average drift velocity. After the

filter field the acceleration once again becomes constant. This behavior appears to be intuitively reasonable.

4.4 *Electron Temperature*

The lower left graph in Figure 11 shows the evolution of the electron temperature T^e as a function of the axial dimension of the ion source. The initial (zeroth-cycle) plot of the electron temperature is near the bottom of the graph, and the second (first-cycle) plot is at the top. The lower left graph in Figure 13 shows that the second calculated value of the electron temperature at the outflow boundary overshoots the equilibrium value and that subsequent calculations converge to it, although not quite as rapidly as in the case of the drift velocity.

The lower graph of Figure 15 shows the equilibrium values of the electron temperature at the 25th cycle. The electron temperature decreases across the magnetic filter, as expected from the discussion in Section 2.3; however, there is a problem here, too. The average electron temperature determined experimentally in a real ion source is approximately 1 eV in the extraction region [1:21] and 2 eV in the production region [34:11], not 6 eV and 7 eV as predicted by the model. Figure 15 compares the electron temperature predicted by the model on the lower graph with the experimental values determined by Johnson [18:162] on the upper graph.

This discrepancy in electron temperature can be explained from the assumptions in the model. The model assumes one single-temperature maxwellian distribution of electrons. In reality the distribution is non-maxwellian, but it can be described reasonably accurately as a superposition of two maxwellian distributions, each with its own temperature. As described in Section 2.1, the larger of the two contains low-energy "secondary" electrons, and the smaller contains high-energy "primary" electrons. Figure 16 shows how the seemingly small discrepancy of ignoring the smaller distribution can make an order of magnitude difference in the results. The solid lines represent the two-population approximation to the experimentally-determined non-maxwellian electron distribu-

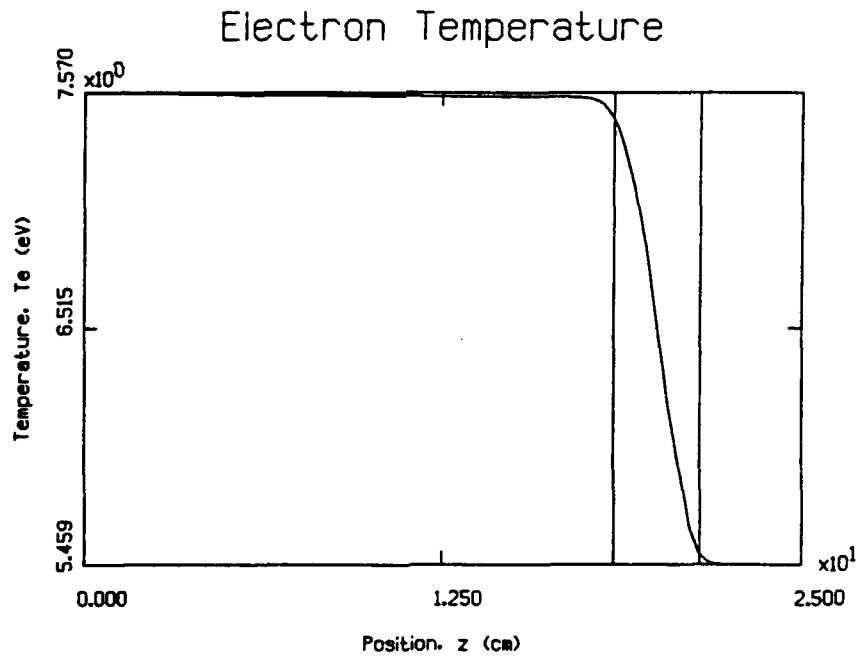
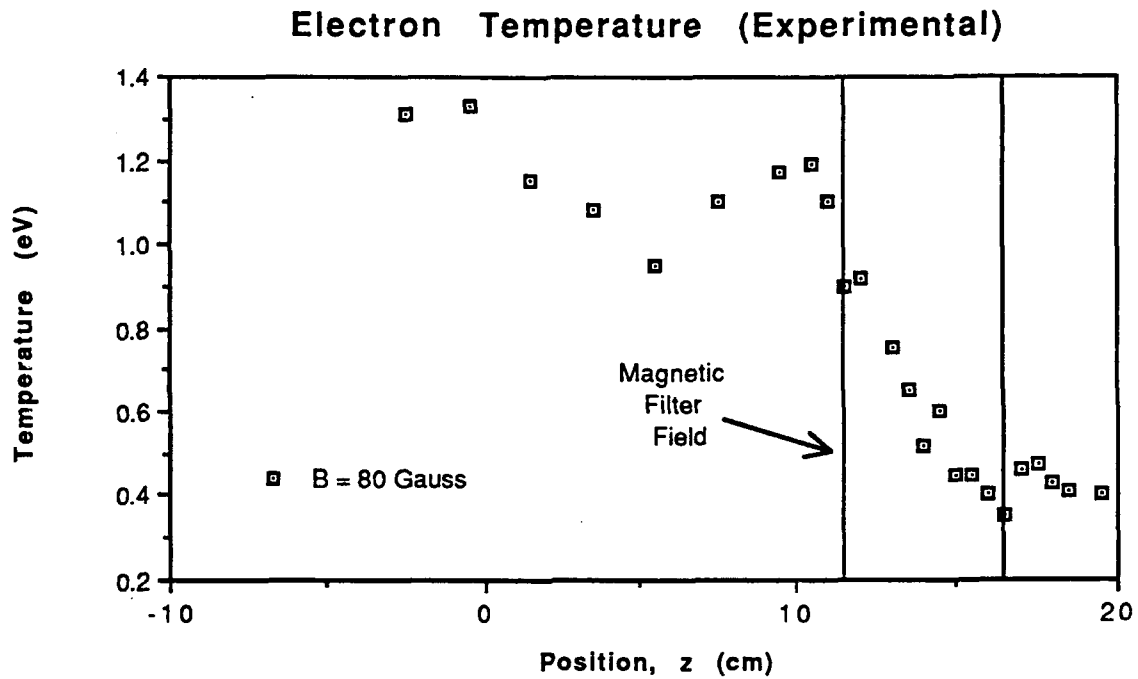


Figure 15. Axial Variation of (Secondary) Electron Temperature: Experimental Measurement (Top) from Johnson [18:162] Compared to Calculations by the Model (Bottom). In both graphs, the filament cathodes are located at $z = 0$, and vertical lines mark the $1/e$ points of the magnetic filter field.

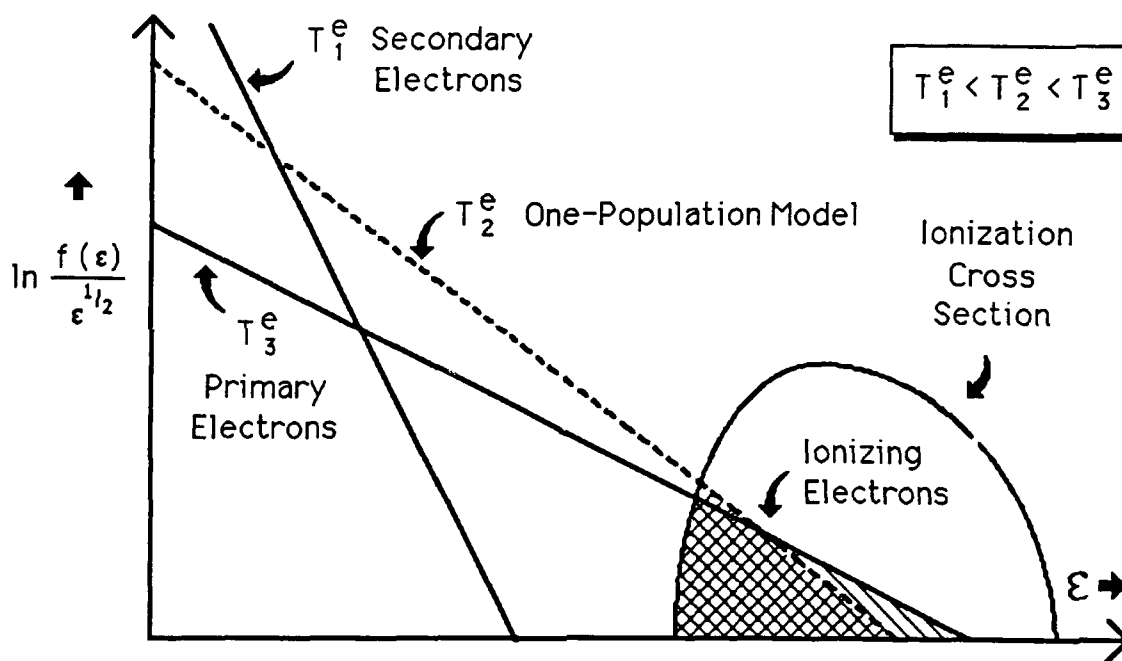


Figure 16. Schematic of the Difference Between a One-Population and a Two-Population Model of the Electron Energy Distribution.

tion. The dashed line represents the one-population distribution assumed in the model. Only those electrons with energies greater than the threshold energy for ionization can ionize neutral atoms or molecules. The probability of an ionization is proportional to the ionization cross section at that energy. Thus high energy electrons (the shaded area in the diagram) accomplish most of the ionization in the tandem volume source. By using a single electron distribution, the model requires the electron distribution to be at a much higher temperature to achieve a given rate of ionization than it would if it were to use two distributions at different temperatures. This is a serious limitation in the model which should be corrected if the model is to correctly predict experimental results.

4.5 Ion Temperature

The lower right graph in Figure 11 shows multiple plots of the evolution of the axial dependence of the ion temperature T^i . Since the model assumes a constant ion temperature throughout the source, the initial (zeroth-cycle) plot of the ion temperature is flat across the middle of the

graph. The first-cycle plot transforms this flat profile into a form very much like the equilibrium result. The lower right graph in Figure 13, of the ion temperature at the outflow boundary, shows that the ion temperature decreases slightly in the second cycle and then increases until it overshoots and then settles to its equilibrium value. The equilibrium profile remains relatively flat, varying only by about six percent from its highest to its lowest value.

In contrast to its prediction for the electron temperature, the model predicts an ion temperature T^i that is slightly higher in the extraction region than in the production region. Since in a real volume source, ions are heated by collisions with hot electrons and cooled by collisions with neutral gas molecules [18], one would expect the opposite behavior: In the production region, the ions can collide with hotter electrons and can thus receive *more* thermal energy there than in the extraction region. Johnson assumes that the positive ion temperature is approximately equal to the negative ion temperature ($T^i \approx T^{H^-}$), which he calculates to be within the range $0.2 \text{ eV} < T^{H^-} < 1 \text{ eV}$ [18:263]. The lower right graph in Figure 11 shows that the ion temperature calculated by the model falls within this range.

4.6 Results of Multiple Runs of the Code (*Irreproducible Results*)

The most distressing feature that the model exhibits is that running it with exactly the same initial conditions does not always produce the same results. Table 6 shows the results of multiple runs of the model with the same inputs as the standard case published in Glasser and Smith [9:422]. The order of the listing runs from lowest maximum density to highest.

As seen in Table 6, the runs with the lowest and highest maximum density are greatly different from the others. Although the other runs have results similar to each other, there is still a significant variation among them.

After this variation from run to run was observed, the standard case was run three times with enhanced graphics. Two of the runs were similar, yet not exactly the same. The plasma densities

run	n_{max}	$V_z)_{max}$	T_{max}^e	T_{max}^i
1	3.429×10^{11}	2.139×10^5	1.015×10^1	3.059×10^{-1}
2	5.104×10^{11}	1.848×10^5	7.579×10^0	3.171×10^{-1}
3	5.120×10^{11}	1.864×10^5	7.570×10^0	3.170×10^{-1}
4	5.138×10^{11}	1.843×10^5	7.567×10^0	3.172×10^{-1}
5	5.149×10^{11}	1.844×10^5	7.548×10^0	3.172×10^{-1}
6	5.163×10^{11}	1.843×10^5	7.550×10^0	3.173×10^{-1}
7	5.173×10^{11}	1.839×10^5	7.554×10^0	3.173×10^{-1}
8	5.840×10^{11}	1.615×10^5	7.276×10^0	3.206×10^{-1}

Table 6. Irreproducible Results: Variation of Final Maximum Values of the Primary Variables among Eight Runs of the Model.

differed in the fourth decimal place after the first cycle ($\sim 3 \times 10^{-5} \text{ sec}$), but by the 25th cycle ($\sim 8 \times 10^{-4} \text{ sec}$) they differed in the second decimal place. One of these two runs is given as the replica of the test case in Figures 11, 12, and 13.

The third run does not even converge by the 25th cycle. Figure 17 shows the results of this curious run, which was launched from the identical conditions that generated Figures 11 and 13. This figure corresponds to Figure 13 in that it shows graphs of the values of the primary variables at the outflow boundary as functions of the number of integration cycles. The plasma density appears to converge normally until about the 18th cycle ($\sim 6 \times 10^{-4} \text{ sec}$), when it starts to diverge.

To verify that the added graphics modules did not cause the variation from run to run, the model was run three times without them. These three runs also exhibited similar variations from run to run.

This variation from run to run is the most serious limitation of the model. If the results are not reproducible, then the model is practically useless. Any further research into the behavior of the model should identify and correct this limitation.

4.7 Summary of the Results of the Unmodified Model

In summary, even though the model was able to approximately reproduce the published results in Glasser and Smith [9:422], it is limited by several factors. First, calculated values of the

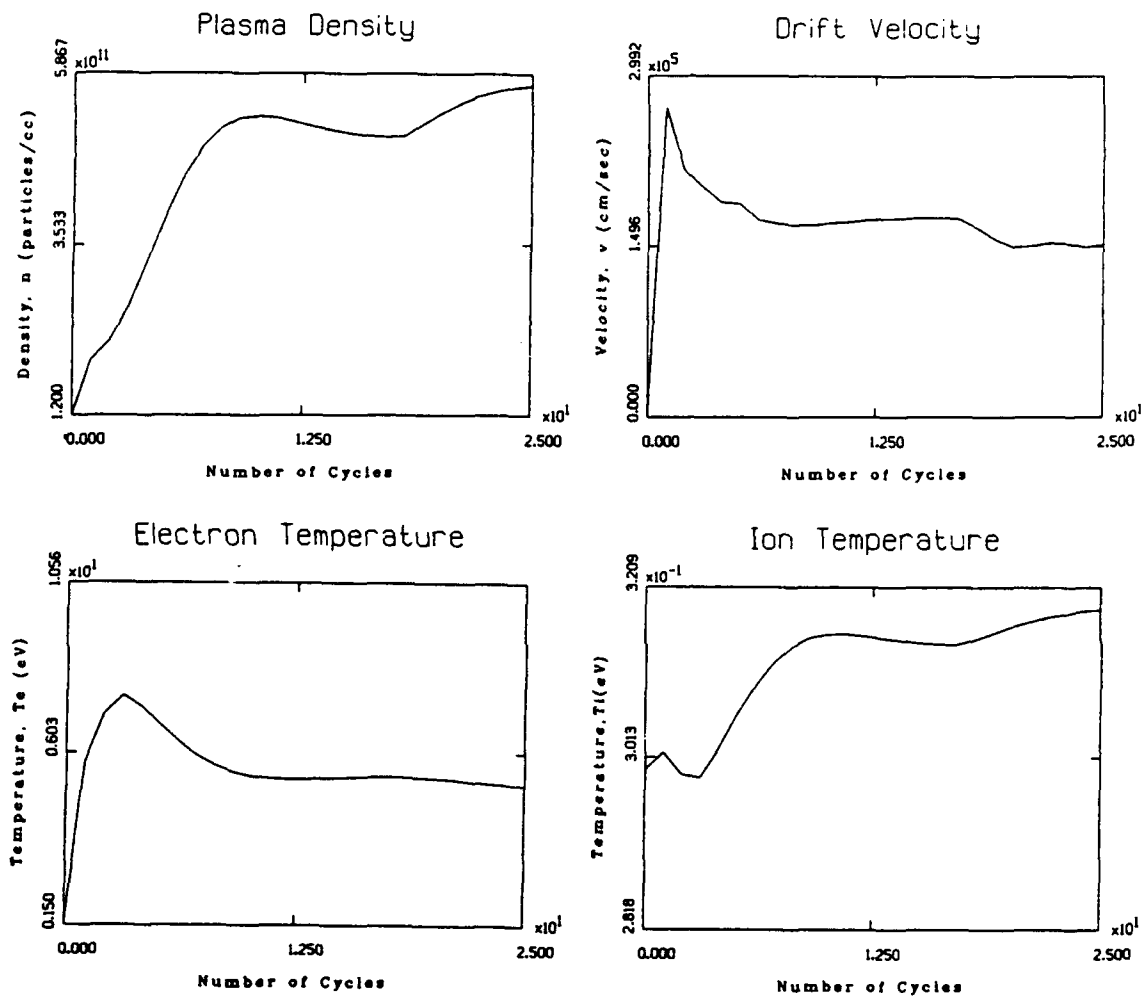


Figure 17. Non-converging Run of the Model with Standard Parameters: The Change in Time of the Values at the Outer Boundary.

plasma density trend opposite to intuition and experiment. Second, the final values of the density depend on the initial guess in the input file. Third, the calculated electron temperature is almost an order of magnitude higher than experimentally observed. Finally, and most seriously, calculated results differ run to run, even when the initial inputs are identical.

V. The Boundary Energy Flux

This thesis takes two exceptions with the approach that the model uses to establish and distribute the energy input from the discharge. First, the model determines the energy flux at the boundary of the driver region from the initial guess at the correct values of the density and the temperature. Thus the final solution also depends on these initial conditions, which are not physical parameters of the system. Second, the model injects energy from the discharge into only the first integration bin at $z = 0$. This leftmost integration bin is where the model locates the cathode filaments (see Figure 3 in Chapter I). Because the mean free path of the primary electrons is of the order of the length of the source, a uniform deposition of discharge energy into the production region, with the energy flux at the boundary set approximately to zero, would appear to be a better representation.

5.1 Dependence of Density on the Left Initial Condition

Table 5 in Section 4.2 shows that the final values of the plasma density depend strongly upon the initial value assumed for the density at the left boundary ($z = 0$). This dependence occurs because of the way that the model defines the energy flux at the left boundary. In line 174 of the *main* module of the *pos* code, the definition for the left boundary energy flux *eflux* is:

```
174      eflux=-e1fac*chiprpe(0)*(yr(3)-yl(3))/xmax
```

This left boundary energy flux represents the flow of energy density from the electrical discharge into the plasma. In symbols, the expression for the left boundary energy flux $\Gamma_{z=0}^e$ is:

$$\Gamma_{z=0}^e = -\Gamma_0^e \kappa_{z=0}^{\perp e} \frac{T_{z=z_{max}}^e - T_{z=0}^e}{z_{max}}$$

where $\frac{T_{z=z_{max}}^e - T_{z=0}^e}{z_{max}}$ is the initial electron temperature gradient, $\kappa_{z=0}^{\perp e}$ is the initial electron thermal conductivity¹ (at the left boundary) in the direction perpendicular to the magnetic filter field, and Γ_0^e is a “user parameter” that specifies how much energy the electrons conduct into the plasma [9:423]. The input file to the test case sets *eflfac* (Γ_0^e) to 0.02 [9:422].

Lines 117 and 118 of the module *brag* define the perpendicular electron thermal conductivity *chprpe* as

$$\kappa^{\perp e} = \frac{p^e \tau^e}{m^e} (\mathcal{P}(x^e))$$

where $p^e = n^e T^e$ defines the electron pressure p^e , $\tau^e = \frac{1}{\nu^e}$ defines the electron time between collisions τ^e in terms of the electron collision frequency ν^e , $x^e = \omega_c^e \tau^e$ defines the argument x^e of the polynomial $\mathcal{P}(x)$ in terms of the electron gyrofrequency ω_c^e and the mass of an electron m^e . Thus *chprpe*(0) is $\kappa_{z=0}^{\perp e}$, or the electron thermal conductivity $\kappa^{\perp e}$ evaluated at the left boundary $z = 0$.

Substituting these values into the expression for the energy flux input at the left boundary and rearranging factors shows a dependence on plasma parameters calculated at the left boundary at $t = 0$ and on initial conditions input into the model:

$$\Gamma_{z=0}^e = - \underbrace{\left\{ \frac{\Gamma_0^e}{m^e z_{max}} \right\}}_{\text{constants}} \underbrace{\{ \tau_{z=0}^e (\mathcal{P}(\omega_c^e \tau^e) |_{z=0}) \}}_{\text{plasma parameters}} \underbrace{\{ n_{z=0}^e T_{z=0}^e (T_{z=z_{max}}^e - T_{z=0}^e) \}}_{\text{initial conditions}}$$

This expression shows explicitly that the energy flux input at the left boundary depends on three initial conditions.

¹Braginskii defines the thermal conductivity κ^α for species α as

$$\kappa^\alpha = \frac{n^\alpha T^\alpha \tau^\alpha}{m^\alpha} (\mathcal{P}(x^\alpha))$$

in his equations 4.37 and 4.40 [3:249-250]. Glasser and Smith set $\kappa^\alpha = \mathcal{P}^\alpha(x^\alpha)$ in their equations 3.17 and 3.18 [9:413], and in the computer code they use *chi* (χ) to represent the thermal conductivity as defined by Braginskii. This thesis follows Braginskii's convention.

First, the energy flux input depends on $n_{z=0}^e$, the initial density at the left boundary:

$$\Gamma_{z=0}^e \propto n_{z=0}^e$$

Table 5 in Section 4.2 showed that the final solutions the model calculates depend on the initial values of the density at the left boundary. This dependence apparently comes through the calculation of the energy flux input at the left boundary. Section 5.2 elaborates on this observation.

Second, the energy flux at the left boundary depends on $T_{z=0}^e$, the initial electron temperature at the left boundary:

$$\Gamma_{z=0}^e \propto T_{z=0}^e$$

Third, the energy flux at the left boundary depends on difference between the initial electron temperature at the left boundary and the initial electron temperature at the right boundary:

$$\Gamma_{z=0}^e \propto (T_{z=z_{max}}^e - T_{z=0}^e)$$

The last two dependences on the initial temperature are not as straightforward to identify in the output from the model as is the first dependence on the initial density because they involve not only the temperature at the left boundary but also the difference in temperature between the two boundaries.

5.2 Left Boundary Condition for the Temperature

The only place that the computer code uses the variable *eflux* is in line 269 of the module *arrays* (line 549 of the composite code) where it sets the left boundary temperature gradient *y1* (3, 0) equal to the ratio of the energy flux and the thermal conductivity perpendicular to the magnetic field:

or in symbols,

$$\left. \frac{\partial T^e}{\partial z} \right)_{z=0} = -\frac{\Gamma_{z=0}^e}{\kappa_{z=0}^{\perp e}} = -\Gamma_0^e \frac{T_{z=z_{max}}^e - T_{z=0}^e}{z_{max}} \frac{\kappa_{z=0}^{\perp e})_{t=0}}{\kappa_{z=0}^{\perp e})_{t=t'}}$$

where t' is the current time of integration.

One significance of this boundary condition is that all of the energy injected into the volume enters the first bin at $z = 0$. Since the mean free path of an electron is determined primarily by the density of the most abundant constituent, H_2 , then

$$\lambda_{mfp} \approx \frac{1}{n_{H_2} \sigma_{e, H_2}} \approx \frac{1}{(4 \times 10^{13} \text{ cm}^{-3})(1 \times 10^{-15} \text{ cm}^2)} = \frac{1}{4 \times 10^{-2} \text{ cm}^{-1}} = 25 \text{ cm}$$

which is the length of the device. Thus first-generation primary electrons can interact with neutral gas molecules throughout the entire volume in the production region, so the model should input energy from the discharge uniformly into the whole production volume, not just into the first integration bin at $z = 0$.

5.3 Summary

This chapter has identified two reservations about the method that the model uses to incorporate energy input from the electrical discharge. Because the model bases its evaluation of the energy flux at the left boundary on an arbitrary input initial guess at the density and temperature at the boundaries, and because it maintains this value of the flux throughout its calculation, the final solution also depends on these initial conditions. Moreover, the distribution of energy input from the discharge appears to be inconsistent with the electron mean free path. Because the mean free path of the primary electrons is of the order of the length of the source, a uniform deposition

of energy into the production region, with the energy flux at the boundary set approximately to zero, appears to be a better representation.

VI. The Derivation of the Equations of the Model

The basis for the model is Braginskii's derivation [3] of transport equations for two fully ionized fluids (designated by superscripts i and e , where i represents H^+). Glasser and Smith have enhanced these transport equations with additional terms to simulate the effects of the set of chemical reactions listed in Table 2 in Chapter III and the effects of collisions with neutral species (H_2 and H) [9:410]. The *pos* code uses these equations to set up differential equations for the four principal variables (plasma density, drift velocity, electron temperature, and ion temperature) to be solved by the *dirk2* differential equation solver [5].

This chapter contains a general overview of the derivation of the equations of the model. Appendix A gives a detailed derivation of the three velocity moments of the Boltzmann Equation and explains the symbols used in greater detail.

6.1 Development of the Transport Equations

Braginskii's derivation of the transport equations for two fully-ionized fluids begins with the Boltzmann Transport Equation, Equation 1.1 in Braginskii [3:205], for a distribution $f^\alpha(\mathbf{v}, \mathbf{x}, t)$ of a particle of species α :

$$\bar{n}^\alpha \left(\frac{\partial f^\alpha}{\partial t} + v_i \frac{\partial f^\alpha}{\partial x_i} + a_i \frac{\partial f^\alpha}{\partial v_i} \right) = \bar{n}^\alpha \left(\frac{\delta f^\alpha}{\delta t} \right)_{coll} \quad (4)$$

where \bar{n}^α is the average number per volume of particles of species α ; x_i , v_i , and a_i are the i^{th} components of position, velocity, and acceleration, respectively; and $\left(\frac{\delta f^\alpha}{\delta t} \right)_{coll}$ is the effect of collisions. Braginskii successively multiplies Equation 4 by 1, $m^\alpha v_i^\alpha$, and $\frac{1}{2} m^\alpha v_i^\alpha v_i^\alpha$ and integrates over the velocity to obtain, respectively, the *particle transport equation*, the *momentum transport equation*, and the *energy transport equation* for particles of species α .

6.2 The Continuity Equation

Integrating Equation 4 over the velocity gives the particle transport equation, or *continuity equation*, Equation 1.11 in Braginskii [3:208], which is:

$$\frac{\partial n^\alpha}{\partial t} + \frac{\partial (n^\alpha V_i^\alpha)}{\partial x_i^\alpha} = S_{coll}^\alpha \quad (5)$$

where V_i^α is the component of the average velocity of particles of species α in the i^{th} direction and S_{coll}^α is the net production of charged particles (ionization minus recombination). Thus the continuity equation states that the time rate of change of the number density of charged particles in a volume of space is equal to the net flow of particles into that volume plus the net production of particles within the volume. In his derivation, Braginskii assumes no production or annihilation of charged particles in the fully-ionized fluids and thus sets $S_{coll}^\alpha = 0$. On the other hand, the model assumes only charge quasineutrality, $n^e = n^i \equiv n$, so electrons and ions are produced and annihilated in pairs and $S_{coll}^e = S_{coll}^i \equiv S_{coll}$. The model considers production (ionization) from Reaction 19 and loss (recombination) from Reaction 26 in Table 2 or Appendix B, so the net production is:

$$S_{coll} = n^e n^0 k_{19} - n^e n^i k_{26} = n n^0 k_{19} - (n)^2 k_{26} \quad (6)$$

which is Equation 3.6 in Glasser and Smith [9:412].

The model assumes ambipolar drift, $V_z^e = V_z^i \equiv V_z$, where the z -direction is along the axis of the ion source, with $z = 0$ at the filament (cathode) end and $z = z_{max}$ at the extraction end. The one-dimensional form of the continuity equation is thus:

$$\frac{\partial n}{\partial t} + \frac{\partial (n V_z)}{\partial z} = S_{coll} \quad (7)$$

6.3 The Momentum Equation

Multiplying Equation 4 by $m^\alpha v_i^\alpha$ and integrating over the velocity yields the momentum transport equation, or *momentum balance equation*, Equation 1.14 in Braginskii [3:209], which is:

$$n^\alpha m^\alpha \left(\frac{\partial V_i^\alpha}{\partial t} + V_i^\alpha \frac{\partial V_i^\alpha}{\partial x_i^\alpha} \right) = -\frac{\partial p^\alpha \delta_{ij}}{\partial x_i^\alpha} - \frac{\partial \Pi_{ij}^\alpha}{\partial x_i^\alpha} + Z e n^\alpha \left(E_i + \frac{1}{c} [\epsilon_{ijk} V_j^\alpha B_k] \right) + R_j^\alpha \quad (8)$$

where

$$R_j^\alpha \equiv \int \bar{n}^\alpha m^\alpha u_j^\alpha \frac{\delta f^\alpha}{\delta t} \Big|_{coll} d\mathbf{v}^\alpha$$

describes the momentum exchange through collisions.

From Equation 8, Glasser and Smith [9:411] derive a similar one-dimensional form of the momentum transport equation as their Equation 3.2:

$$\underbrace{nm^\alpha \frac{\partial V_z}{\partial t}}_1 + \underbrace{nm^\alpha V_z \frac{\partial V_z}{\partial z}}_2 = -\underbrace{\frac{\partial p^\alpha}{\partial z}}_3 + \underbrace{\frac{\partial \Pi_{zz}^\alpha}{\partial z}}_4 + \underbrace{Z e n E_z}_5 \pm \underbrace{R_z^{\alpha\beta}}_6 + \underbrace{R_z^{\alpha n}}_7 - \underbrace{m^\alpha V_z S_{coll}^\alpha}_8 - \underbrace{d^\alpha V_z}_9 \quad (9)$$

Several features of Equation 9 are evident. First, Braginskii's R_j^α has been taken in the z direction only and extended to include the effects of collisions with neutral particles:

$$R_z^\alpha = \pm R_z^{\alpha\beta} + R_z^{\alpha n} - m^\alpha V_z S_{coll}^\alpha - d^\alpha V_z$$

where $\pm R_z^{\alpha\beta}$ describes the exchange of momentum in the z direction due to collisions between charged particles of species i and e (when $\alpha = e$ in the electron equation, then $\beta = i$; conversely, when $\alpha = i$ in the ion equation, then $\beta = e$), $m^\alpha V_z S_{coll}^\alpha$ describes the exchange of momentum due to the net production of charged particles of species α from collisions with neutral particles, $d^\alpha V_z$ describes the exchange of momentum due to collisions of particles of species α with neutral particles (the drag due to collisions with neutral particles), and $R_z^{\alpha n}$ appears to be a redundant momentum exchange term.

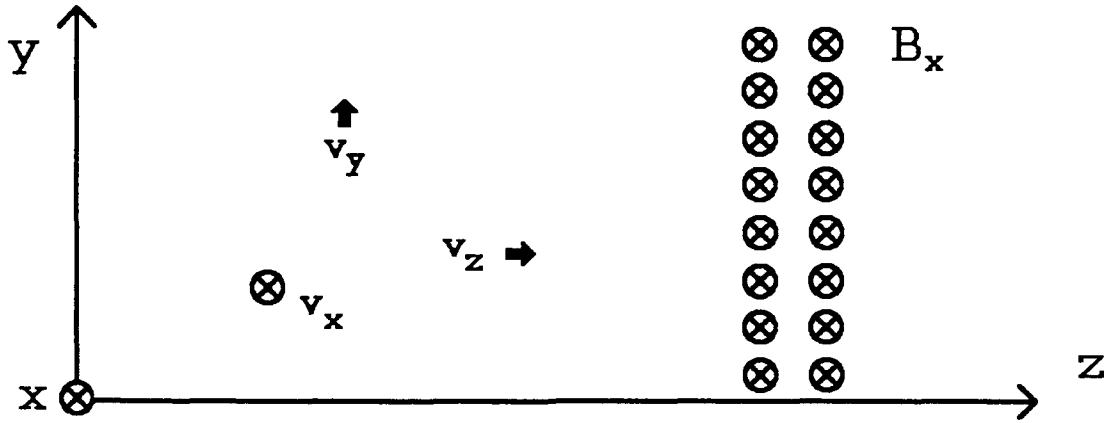


Figure 18. Tandem Volume Source Geometry

A second feature of Equation 9 is that it is missing the term in Equation 8 from the interaction of the velocity with the magnetic filter field, $[\epsilon_{ijk} V_j^\alpha B_k]$. Let the z direction be defined along the central axis of the volume source, from the driver to extraction regions, and let the x direction be aligned with the magnetic filter field in Figure 3 so that the y direction is perpendicular to both the filter field and the axis. Figure 18 depicts this geometry. Since the filter field is applied in one direction only, $B_y = B_z = 0$. Then the only surviving term in the z direction of the interaction between the drift velocity and the filter field $[\epsilon_{ijk} V_j^\alpha B_k]$ is the term $-V_y B_x$. The model assumes that for the one-dimensional case $V_y = 0$. Therefore, the *only* effect of the magnetic filter field enters through the parameter x^α defined by

$$x^\alpha = \omega_c^\alpha \tau^\alpha$$

where ω_c^α is the gyrofrequency of species α and τ^α is the mean time between collisions. The parameter x^α appears in two of the transport coefficients: first, in the j^{th} order coefficients of transport of viscosity, η_j^α :

$$\eta_j^\alpha = n^\alpha T^\alpha \tau^\alpha \mathcal{P}(x^\alpha)$$

where $\mathcal{P}(x^\alpha)$ is a dimensionless polynomial in x^α , and second, in the coefficients of thermal transport in the i^{th} direction, κ_i^α :

$$\kappa_i^\alpha = \frac{n^\alpha T^\alpha \tau^\alpha}{m^\alpha} \mathcal{P}(x^\alpha)$$

The one-dimensional expression in Equation 9 should correspond to similar one-dimensional expressions from other sources. For example, Golant [10:309] gives an expression for steady-state electron and ion motion perpendicular to an applied magnetic field in a fully-ionized plasma:

$$\mp e \mathbf{E}_\perp - \frac{1}{n} \nabla_\perp (n T^\alpha) \mp \frac{e}{c} [\mathbf{V}_\perp^\alpha \times \mathbf{H}] \mp \frac{\bar{\nu}^{ei}}{\omega_H^\alpha} [\mathbf{h} \times \nabla T^e] \mp m^e \bar{\nu}^{ei} (\mathbf{V}_\perp^e - \mathbf{V}_\perp^i) = 0 \quad (10)$$

where the upper signs are for the electron equation ($\alpha = e$) and the lower signs for the ion equation ($\alpha = i$), the symbol \perp represents the directions perpendicular to the magnetic field, the magnetic field intensity \mathbf{H} is related to the magnetic induction \mathbf{B} by $\mu \mathbf{H} = \mathbf{B}$, with μ representing the magnetic permeability, $\bar{\nu}^{ei}$ is the "frequency of electron-ion collisions averaged over the Maxwellian distribution" [10:308], ω_H^α is the cyclotron frequency $\frac{ZeH}{m^\alpha c}$ for species α [10:313], and $\mathbf{h} = \frac{\mathbf{H}}{H} = \frac{\mathbf{B}}{B}$ is a unit vector in the direction of the magnetic field [10:315].

Under the condition of ambipolar diffusion, the mean velocities of the electrons and the ions are approximately equal ($\mathbf{V}_\perp^e \approx \mathbf{V}_\perp^i$), so the last term of Equation 10 is zero. If the x axis lies in the direction of the magnetic field as in Figure 18 so that $B_y = B_z = 0$, then Golant's expression, in indicial notation, becomes two analogous equations, one for motion in the y direction, the other for motion in the z direction:

$$\begin{aligned} ZeE_y - \frac{1}{n} \frac{\partial}{\partial y} (n T^\alpha) + \frac{Ze}{c\mu} [V_z^\alpha B_x]_y + \frac{3}{2} \frac{Z\mu\bar{\nu}^{ei}}{\omega_c^\alpha |B|} \left[-B_x \frac{\partial T^e}{\partial z} \right]_y &= 0 \\ ZeE_z - \frac{1}{n} \frac{\partial}{\partial z} (n T^\alpha) + \frac{Ze}{c\mu} [-V_y^\alpha B_x]_z + \frac{3}{2} \frac{Z\mu\bar{\nu}^{ei}}{\omega_c^\alpha |B|} \left[B_x \frac{\partial T^e}{\partial y} \right]_z &= 0 \end{aligned}$$

where Z is the charge state ($Z = 1$ for ions $Z = -1$ for electrons). If the temperature distribution in the y direction is uniform, then $\frac{\partial T^e}{\partial y} = 0$. Upon multiplying by n , rearranging terms, and applying the ideal gas law $p^\alpha = nT^\alpha$, the equation of motion in the z direction becomes:

$$0 = -\frac{\partial}{\partial z} p^\alpha + ZenE_z + \frac{Ze}{c\mu} [V_y^\alpha B_x]_z \quad (11)$$

A few simplifying assumptions can reduce Equation 9 to a similar form. In a steady-state, the first term is zero. Neglecting the smaller terms of those remaining, Equation 9 becomes

$$\underbrace{0}_1 = -\underbrace{\frac{\partial}{\partial z} p^\alpha}_3 + \underbrace{ZenE_z}_5$$

which is identical to Golant's form in Equation 11 except for the missing $[V_y^\alpha B_x]$ term suggested by Equation 8.

In reality, the magnetic filter doesn't go away. Electrons orbit in the filter, and ions are deflected. Both processes result in velocities in the y direction. Thus $V_y = 0$ is not a good assumption, even in a one-dimensional model.

The third feature of Equation 9 is that it is really two equations, one with $\alpha = e$ and $\beta = i$, the other with $\alpha = i$ and $\beta = e$. Adding these two equations eliminates the electric field, E_z , and the coulomb interaction term, $\pm R_z^{\alpha\beta}$. The resulting equation is Equation 3.4 in Glasser and Smith [9:412], which the model uses as the basis of its differential equation for the drift velocity V_z :

$$\begin{aligned} \frac{\partial V_z}{\partial t} + V_z \frac{\partial V_z}{\partial z} + \frac{1}{m} \sum_\alpha \frac{p^\alpha}{(n)^2} \frac{\partial n}{\partial z} - \frac{4}{3m(n)^2} \frac{\partial V_z}{\partial z} \sum_\alpha \eta^\alpha \tau^\alpha p^\alpha \frac{\partial n}{\partial z} \\ + \frac{1}{m} \frac{\partial}{\partial z} \sum_\alpha \left[\frac{p^\alpha}{n} \left(1 - \frac{4}{3} \eta^\alpha \tau^\alpha \frac{\partial V_z}{\partial z} \right) \right] + \frac{1}{nm} (-R_z^{en} - R_z^{in} + mV_z S_{coll}) + dV_z = 0 \quad (12) \end{aligned}$$

where $m \equiv m^e + m^i$, η^α is the coefficient of viscosity of species α , τ^α is the mean time between collisions for species α , and d is a composite drag defined in Equation 18.

6.4 The Energy Equation

Multiplying Equation 4 by $\frac{1}{2}m^\alpha v_i^\alpha v_i^\alpha$ and integrating over the velocity gives the *energy transport equation*, which is Equation 1.23 in Braginskii [3:210]:

$$\begin{aligned} \frac{\partial}{\partial t} \left(\frac{1}{2} n^\alpha m^\alpha V_j^\alpha V_j^\alpha + \frac{3}{2} n^\alpha T^\alpha \right) + \frac{\partial}{\partial x_i^\alpha} \left\{ \left(\frac{1}{2} n^\alpha m^\alpha V_j^\alpha V_j^\alpha + \frac{5}{2} n^\alpha T^\alpha \right) V_i^\alpha + \right. \\ \left. + (\Pi_{ij}^\alpha V_j^\alpha) + q_i^\alpha \right\} = -Z e n^\alpha E_i V_i^\alpha + \frac{1}{2} m^\alpha V_j^\alpha V_j^\alpha S_{coll}^\alpha + m^\alpha V_j^\alpha R_j^\alpha + Q_{coll}^\alpha \end{aligned} \quad (13)$$

To develop differential equations for the temperatures T^e and T^i the model uses a one-dimensional version of Equation 13 of the form:

$$\begin{aligned} \frac{3}{2} n \frac{\partial T^\alpha}{\partial t} + \frac{3}{2} n V_z \frac{\partial T^\alpha}{\partial z} + p^\alpha \frac{\partial V_z}{\partial z} = \frac{1}{m^\alpha} \frac{\partial}{\partial z} \left(\kappa^\alpha n T^\alpha \tau^\alpha \frac{\partial T^\alpha}{\partial z} \right) \\ + \frac{4}{3} \eta^\alpha n T^\alpha \tau^\alpha \left(\frac{\partial V_z}{\partial z} \right)^2 - Q^\alpha + Q_{sink}^\alpha + V_z R^{\alpha n} - \frac{3}{2} T^\alpha S_{coll} + \frac{1}{2} m^\alpha (v)^2 S_{coll} \end{aligned} \quad (14)$$

where κ^α is the thermal conductivity of species α , Q_{sink}^α is an energy "sink" [9:412] due to radiation from and chemical reactions involving species α , and Q^α is the rate of heat transfer to species α , defined as

$$Q^\alpha = Q^{\alpha\beta} + Q^{\alpha n}$$

where $Q^{\alpha\beta}$ is the rate of transfer from charged species β to charged species α , and $Q^{\alpha n}$ is the rate of transfer from neutral particles to species α .

6.5 Differential Equations

The computer code stores each of the primary variables n , V_z , T^e , T^i , and z as a subarray of j elements in the i^{th} row of the array y_{ij} (the variable $y(i, j)$ in the computer code), where j is the number of the integration bin. Thus $y_{1j} = n_j$, $y_{2j} = (V_z)_j$, $y_{3j} = T_j^e$, $y_{4j} = T_j^i$, and $y_{5j} = z_j$. The model solves for the component variables and isolates the time dependence of the one-dimensional

moment equations above to develop, for each of the four primary variables y_i , differential equations of the form given in Equation 4.1 in Glasser and Smith [9:413]:

$$\frac{\partial y_i}{\partial t} = S_i - \frac{\partial F_i}{\partial z}$$

where S_i is a matrix of source terms, and F_i is a matrix of flux terms defined by Equation 4.2 in Glasser and Smith [9:413]:

$$F_i = C_i - D_i \frac{\partial y_i}{\partial z}$$

The *pos* code then exports these differential equations to the *dirk2* code that solves them.

6.6 Numerical Approach

The *dirk2* code uses a diagonally implicit Runge-Kutta method of order 2 and the method of moving finite elements to solve the differential equations supplied by the model. The method of moving finite elements concentrates integration "bins" at inflection points where the second derivatives of the primary variables are the greatest. Thus calculations in regions where the gradients of the primary variables are changing sharply use a finer integration mesh, and calculations in regions where the gradients of the primary variables change relatively little use a coarser mesh. By means of this method, the model achieves greater computational accuracy for any given number of bins.

6.7 Conclusion to Derivation of the Equations

Thus Glasser and Smith implement Braginskii's derivation, from the velocity moments of the Boltzmann equation, of transport equations for two fully ionized fluids in one dimension as the basis for the model. In the course of review of the derivations, three inconsistencies were identified, where the equations implemented in the model do not match the derivations. These inconsistencies are the subject of Chapter VII.

VII. Inconsistencies in the Derivation of the Equations

There are three inconsistencies in the model where the derivation and coding of the differential equations for the four primary variables in the model differ from the one-dimensional velocity moment equations adapted from Braginskii. This chapter identifies these three inconsistencies, describes the attempts to correct them, and presents the results of those attempts.

7.1 Omitted Momentum Term in the Model

The first inconsistency is that in lines 114, 127, and 128 of the module *fluxes* the computer code omits the term for momentum exchange between ions and neutral particles, R^{in} , from the second dissipative source term, S_2^d , included in Equation 4.12 in Glasser and Smith [9:414]:

$$S_2^d = -D_2 \frac{1}{n} \frac{\partial n}{\partial z} - dv + \frac{1}{m^i n} \left(R^{en} + \underbrace{R^{in}}_{\text{omitted}} - m^i v S_{coll} \right) \quad (15)$$

7.2 Extra Temperature Gradient in the Model

The second inconsistency is that in setting up the differential equations for temperature, the implementation of the computer code squares the temperature gradient in one term of the energy transport equation. Instead of the correct form given by Equation 14, the equation actually implemented in the computer code is:

$$\begin{aligned} \frac{3}{2} n \frac{\partial T^\alpha}{\partial t} + \frac{3}{2} n V_z \frac{\partial T^\alpha}{\partial z} + n T^\alpha \frac{\partial V_z}{\partial z} &= \frac{1}{m^\alpha} n \frac{\partial}{\partial z} \left(\kappa^\alpha n T^\alpha \tau^\alpha \frac{\partial T^\alpha}{\partial z} \underbrace{\frac{\partial T^\alpha}{\partial z}}_{\text{added}} \right) + \frac{1}{m^\alpha} \kappa^\alpha n T^\alpha \tau^\alpha \frac{\partial T^\alpha}{\partial z} \frac{\partial n}{\partial z} \\ &+ \frac{4}{3} \eta^\alpha n T^\alpha \tau^\alpha \left(\frac{\partial V_z}{\partial z} \right)^2 - Q^\alpha + Q_{sink}^\alpha - V_z R^{\alpha n} - \frac{3}{2} T^\alpha S_{coll} + \frac{1}{2} m^\alpha (v)^2 S_{coll} \end{aligned} \quad (16)$$

Dimensional analysis shows that the form of the fourth term is correct in Equation 14, not in Equation 16. If $[\ell]$ represents a dimension of length, $[m]$ of mass, and $[t]$ of time, then the first

term of Equations 14 and 16 shows that they have dimensions of power density:

$$\left[\frac{3}{2} n \frac{\partial T^\alpha}{\partial t} \right] \sim [n] \frac{[T]}{[t]} = \left[\frac{1}{\ell^3} \right] \frac{[m(\ell/t)^2]}{[t]} = \left[\frac{m}{\ell t^3} \right]$$

The fourth term in Equation 14 also has dimensions of power density:

$$\left[\frac{1}{m^\alpha} \frac{\partial}{\partial z} \left(\kappa^\alpha n T^\alpha \tau^\alpha \frac{\partial T^\alpha}{\partial z} \right) \right] \sim \left[\frac{1}{m} \right] \left[\frac{1}{\ell} \right] [1] \left[\frac{1}{\ell^3} \right] \left[m \frac{\ell^2}{t^2} \right] [t] \left[\frac{m \ell^2 / t^2}{\ell} \right] = \left[\frac{m}{\ell t^3} \right]$$

as required. Thus multiplication by the “added” gradient of the temperature in Equation 16 is incorrect.

7.3 Extra Velocity Gradient in the Model

The third inconsistency occurs in the derivation of the differential equation for V_z from the sum of the one-dimensional momentum equations. Instead of implementing the momentum equation in the form of Equation 12, the computer code implements it with the gradient of the velocity squared:

$$\begin{aligned} & \frac{\partial V_z}{\partial t} + V_z \frac{\partial V_z}{\partial z} + \frac{1}{m} \sum_\alpha \frac{p^\alpha}{(n)^\alpha} \frac{\partial n}{\partial z} - \frac{4}{3m(n)^2} \frac{\partial V_z}{\partial z} \sum_\alpha \eta^\alpha \tau^\alpha p^\alpha \frac{\partial n}{\partial z} \\ & + \frac{1}{m} \frac{\partial}{\partial z} \sum_\alpha \left[\frac{p^\alpha}{n} \left(1 - \frac{4}{3} \eta^\alpha \tau^\alpha \frac{\partial V_z}{\partial z} \underbrace{\frac{\partial V_z}{\partial z}}_{\text{added}} \right) \right] + \frac{1}{nm} (-R_z^{en} - R_z^{in} + m V_z S_{coll}) - dV_z \quad (17) \end{aligned}$$

Once again dimensional analysis shows that the form developed in Section 6.1 as Equation 12 is correct. The dimensions of the first terms in Equations 12 and 17 are dimensions of acceleration:

$$\left[\frac{\partial V_z}{\partial t} \right] \sim \left[\frac{v}{t} \right] = \left[\frac{\ell/t}{t} \right] = \left[\frac{\ell}{t^2} \right]$$

The leading terms in front of the parentheses in the fifth term in Equations 12 and 17 have dimensions of

$$\left[\frac{1}{m} \frac{\partial}{\partial z} \sum_{\alpha} \frac{p^{\alpha}}{n} \right] \sim \left[\frac{1}{m} \right] \left[\frac{1}{z} \right] [T] = \left[\frac{1}{m} \right] \left[\frac{1}{\ell} \right] \left[m \frac{\ell^2}{t^2} \right] = \left[\frac{\ell}{t^2} \right]$$

which are also dimensions of acceleration, so the quantity inside parentheses in the fifth term must be dimensionless. There is also a simpler way to see this. For the two expressions inside the parentheses to be subtracted, they must have the same dimensions. Since 1 is dimensionless, $\frac{4}{3} \eta^{\alpha} \tau^{\alpha} \frac{\partial V_z}{\partial z}$ must be dimensionless, too. Its dimensions are

$$\left[\frac{4}{3} \eta^{\alpha} \tau^{\alpha} \frac{\partial V_z}{\partial z} \right] \sim [1] [1] [t] \left[\frac{\ell/t}{\ell} \right] = [1]$$

Thus the correct dimensionless term is the one without the extra gradient of velocity.

7.4 Attempts to Correct Inconsistencies in the Equations

Correcting the first inconsistency by adding the missing R^{in} term (*sc (3, j)* in the computer code) back into the equation for S_2^d (*dsource (2, j)* in the computer code) is simple. The modification changed lines 127 and 128 of the module *fluxes* from

```
127      dsource(2,j)=dsource(2,j)
128      2  +(sc(2,j)-mi*yy(2,j)*sc(1,j))/(mi*yy(1,j))
```

to

```
127      dsource(2,j)=dsource(2,j)
128      2  +(sc(2,j)+sc(3,j)-mi*yy(2,j)*sc(1,j))/(mi*yy(1,j))
```

where the *sc (3, j)* term has been added to the continuation line.

Correcting the second and third inconsistencies was a more involved matter because the code divides the equations up differently from the way the derivations do. Simply dividing through by

the extra terms where they appear resulted in "divide by zero" errors. For example, the first call of the subroutine *fluxes* occurs while the drift velocity is still initialized to zero, so the velocity cannot be a divisor. This problem was avoided by not dividing by the terms to be removed; instead, the extra terms were removed from variables where they were multiplicative factors. So as not to alter other expressions derived from these variables, the terms had to be multiplied back in at other places.

For example, to correct the second inconsistency, removing the extra temperature gradients from the energy equations required changing lines 109 through 110 and 115 through 118 of the *fluxes* module. The unmodified code read:

```

109      qte=-chiprpe(j)*boltz*te1
110      qti=-chiprpi(j)*boltz*ti1
...
115      dsource(3,j)=-(boltz*(qeifac(j)*(te-ti)+qe0fac(j)*(te-temp0))
116      2  +pizze*v1+qte*(den1/den))/(1.5*boltz*den)
117      dsource(4,j)=-(boltz*(qeifac(j)*(ti-te)+qi0fac(j)*(ti-temp0))
118      2  +pizzi*v1+qti*(den1/den))/(1.5*boltz*den)

```

The modification removes the two gradient terms *te1* and *ti1* from *qte* and *qti* in lines 109 and 110 and adds them back into *dsource* (3, *j*) and *dsource* (4, *j*) in lines 115 through 118.

```

109      qte=-chiprpe(j)*boltz
110      qti=-chiprpi(j)*boltz
...
115      dsource(3,j)=-(boltz*(qeifac(j)*(te-ti)+qe0fac(j)*(te-temp0))
116      2  +pizze*v1+(qte*te1)*(den1/den))/(1.5*boltz*den)
117      dsource(4,j)=-(boltz*(qeifac(j)*(ti-te)+qi0fac(j)*(ti-temp0))
118      2  +pizzi*v1+(qti*ti1)*(den1/den))/(1.5*boltz*den)

```

The modification had the same effect as dividing the terms *dflux* (3, *j*) and *dflux* (4, *j*) in lines 112 and 113 by *te1* and *te2* respectively, but without the "divide by zero" error in the initial call of *fluxes*.

The correction of the third inconsistency required dividing the gradient of the velocity $\frac{\partial v}{\partial z}$ (*v1* in the computer code) out of *D₂* (*dflux* (2, *j*) in the computer code). To avoid the error on

the initial call, $v1$ was removed from $pizze$ (Π_{zz}^e) and $pizzi$ (Π_{zz}^i) in lines 106 and 107 of *fluxes*. To compensate for removing $v1$ from the Π_{zz}^a terms, $v1$ was multiplied back into $dsource$ ($2, j$) (S_2^d), $dsource$ ($3, j$) (S_3^d), and $dsource$ ($4, j$) (S_4^d). The original code was:

```

106     pizze=-fourby3*(etae0(j)/3.+etae1(j))*v1
107     pizzi=-fourby3*(etai0(j)/3.+etai1(j))*v1
108     pizz=pizze+pizzi
109     qte=-chiprpe(j)*boltz*te1
110     qti=-chiprpi(j)*boltz*ti1
111     dflux(2,j)=pizz/(den*mi)
112     dflux(3,j)=qte/(1.5*boltz*den)
113     dflux(4,j)=qti/(1.5*boltz*den)
114     dsource(2,j)=-dflux(2,j)*(den1/den)-drag(j)*v
115     dsource(3,j)=- (boltz*(qeifac(j)*(te-ti)+qe0fac(j)*(te-temp0))
116 2   +pizze*v1+qte*(den1/den))/(1.5*boltz*den)
117     dsource(4,j)=- (boltz*(qeifac(j)*(ti-te)+qi0fac(j)*(ti-temp0))
118 2   +pizzi*v1+qti*(den1/den))/(1.5*boltz*den)

```

After removing $v1$ from $dflux$ ($2, j$), the modified code was:

```

106     pizze=-fourby3*(etae0(j)/3.+etae1(j))
107     pizzi=-fourby3*(etai0(j)/3.+etai1(j))
108     pizz=pizze+pizzi
109     qte=-chiprpe(j)*boltz*te1
110     qti=-chiprpi(j)*boltz*ti1
111     dflux(2,j)=pizz/(den*mi)
112     dflux(3,j)=qte/(1.5*boltz*den)
113     dflux(4,j)=qti/(1.5*boltz*den)
114     dsource(2,j)=-dflux(2,j)*v1*(den1/den)-drag(j)*v
115     dsource(3,j)=- (boltz*(qeifac(j)*(te-ti)+qe0fac(j)*(te-temp0))
116 2   +pizze*v1+qte*(den1/den))/(1.5*boltz*den)
117     dsource(4,j)=- (boltz*(qeifac(j)*(ti-te)+qi0fac(j)*(ti-temp0))
118 2   +pizzi*v1+qti*(den1/den))/(1.5*boltz*den)

```

7.5 Results of Modifications to Terms in the Equations

With the term R^{in} added into the expression for S_a^2 , the model ran for all 25 cycles and converged to a solution. For the test case parameters there was no noticeable difference between the results with the term R^{in} and without the term R^{in} .

When run with the extra temperature gradient terms removed from the differential equations for temperature, the model evidently suffered a strong interaction with one of the outflow boundary conditions which led to numerical instabilities. The symptoms were an increase in electron temperature of over two orders of magnitude in the 40th (rightmost) integration bin which led to a decrease in the integration time step in *dirk2* beyond its lower bound of 1.0×10^{-11} sec.

Running the model with the extra velocity gradient term removed caused rather different behavior. The model ran for over $16\frac{1}{2}$ hours but completed only 5 time cycles. At the onset of numerical instability during the fifth time cycle, there was a sharp discontinuity in the density profile and several smaller discontinuities in the velocity profile. Evidently, these forced the integrator to smaller and smaller time steps until it exceeded its lower bound of 1.0×10^{-11} sec.

7.6 *Conclusions from the Results of Modifications*

Since there is no noticeable difference between runs that include and runs that exclude the term R^{in} , it is apparently negligible for the parameters of the published results.

The sharp increase in electron temperature in the outermost bin observed during the run without the extra temperature gradient terms was typical of the onset of numerical instabilities in the model. Future work with this model should isolate the boundary condition responsible and investigate the nature of the interaction.

The model contains user-input stability factors in the terms for the dissipative fluxes. It may be possible to adjust the stability terms built into the model to make the modified equations stable.

VIII. Enhancements to the Model.

To enhance the information provided by the model and to allow comparisons (1) between this model and experiment and (2) between this model and other models, the output was extended to calculate four additional variables: the electron flux, the electric field, the electrical potential, and the electron pressure.

8.1 Electron Flux

In addition to the four basic macroscopic quantities that the model calculates, the plasma density, drift velocity, electron temperature, and ion temperature, another basic property of a plasma is the electron flux, Γ_i^e , defined by $\Gamma_i^e = n^e V_i^e$ [21:83]. The model assumes (1) a quasineutral plasma so that $n^e = n^i$ and (2) ambipolar diffusion so that $V_i^e = V_i^i$. Thus $\Gamma_i^e = n^e V_i^e = n^i V_i^i = \Gamma_i^i$, so the electron and ion fluxes are equal. The continuity equation, Equation 46 in Appendix A, shows that

$$\frac{\partial n^\alpha}{\partial t} + \frac{\partial n^\alpha V_i^\alpha}{\partial x_i^\alpha} = S_{coll}^\alpha$$

Because for every electron created, there is an ion created, $S_{coll}^e = S_{coll}^i$. In steady state, there is no change in time, so in one dimension:

$$\frac{\partial \Gamma_z}{\partial z} = S_{coll}$$

Thus the slope of the electron flux curve gives a measure of the net production in the plasma.

Figure 19 shows the particle flux for the steady state. The slope, and hence the net production S_{coll} , is roughly constant from $z = 0$ to $z = 20.4 \text{ cm}$. From $z = 20.4 \text{ cm}$ to $z = 25 \text{ cm}$, the slope is shallower, corresponding to a somewhat smaller value of S_{coll} . Because in a real tandem volume ion source the magnetic filter field confines the ionizing primary electrons to the production region,

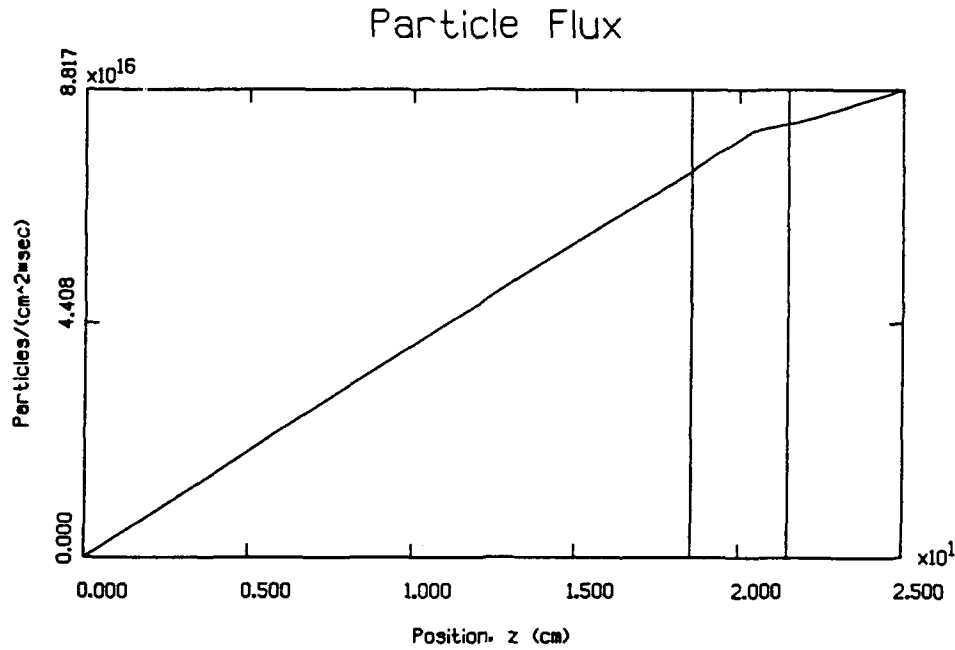


Figure 19. Charged Particle Flux.

one would intuitively expect the net production to be smaller in the extraction region. In this case the results from the model behave as intuition suggests.

However, as Section 6.3 demonstrated, the effect of the magnetic filter field is not included explicitly in the model, but enters only indirectly through the transport coefficients. This enhancement to the model does not calculate the flux as the integral of the production term S_{coll} , but as the product of the density (in Figures 11 and 14) and the drift velocity (in Figure 11).

8.2 The Electric Field

Another enhancement to the model calculated the electric field by three different methods, and graphed the results for comparison. The first method solved for the electric field from the ion momentum equation, the second method solved for the electric field from the electron momentum equation, and the third method solved for the electric field from the difference of the two momentum equations.

The electric field in terms of the ion equation [35] is:

$$\begin{aligned}
 enE_j = & \underbrace{m^i n_j V_z)_j \frac{\partial V_z}{\partial z}}_2 + \underbrace{\frac{n_{(j+1)} T_{(j+1)}^i - n_j T_j^i}{z_{(j+1)} - z_j}}_3 \\
 & - \underbrace{\frac{4}{3} \frac{\eta_{(j+1)}^i n_{(j+1)} T_{(j+1)}^i \tau_{(j+1)}^i \frac{\partial V_z}{\partial z}}_{(j+1)} - \eta_j^i n_j T_j^i \tau_j^i \frac{\partial V_z}{\partial z}}_4 \\
 & + \underbrace{(-R_j^{in})}_7 + \underbrace{m^i V_z)_j S_j}_8 + \underbrace{\frac{n_j m^i}{\tau_j^{in}} V_z)_j}_9
 \end{aligned}$$

where subscript j indicates a quantity calculated in the j^{th} integration bin, and the numbers of the terms correspond to the numbers of the terms in Equation 9 in Chapter VI.

Solving for the electric field from the electron momentum equation yields:

$$\begin{aligned}
 enE_j = & \underbrace{-m^e n_j V_z)_j \frac{\partial V_z}{\partial z}}_2 - \underbrace{\frac{n_{(j+1)} T_{(j+1)}^e - n_j T_j^e}{z_{(j+1)} - z_j}}_3 \\
 & + \underbrace{\frac{4}{3} \frac{\eta_{(j+1)}^e n_{(j+1)} T_{(j+1)}^e \tau_{(j+1)}^e \frac{\partial V_z}{\partial z}}_{(j+1)} - \eta_j^e n_j T_j^e \tau_j^e \frac{\partial V_z}{\partial z}}_4 \\
 & + \underbrace{R_j^{en}}_7 - \underbrace{m^e V_z)_j S_j}_8 - \underbrace{\frac{n_j m^e}{\tau_j^{en}} V_z)_j}_9
 \end{aligned}$$

Similarly, the electric field in terms of the difference of the two momentum equations is:

$$\begin{aligned}
 enE_j = & \underbrace{\frac{1}{2} (m^i - m^e) n_j V_z)_j \frac{\partial v}{\partial z}}_2 \\
 & + \underbrace{\frac{1}{2} \left\{ n_j \left[\frac{\partial T^i}{\partial z} \right)_j - \frac{\partial T^e}{\partial z} \right)_j + \frac{\partial n}{\partial z} \right)_j (T_j^i - T_j^e) \right\}}_3
 \end{aligned}$$

$$\begin{aligned}
& + \frac{2}{3} \left\{ \underbrace{\left(\frac{\partial n}{\partial z} \right)_j \left(\frac{\partial v}{\partial z} \right)_j (\eta^e T^e \tau^e - \eta^i T^i \tau^i)_j}_{4a} + \underbrace{n_j \frac{\partial}{\partial z} \left(\frac{\partial v}{\partial z} \right)_j (\eta^e T^e \tau^e - \eta^i T^i \tau^i)_j}_{4b} \right. \\
& + \left. \underbrace{n_j \frac{\partial v}{\partial z} \right)_j \frac{(\eta^e T^e \tau^e - \eta^i T^i \tau^i)_{j+1} - (\eta^e T^e \tau^e - \eta^i T^i \tau^i)_j}{z_{(j+1)} - z_j}}_{4c} \Bigg\} \\
& + \underbrace{\frac{1}{2}(R_j^{en} - R_j^{in})}_7 + \underbrace{\frac{1}{2}(m^i - m^e) V_z)_j S_j}_8 + \underbrace{\frac{1}{2} n_j \left(\frac{m^i}{\tau_j^{in}} - \frac{m^e}{\tau_j^{en}} \right) V_z)_j}_9
\end{aligned}$$

Figure 20 gives the results of the three different methods of calculating the electric field and an additional graph of the average of the three methods. The general shape of each of the four graphs is similar: a slow linear rise in the production region, a sharp and abrupt peak in the magnetic filter region, where in a real source charged particles are trapped or deflected by the magnetic field, and a return to the slow linear rise in the extraction region. The lower left graph in Figure 20, labelled "(ion)," shows the electric field derived from the ion equation. It is smooth and regular and is dominated by the ion drag term (Term 8) [35]. In contrast, the lower right graph in Figure 20, labelled "(electron)" and derived from the electron momentum equation, is jagged and irregular. It is dominated by the pressure term (Term 3). Why there should be such a large difference in the appearance of the graphs is unknown, as is the reason for the sharp downward spike at 20.3 cm. The upper right graph in Figure 20, labelled "(difference)," shows the electric field calculated from the difference of the two momentum equations. The appearance of this graph is intermediate between the electron and ion graphs. The upper left graph, labelled "(average)," is an average of the three methods of calculating the electric field.

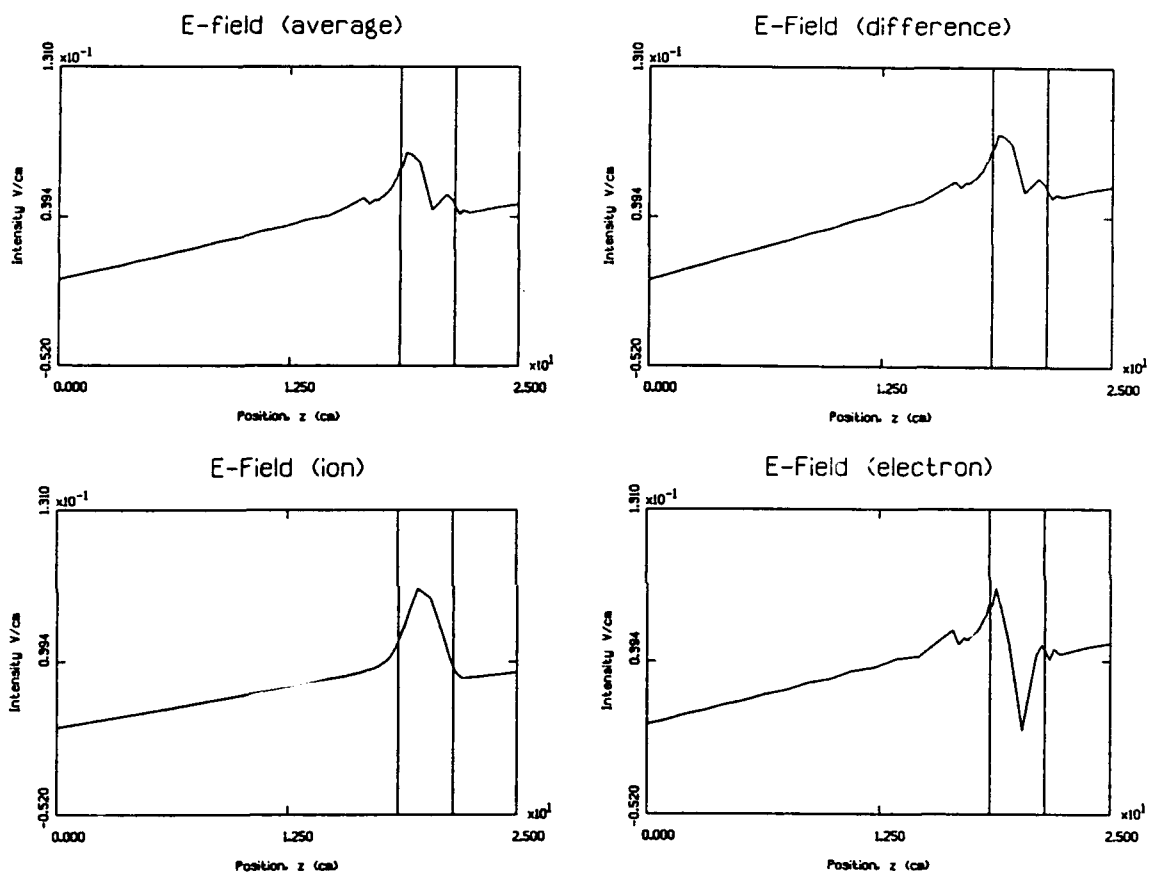


Figure 20. The Electric Field. Counter-clockwise from lower left: the electric field calculated from: (1) the ion momentum equation ("ion"), (2) the electron momentum equation ("electron"), (3) the difference of the two momentum equations ("difference"), and (4) an average of the three methods ("average"). The filament cathodes are located at $z = 0$, and vertical lines mark the $1/e$ points of the magnetic filter field.

8.3 The Potential

Since the relationship between the electric field in the i^{th} direction E_i and the potential Φ is

$$E_i = -\frac{\partial \Phi}{\partial x_i}$$

the potential in the one-dimensional model is

$$\Phi = -\int_z E_z dz$$

Therefore, summing the contributions of the electric field from each bin from $j = 0$ to $j = j_0$ approximates the potential at the location of bin j_0 . Figure 21 compares the potential calculated from the one-dimensional model with a graph of experimental values of the plasma potential from Johnson [18:168]. The enhancement to the model calculates the electrical potential from each of the four methods of calculating the electric field. Figure 21 displays the potential calculated from the electric field derived from the ion momentum equation (labelled "ion" in Figure 20) because the graph of that method of calculating the electric field is the smoothest. Because the process of integration itself is a smoothing process, the potential curves calculated from the other methods are indistinguishable from the one displayed in Figure 21.

The model's calculation of the potential appears to agree well both qualitatively and quantitatively with the trend of experimental data. Where the model calculates a $1\frac{1}{4}$ volt in potential from the cathode to the extraction anode, experiment shows a drop of just under 2 volts. Since the potential is the integral of the electric field, the zero point depends on the choice of the constant of integration. Thus the potential is a relative quantity, and the scale values are arbitrary. For simplicity, this enhancement chose an integration constant of zero.

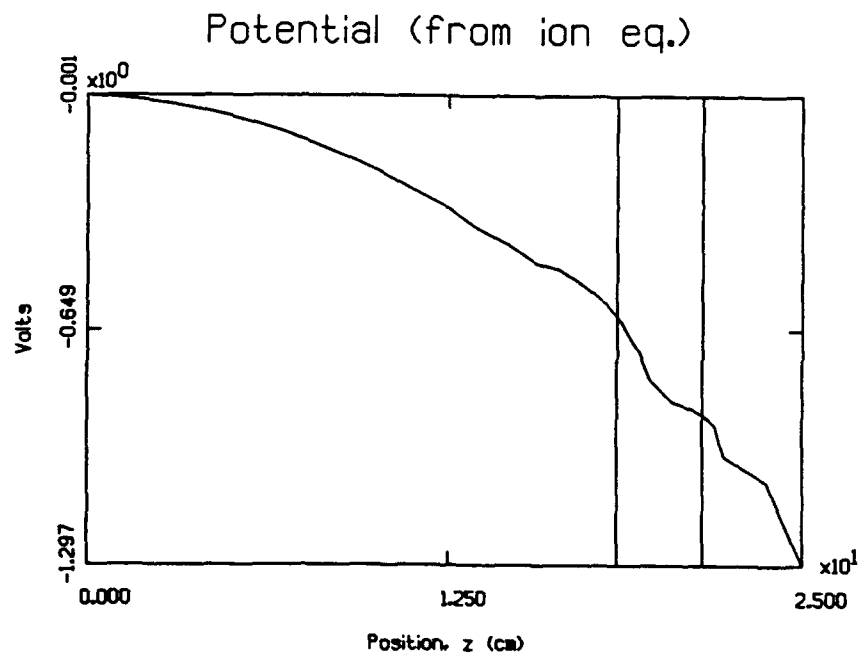
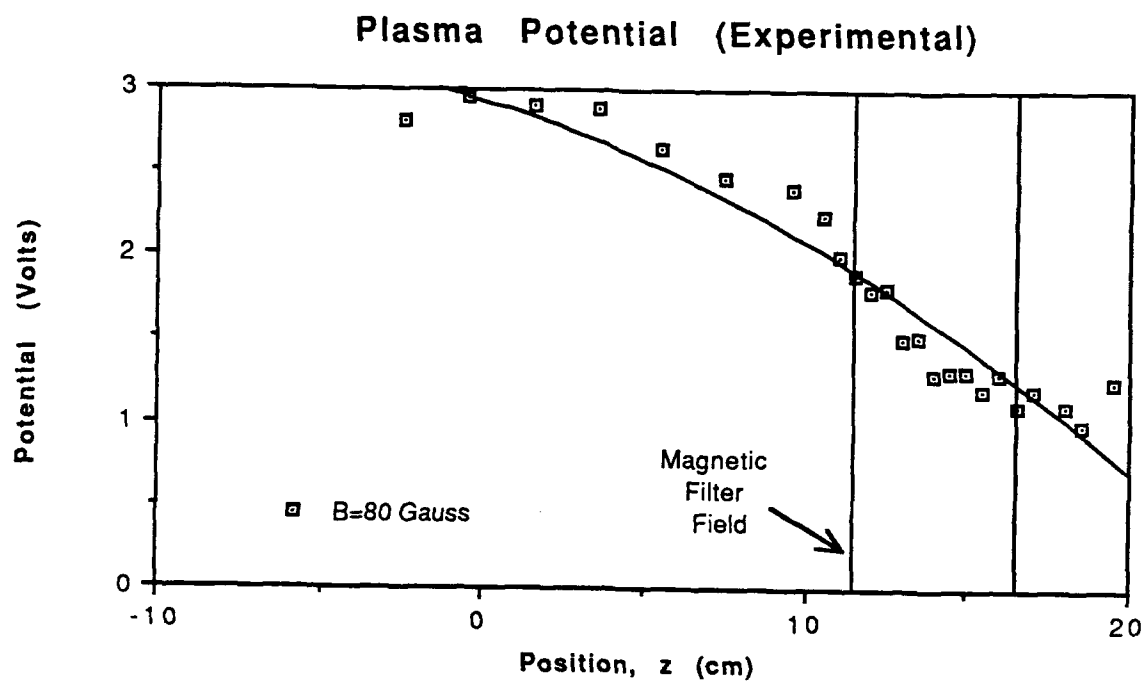


Figure 21. Plasma Potential: Experimental Data (Top) from Johnson [18:168] Compared to Calculation by the Model (Bottom). In both graphs, the filament cathodes are located at $z = 0$, and vertical lines mark the $1/e$ points of the magnetic filter field.

8.4 The Electron Pressure

Another important parameter in an ion source is the electron pressure, p^e , which is defined by

$$p^e \equiv n^e T^e$$

Johnson [18:163] explains why this is an important parameter:

If small numerical constants from the implied average over the electron distribution function are ignored, this parameter can be said to represent the energy density, in eV cm^{-3} , of the bulk plasma.

Figure 22 shows results of calculations of the electron pressure from the one-dimensional model compared with experimental results of the electron pressure from Johnson [18:164].

The general trend from high electron pressure in the production region to low electron pressure in the extraction region that the model calculates agrees with the trend in the experimental data; however, the shape and magnitude of the decline are different¹. The magnitude of the decline that the model calculates is small (just over 15%), where the magnitude of the decline in the experimental data is almost two orders of magnitude.

¹ Coincidentally, the shape of the electron pressure curve that the model calculates is very similar to the *logarithm* of the experimental data.

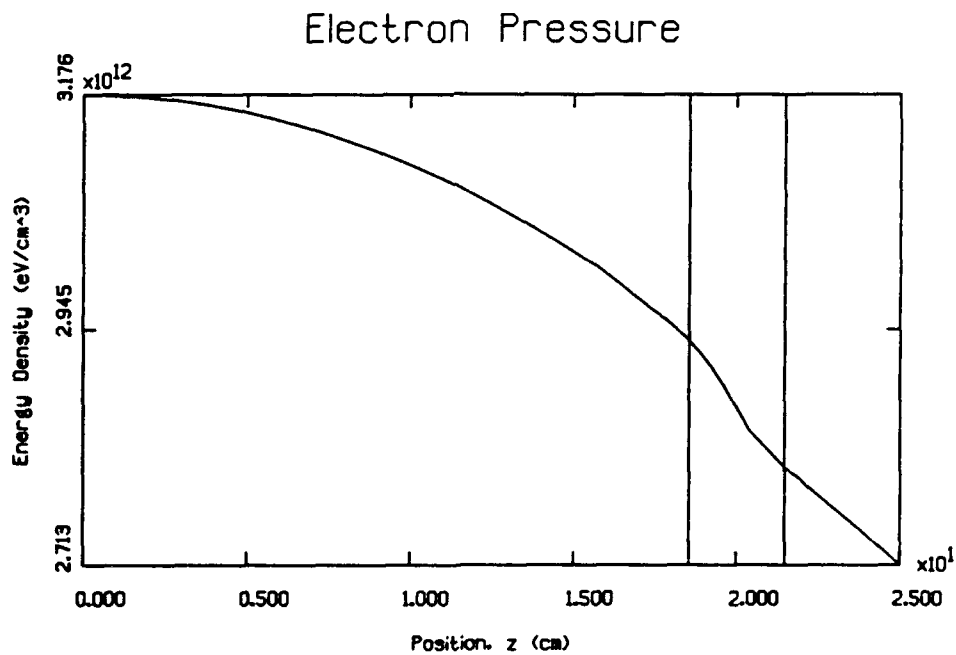
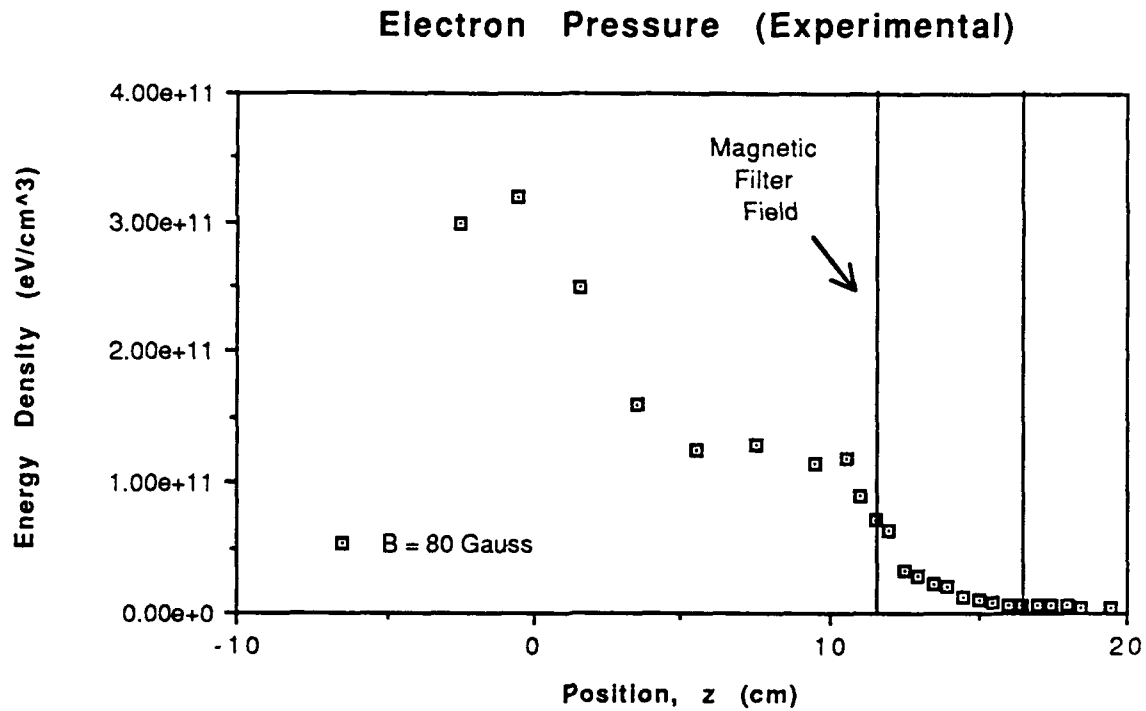


Figure 22. Electron Pressure (Energy Density): Experimental Data (Top) from Johnson [18:164] vs. Calculations by the Model (Bottom). In both graphs, the filament cathodes are located at $z = 0$, and vertical lines mark the $1/e$ points of the magnetic filter field.

IX. Conclusions and Recommendations

9.1 Conclusions

The one-dimensional plasma fluid model studied in this thesis has a lot of potential: The ability of the method of moving finite elements to concentrate computational power where it is needed is attractive. The derivation of most of the equations upon which the model is based has been verified. The FORTRAN code is well-written and portable, and it is designed to allow additional reactions to be included and additional parameters to be calculated with only minor changes. On the other hand, the utility of the model is limited by several factors.

(1) The results out of the current model are unphysical. The model predicts plasma density higher in the extraction region than in the production region, opposite from experimental results. Moreover, it predicts an electron temperature almost an order of magnitude larger than that experimentally observed.

(2) The simplification of the reaction chemistry used to develop the model causes the model to neglect the principal paths of ionization and recombination. The resulting plasma balance between ionization and outflow is incorrect, where the correct balance would be between ionization and recombination.

(3) The model neglects wall losses.

(4) There are inconsistencies in the derivations of some equations, leading to extra terms in the momentum and temperature equations.

(5) The method used to calculate the energy flux at the left boundary makes the final solution depend on the choice of the initial guess at a solution.

(6) For an unknown reason, multiple runs of the model do not reproduce the same results.

(7) When terms in the equations are modified or when initial conditions are varied outside of a relatively narrow range, the model develops numerical instabilities.

If these limitations can be remedied, the code could become a very useful tool in the study of volume tandem magnetic multicusp ion sources.

Although the reason that the model predicts a plasma density that trends opposite to experiment is still unknown, the incorrect electron temperature can be explained in terms of the processes occurring within the model. The model is apparently driven by an outflow boundary condition at the extraction end. Because the model limits the production of plasma to the ionization of atomic hydrogen H , and because it neglects the distinction between hot primary electrons and thermalized secondary electrons, the outflow boundary condition requires a greater production than secondary electrons can achieve at experimentally observed temperatures of about 1 eV . The model compensates by raising its electron temperature to about 7 eV to achieve the required production. The reaction rate for the ionization of atomic hydrogen rises almost six orders of magnitude between 1 eV and 7 eV , and the production matches the required outflow at this point.

The population of hot primary electrons accomplishes most of the ionization in a real ion source through ionization reactions with *both* H and H_2 . Moreover, the loss mechanism in a real source includes recombination reactions with H_2^+ and H_3^+ as well as H^+ . The recombination rates for the dissociative recombination reactions with H_2^+ and H_3^+ are six orders of magnitude larger than the radiative recombination rate with H^+ , so that the balance in a real source is between production and loss. By neglecting the principal plasma loss mechanisms, the model achieves an incorrect balance between production and outflow.

The tendency of the model to develop numerical instabilities made implementing modifications much more difficult than anticipated. This tendency slowed the investigation and limited the achievement of the objectives outlined at the beginning. However, further study may provide the needed breakthrough to overcome the limitations that this study has identified.

9.2 Recommendations

A number of recommendations for further study follow directly from the conclusions above. Although the model does show a great deal of promise, it has many limitations, and any future investigator should weigh carefully the costs and benefits of continued investigation.

9.2.1 Reproducible Results. The most important avenue for further investigation into the model is to determine the cause of the variation between different runs of the model with identical inputs. Until the cause of this behavior can be identified and corrected, the model can be of little use.

9.2.2 Boundary Conditions. The boundary conditions seem to be one of the main keys to the performance of the model. Further research should more explicitly identify the boundary conditions and where they are applied in the code. Identification of the boundary conditions and how they affect the code would allow a greater variety of modifications, which would hopefully yield insight into the physics behind the model.

9.2.3 Stability Terms. Another important area for further investigation is the effect of the stability terms introduced to accelerate convergence of the fluid equations. Understanding the behavior of these terms may provide the means to overcome the tendency of the model to develop numerical instabilities when the terms of the equations are modified and when the initial conditions are varied outside of a narrow range.

9.2.4 Wall Losses. An accurate model of a tandem volume ion source must account for wall losses. It may be possible to include a wall loss term developed in a manner similar to that in Johnson [18:41-42].

9.2.5 Energy Input. A relatively simple enhancement to the model would be a modified energy input term based on the discharge parameters of current I and voltage V . Section 5.2

pointed out that the energy input should be into the entire production volume \mathcal{V} , not just into the first integration bin, because the length of the electron mean free path is of the order of the length of the device. Thus the energy input term would have the form:

$$\varepsilon_{in} \propto \frac{IV}{\mathcal{V}}$$

9.2.6 Inclusion of a B-Field Term. In the momentum transport equation, Equation 1.14 in Braginskii [3:209], there is a term that includes the magnitude B of the magnetic filter field:

$$m^\alpha n \frac{dV_i^\alpha}{dt} = -\frac{\partial p^\alpha}{\partial x_i} - \frac{\partial \Pi_{ij}^\alpha}{\partial x_i} + en \left(E_i + \underbrace{\frac{1}{c} [\epsilon_{ijk} V_j^\alpha B_k]}_{\text{filter field term}} \right) + R_i$$

When Glasser and Smith adapt this three-dimensional equation into their one-dimensional Equation 3.2, the term for the magnetic filter field disappears. In a one-dimensional model, the cross product of the drift velocity in the z direction and the magnetic field in the x direction is in the y direction and thus out of axial direction to which the model limits itself. So the only remaining effect of the magnetic filter enters through the transport coefficients. However, there are velocities in the perpendicular directions that cannot be neglected (charged particles *orbit* when they reach the magnetic filter). It seems that the code should include the effect of the filter field explicitly. It should be possible to include its effect by following a diffusional derivation like that in Chapters 6, 7, and 9 of Golant [10].

Appendix A. *Derivation of the Moment Equations*

This appendix is based on a course handout which summarized a similar derivation in Chapter 6 of Holt and Haskell [16:152-176].

A.1 *Introduction*

By analogy to moments of force acting on a lever arm, we obtain n^{th} velocity moments of the Boltzmann equation by multiplying the Boltzmann equation by the n^{th} power of the velocity and then integrating over the velocity space. The powers of the velocity generally chosen are v^0 , mv^1 , and $\frac{1}{2}mv^2$ to correspond to the respective physically measurable quantities of number, momentum, and energy.

A.2 *Definitions*

In order to derive the velocity moments of the Boltzmann equation, we first need some basic definitions. The expectation value $\langle \phi \rangle$ of some quantity ϕ is defined as:

$$\langle \phi \rangle \equiv \frac{\int \phi \bar{n}^\alpha f^\alpha d\mathbf{v}^\alpha}{\int \bar{n}^\alpha f^\alpha d\mathbf{v}^\alpha} = \frac{1}{n^\alpha} \int \phi \bar{n}^\alpha f^\alpha d\mathbf{v}^\alpha \quad (18)$$

where \mathbf{v} is the vector velocity of species α , $f^\alpha(\mathbf{v}, \mathbf{x}, t)$ is the distribution function for a single particle of species α , $n^\alpha(\mathbf{x}, t) = \int \bar{n}^\alpha f^\alpha(\mathbf{v}, \mathbf{x}, t) d\mathbf{v}^\alpha$ is the density of particles of species α at point \mathbf{x} and time t [21:83], and $\bar{n}^\alpha = N^\alpha/\mathcal{V}$ [21:79, 316] is the average density—the ratio of the total number of particles N^α of species α to the total volume \mathcal{V} occupied by those particles. From this definition of the expectation value it follows that, if a and b are constants and g and h are functions of \mathbf{v} , then

$$\langle a \rangle = a \quad (19)$$

$$\langle ag \rangle = a \langle g \rangle \quad (20)$$

$$\langle ag + bh \rangle = \langle ag \rangle + \langle bh \rangle = a\langle g \rangle + b\langle h \rangle \quad (21)$$

The velocity v can be decomposed into two components, the mean velocity V and the peculiar velocity u , so that for each species α ,

$$v_i^\alpha = V_i^\alpha + u_i^\alpha \quad (22)$$

where i is an index defined so that $i = x, y, z$. Since the peculiar velocity is random, it averages to zero:

$$\langle u_i \rangle = 0 \quad (23)$$

Because $V(\mathbf{x}, t)$ is *not* a function of velocity v , the average velocity V can come outside of the integral in Equation 18 so that

$$\langle V_j \rangle = V_j \quad (24)$$

We can apply the results in Equations 23 and 24 to obtain the expectation value of the product $u_i V_j$:

$$\langle u_i V_j \rangle = V_j \langle u_i \rangle = 0 \quad (25)$$

Moreover, from Equations 22, 21, 23, and 24, $\langle v_i \rangle = \langle V_i + u_i \rangle = \langle V_i \rangle + \langle u_i \rangle = V_i$ so that

$$\langle v_i \rangle = V_i, \quad (26)$$

which is just the definition of the average velocity.

In order to derive the moments of the velocity distribution, we also need the relationships $\langle v_i v_j \rangle$ and $\langle v_i v_j v_k \rangle$. If we break the velocity into its components in the manner of Equation 22, the first product becomes

$$\langle v_i v_j \rangle = \langle (V_i + u_i)(V_j + u_j) \rangle = \langle (V_i V_j + u_j V_i + u_i V_j + u_i u_j) \rangle$$

Since the expectation value of a sum is just the sum of the expectation values,

$$\langle v_i v_j \rangle = \langle V_i V_j \rangle + \langle u_j V_i \rangle + \langle u_i V_j \rangle + \langle u_i u_j \rangle$$

Applying Equation 24, we obtain

$$\langle v_i v_j \rangle = V_i V_j + \underbrace{V_i \langle u_j \rangle}_{=0} + \underbrace{V_j \langle u_i \rangle}_{=0} + \langle u_i u_j \rangle$$

Recognizing that the middle two terms are zero from Equation 25, our final relation becomes

$$\langle v_i v_j \rangle = V_i V_j + \langle u_i u_j \rangle \quad (27)$$

The triple product can be analyzed in the same way. Applying Equation 22 to break the velocity into its components gives

$$\begin{aligned} \langle v_i v_j v_j \rangle &= \langle (V_i + u_i)(V_i + u_i)(V_i + u_i) \rangle = \\ &\langle V_i V_j V_j + V_i V_j u_j + V_i u_j V_j + V_i u_j u_j + u_i V_j V_j + u_i V_j u_j + u_i u_j V_j + u_i u_j u_j \rangle \end{aligned}$$

Applying Equations 21 and 24 and collecting terms yields

$$\langle v_i v_j v_j \rangle = V_i V_j V_j + 2V_i V_j \underbrace{\langle u_j \rangle}_{=0} + V_j V_j \underbrace{\langle u_i \rangle}_{=0} + 2V_j \langle u_i u_j \rangle + V_i \langle u_j u_j \rangle + \langle u_i u_j u_j \rangle$$

Equation 23 shows us that once again two of the terms are zero, so our final expression for the expectation value of the triple product is

$$\langle v_i v_j v_j \rangle = V_i V_j V_j + 2V_j \langle u_i u_j \rangle + V_i \langle u_j u_j \rangle + \langle u_i u_j u_j \rangle \quad (28)$$

A.3 The Generalized Equation of Change

If $f^\alpha(\mathbf{v}, \mathbf{x}, t)$ is the distribution function of a single particle of species α , and \bar{n}^α is the average density of particles of species α , as defined above, then $\bar{n}^\alpha f^\alpha(\mathbf{v}, \mathbf{x}, t)$ is the density distribution of particles of species α with velocities in the range \mathbf{v} to $\mathbf{v} + d\mathbf{v}$ and positions in the range \mathbf{x} to $\mathbf{x} + d\mathbf{x}$. The Boltzmann equation for particles of species α has the form:

$$\bar{n}^\alpha \left(\frac{\partial f^\alpha}{\partial t} + v_i \frac{\partial f^\alpha}{\partial x_i} + a_i \frac{\partial f^\alpha}{\partial v_i} \right) = \bar{n}^\alpha \left(\frac{\delta f^\alpha}{\delta t} \right)_{coll} \quad (29)$$

where

$$a_i = \frac{\sum F_i}{m^\alpha} = \frac{Ze}{m^\alpha} \left(E_i + \frac{1}{c} [\epsilon_{ijk} v_j^\alpha B_k] \right) = \frac{Ze}{m^\alpha} \left(\mathbf{E} + \frac{1}{c} [\mathbf{v}_\alpha \times \mathbf{B}] \right) \quad (30)$$

is the acceleration due to external forces acting on the particles, $\left(\frac{\delta f^\alpha}{\delta t} \right)_{coll}$ is the time rate of change due to collisions, Z is the charge state (defined as $Z = -1$ for electrons and $Z = +1$ for hydrogen ions), and ϵ_{ijk} is the *alternating unit tensor*, defined by [16:36]

$$\epsilon_{ijk} = \begin{cases} 1 & \text{if the indices are cyclic: } xyz, yzx, zxy. \\ -1 & \text{if the indices are anticyclic: } zyx, yxz, xzy. \\ 0 & \text{if any two or more indices are equal.} \end{cases} \quad (31)$$

Let ϕ be a generalized power of the velocity, so that we can later set $\phi = 1$, $\phi = mv$, and $\phi = \frac{1}{2}mv^2$. Multiplying the Boltzmann equation, Equation 29, by ϕ and integrating over the velocity space, we get

$$\underbrace{\int \phi \bar{n}^\alpha \frac{\partial f^\alpha}{\partial t} d\mathbf{v}^\alpha}_1 + \underbrace{\int \phi \bar{n}^\alpha v_i^\alpha \frac{\partial f^\alpha}{\partial x_i^\alpha} d\mathbf{v}^\alpha}_2 + \underbrace{\int \phi \bar{n}^\alpha a_i^\alpha \frac{\partial f^\alpha}{\partial v_i^\alpha} d\mathbf{v}^\alpha}_3 = \underbrace{\int \phi \bar{n}^\alpha \left(\frac{\delta f^\alpha}{\delta t} \right)_{coll} d\mathbf{v}^\alpha}_4 \quad (32)$$

which uses the standard shorthand notation for integration over the velocity space:

$$\int \xi d\mathbf{v} \equiv \int \int \int \xi dv_x dv_y dv_z = \int \xi dv_i \quad i = x, y, z \quad (33)$$

for some arbitrary quantity ξ .

To develop the generalized equation of change in terms of $\langle \phi \rangle$, we apply the chain rule and rearrange terms. In the case of the first term, the chain rule gives

$$\frac{\partial \bar{n}^\alpha f^\alpha \phi}{\partial t} = \bar{n}^\alpha f^\alpha \frac{\partial \phi}{\partial t} + \underbrace{\phi \bar{n}^\alpha \frac{\partial f^\alpha}{\partial t}}_1 \quad (34)$$

where the term corresponding to the first term in the integrated Boltzmann equation is indicated with an underbrace.

Solving for the term labelled "1" on the right hand side of Equation 34, we can rewrite the first term of the integrated Boltzmann equation, Equation 32, as

$$\underbrace{\int \phi \bar{n}^\alpha \frac{\partial f^\alpha}{\partial t} d\mathbf{v}^\alpha}_1 = \underbrace{\int \frac{\partial \bar{n}^\alpha f^\alpha \phi}{\partial t} d\mathbf{v}^\alpha}_{1a} - \underbrace{\int \bar{n}^\alpha f^\alpha \frac{\partial \phi}{\partial t} d\mathbf{v}^\alpha}_{1b}$$

Because we are looking at the temporal evolution of the system in terms of a phase space of $6N$ dimensions, where N is the number of particles in the system, all of the primary coordinates (x, y, z, v_x, v_y, v_z , and t) are independent from each other. This independence allows us to bring the time derivative outside of the integral in Term 1a to obtain

$$\underbrace{\int \phi \bar{n}^\alpha \frac{\partial f^\alpha}{\partial t} d\mathbf{v}^\alpha}_1 = \frac{\partial}{\partial t} \underbrace{\int \bar{n}^\alpha f^\alpha \phi d\mathbf{v}^\alpha}_{1a} - \underbrace{\int \bar{n}^\alpha f^\alpha \frac{\partial \phi}{\partial t} d\mathbf{v}^\alpha}_{1b}$$

From the definition of the expectation value ϕ in Equation 18 above, we get the relation:

$$n^\alpha \langle \phi \rangle = \int \bar{n}^\alpha f^\alpha \phi d\mathbf{v}^\alpha$$

By substituting $\frac{\partial \phi}{\partial t}$ into the above relation for ϕ , we obtain another relation:

$$n^\alpha \langle \frac{\partial \phi}{\partial t} \rangle = \int \bar{n}^\alpha f^\alpha \frac{\partial \phi}{\partial t} d\mathbf{v}^\alpha$$

Applying these two relations to the expression for the first term of the integrated Boltzmann equation gives

$$\underbrace{\int \phi \bar{n}^\alpha \frac{\partial f^\alpha}{\partial t} d\mathbf{v}^\alpha}_1 = \underbrace{\frac{\partial}{\partial t} (n^\alpha \langle \phi \rangle)}_{1a} - \underbrace{n^\alpha \langle \frac{\partial \phi}{\partial t} \rangle}_{1b} \quad (35)$$

where the integrals really haven't been solved, but have merely been hidden by the bracket notation for expectation values.

The second term of the integrated Boltzmann equation lends itself to similar analysis. In this case the chain rule gives

$$\frac{\partial}{\partial x_i^\alpha} (\bar{n}^\alpha f^\alpha \phi) = \bar{n}^\alpha f^\alpha \frac{\partial \phi}{\partial x_i^\alpha} + \underbrace{\phi \frac{\partial}{\partial x_i^\alpha} (\bar{n}^\alpha f^\alpha)}_2 \quad (36)$$

Solving for the term marked "2" and using the resulting expression to expand the second term of the integrated Boltzmann equation gives

$$\underbrace{\int \phi \bar{n}^\alpha v_i^\alpha \frac{\partial f^\alpha}{\partial x_i^\alpha} d\mathbf{v}^\alpha}_2 = \underbrace{\int v_i^\alpha \phi \frac{\partial}{\partial x_i^\alpha} (\bar{n}^\alpha f^\alpha) d\mathbf{v}^\alpha}_2 = \underbrace{\int v_i^\alpha \frac{\partial}{\partial x_i^\alpha} (\bar{n}^\alpha f^\alpha \phi) d\mathbf{v}^\alpha}_{2a} - \underbrace{\int v_i^\alpha \bar{n}^\alpha f^\alpha \frac{\partial \phi}{\partial x_i^\alpha} d\mathbf{v}^\alpha}_{2b}$$

Once again we can apply the independence of the v_i and x_i coordinates to bring the partial differentiation outside the integral in Term 2a:

$$\underbrace{\int \phi \bar{n}^\alpha v_i^\alpha \frac{\partial f^\alpha}{\partial x_i^\alpha} d\mathbf{v}^\alpha}_2 = \underbrace{\frac{\partial}{\partial x_i^\alpha} \int v_i^\alpha (\bar{n}^\alpha f^\alpha \phi) d\mathbf{v}^\alpha}_{2a} - \underbrace{\int v_i^\alpha \bar{n}^\alpha f^\alpha \frac{\partial \phi}{\partial x_i^\alpha} d\mathbf{v}^\alpha}_{2b}$$

Substituting into the definition of the expectation value in Equation 18 gives a relation for $\langle v_i^\alpha \phi \rangle$

$$n^\alpha \langle v_i^\alpha \phi \rangle = \underbrace{\int v_i^\alpha (\bar{n}^\alpha f^\alpha \phi) d\mathbf{v}^\alpha}_{2a}$$

and another for $\langle v_i^\alpha \frac{\partial \phi}{\partial x_i^\alpha} \rangle$

$$n^\alpha \langle v_i^\alpha \frac{\partial \phi}{\partial x_i^\alpha} \rangle = \underbrace{\int v_i^\alpha \bar{n}^\alpha f^\alpha \frac{\partial \phi}{\partial x_i^\alpha} d\mathbf{v}^\alpha}_{2b}$$

We can rewrite the second term of the Boltzmann equation in terms of these two relations to get the final form of that term:

$$\underbrace{\int \phi \bar{n}^\alpha v_i^\alpha \frac{\partial f^\alpha}{\partial x_i^\alpha} d\mathbf{v}^\alpha}_2 = \underbrace{\frac{\partial \phi}{\partial x_i^\alpha} n^\alpha \langle v_i^\alpha \phi \rangle}_{2a} - \underbrace{n^\alpha \langle v_i^\alpha \frac{\partial \phi}{\partial x_i^\alpha} \rangle}_{2b} \quad (37)$$

where Term 2a is analogous to Term 1a, and Term 2b to Term 1b.

To derive a term like the third term in the integrated Boltzmann equation, Equation 32, we can apply the chain rule to the following expression:

$$\frac{\partial}{\partial v_i^\alpha} (\phi \bar{n}^\alpha a_i^\alpha f^\alpha) = \bar{n}^\alpha a_i^\alpha f^\alpha \frac{\partial \phi}{\partial v_i^\alpha} + \phi \bar{n}^\alpha f^\alpha \frac{\partial a_i^\alpha}{\partial v_i^\alpha} + \underbrace{\phi \bar{n}^\alpha a_i^\alpha \frac{\partial f^\alpha}{\partial v_i^\alpha}}_3 \quad (38)$$

Solving for the term labelled "3" in Equation 38 and using the resulting expression to expand the third term of the integrated Boltzmann equation gives

$$\underbrace{\int \phi \bar{n}^\alpha a_i^\alpha \frac{\partial f^\alpha}{\partial v_i^\alpha} dv^\alpha}_3 = \underbrace{\int \frac{\partial}{\partial v_i^\alpha} (\phi \bar{n}^\alpha a_i^\alpha f^\alpha) dv^\alpha}_{3a} + \underbrace{\int \bar{n}^\alpha a_i^\alpha f^\alpha \frac{\partial \phi}{\partial v_i^\alpha} dv^\alpha}_{3b} + \underbrace{\int \phi \bar{n}^\alpha f^\alpha \frac{\partial a_i^\alpha}{\partial v_i^\alpha} dv^\alpha}_{3c} \quad (39)$$

Looking at Term 3a, we see that

$$\begin{aligned} \int \frac{\partial}{\partial v_i^\alpha} (a_i^\alpha \phi \bar{n}^\alpha f^\alpha) dv_i &= \\ \int \frac{\partial}{\partial v_x^\alpha} (a_x^\alpha \phi \bar{n}^\alpha f^\alpha) dv_x + \int \frac{\partial}{\partial v_y^\alpha} (a_y^\alpha \phi \bar{n}^\alpha f^\alpha) dv_y + \int \frac{\partial}{\partial v_z^\alpha} (a_z^\alpha \phi \bar{n}^\alpha f^\alpha) dv_z &= \\ a_i^\alpha \phi \bar{n}^\alpha f^\alpha \Big|_{-\infty}^{+\infty} \end{aligned}$$

Because, as v_i goes to infinity, the distribution function f^α goes to zero more strongly than $\phi = 1$, $\phi = mv$, or $\phi = \frac{1}{2}mv^2$ go to infinity, the value of term 3a is zero.

Likewise, we can see that the value of term 3c is zero by evaluating the partial derivative $\frac{\partial a_i^\alpha}{\partial v_i^\alpha}$. Equation 30 gives a value for the acceleration which we can substitute into the derivative to separate it into electric-field and magnetic-field components:

$$\begin{aligned} \frac{\partial a_i^\alpha}{\partial v_i^\alpha} &= \frac{\partial}{\partial v_i^\alpha} \left\{ \frac{Ze}{m^\alpha} \left(E_i + \frac{1}{c} [\epsilon_{ijk} v_j^\alpha B_k] \right) \right\} \\ &= \underbrace{\frac{Ze}{m^\alpha} \frac{\partial E_i}{\partial v_i^\alpha}}_{\text{E-field component}} + \underbrace{\frac{Ze}{m^\alpha c} \frac{\partial}{\partial v_i^\alpha} [\epsilon_{ijk} v_j^\alpha B_k]}_{\text{B-field component}} \end{aligned}$$

First, consider the electric-field component. Since E_i is not a function of v_i ,

$$\frac{\partial E_i}{\partial v_i^\alpha} = 0$$

so the value of the electric-field component is zero.

Next, consider the magnetic-field component. Since neither B_k nor ϵ_{ijk} are functions of v_i ,

$$\frac{\partial}{\partial v_i^\alpha} [\epsilon_{ijk} v_j^\alpha B_k] = [\epsilon_{ijk} \frac{\partial v_j^\alpha}{\partial v_i^\alpha} B_k]$$

Looking at the partial term on the right, we see that

$$\frac{\partial v_j^\alpha}{\partial v_i^\alpha} = \begin{cases} 1 & i = j \\ 0 & i \neq j \end{cases}$$

and there is no contribution when $i \neq j$. But from the definition of the alternating unit tensor ϵ_{ijk} in Equation 31, when $i = j$, then $\epsilon_{ijk} = \epsilon_{jjk} = 0$. So when $i = j$, the magnetic-field component is zero because $\epsilon_{ijk} = 0$, and when $i \neq j$, the magnetic field component is zero because $\frac{\partial v_j^\alpha}{\partial v_i^\alpha} = 0$. Therefore, both the components of Term 3c are zero, so the value of Term 3c is also zero.

Only Term 3b remains in the third term of the integrated Boltzmann equation. The definition of the expectation value allows us to rewrite this term more compactly:

$$n^\alpha \langle a_i^\alpha \frac{\partial \phi}{\partial v_i^\alpha} \rangle = \underbrace{\int \bar{n}^\alpha a_i^\alpha f^\alpha \frac{\partial \phi}{\partial v_i^\alpha} d\mathbf{v}^\alpha}_{3b}$$

Substituting the values derived for Terms 3a, 3b, and 3c back into Equation 39 gives the final expression for the third term of the integrated Boltzmann equation:

$$\underbrace{\frac{\partial}{\partial v_i^\alpha} (\phi \bar{n}^\alpha a_i^\alpha f^\alpha)}_3 = n^\alpha \underbrace{\langle a_i^\alpha \frac{\partial \phi}{\partial v_i^\alpha} \rangle}_{3b} \quad (40)$$

where Term 3b is of the same form as Terms 1b and 2b.

Substituting the expressions in Equations 35, 37, and 40 into Equation 32, the integrated Boltzmann equation becomes:

$$\underbrace{\frac{\partial}{\partial t}(n^\alpha \langle \phi \rangle)}_{1a} - \underbrace{n^\alpha \langle \frac{\partial \phi}{\partial t} \rangle}_{1b} + \underbrace{\frac{\partial}{\partial x_i^\alpha} n^\alpha \langle v_i^\alpha \phi \rangle}_{2a} - \underbrace{n^\alpha \langle v_i^\alpha \frac{\partial \phi}{\partial x_i^\alpha} \rangle}_{2b} + \underbrace{n^\alpha \langle a_i^\alpha \frac{\partial \phi}{\partial v_i^\alpha} \rangle}_{3b} = \underbrace{\int \phi \bar{n}^\alpha \frac{\delta f^\alpha}{\delta t} \bigg|_{coll} d\mathbf{v}^\alpha}_{4} \quad (41)$$

If we collect together the "a" terms and the "b" terms in Equation 41, we get what is known as the *generalized equation of change*:

$$\underbrace{\frac{\partial}{\partial t}(n^\alpha \langle \phi \rangle)}_1 + \underbrace{\frac{\partial}{\partial x_i^\alpha} (n^\alpha \langle v_i^\alpha \phi \rangle)}_2 - n^\alpha \left(\underbrace{\langle \frac{\partial \phi}{\partial t} \rangle}_3 + \underbrace{\langle v_i^\alpha \frac{\partial \phi}{\partial x_i^\alpha} \rangle}_4 + \underbrace{\langle a_i^\alpha \frac{\partial \phi}{\partial v_i^\alpha} \rangle}_5 \right) = \underbrace{\int \phi \bar{n}^\alpha \frac{\delta f^\alpha}{\delta t} \bigg|_{coll} d\mathbf{v}^\alpha}_6 \quad (42)$$

where the overbraces identify the terms of the integrated Boltzmann equation, and the underbraces identify the terms of the generalized equation of change.

Holt and Haskell [16:154-155] identify the physical significance of the terms of the generalized equation of change: Term 1 is the "local time variation of the mean value" of ϕ [16:154]. Term 2 represents the part of that local time variation caused by "molecules streaming in and out of the volume element" [16:154]. Terms 3, 4, and 5 represent the part of the local time variation due to the dependence of ϕ on "the time, the position of the particles, and the external forces" [16:155], respectively. Finally, Term 6 represents the part of the local time variation caused by collisions with particles of other species. Any gain in the mean value of ϕ must be reflected in a corresponding and equal loss from the other species.

A.4 The Zeroth Velocity Moment (The Continuity Equation)

To develop an equation for number, we let $\phi = 1$ in the generalized equation of change. Then $\frac{\partial \phi}{\partial t} = 0$, $\frac{\partial \phi}{\partial x_i^\alpha} = 0$, $\frac{\partial \phi}{\partial v_i^\alpha} = 0$, and $\langle \phi \rangle = 1$ so that the generalized equation of change reduces to

$$\underbrace{\frac{\partial}{\partial t}(n^\alpha)}_1 + \underbrace{\frac{\partial}{\partial x_i^\alpha}(n^\alpha \langle v_i^\alpha \rangle)}_2 = \underbrace{\int \bar{n}^\alpha \frac{\delta f^\alpha}{\delta t} dv^\alpha}_{6 \text{ coll}} \quad (43)$$

It is customary to define the term S_{coll}^α so that

$$\int \bar{n}^\alpha \frac{\delta f^\alpha}{\delta t} dv^\alpha \equiv S_{coll}^\alpha = (Production) - (Loss) \quad (44)$$

where the term *production* refers to production of charge carriers, or ionization, and the term *loss* refers to the loss of charge carriers, or recombination. If we substitute S_{coll}^α from Equation 44, and recognize that Equation 26 shows that $\langle v_i^\alpha \rangle = V_i^\alpha$, then Equation 43 becomes

$$\frac{\partial}{\partial t}(n^\alpha) + \frac{\partial}{\partial x_i^\alpha}(n^\alpha V_i^\alpha) = S_{coll}^\alpha \quad (45)$$

This equation expresses the principle of conservation of number of charged particles and is therefore called the *continuity equation*. Equation 45 is the same form used in Equation 1.11 of Braginskii's derivation [3:208], except that Braginskii assumes that no particles are created or destroyed in collisions so that on the right hand side, $S_{coll}^\alpha = 0$.

Applying the chain rule to the second term on the left side of Equation 45 gives

$$\frac{\partial(n^\alpha V_i^\alpha)}{\partial x_i^\alpha} = V_i^\alpha \frac{\partial n^\alpha}{\partial x_i^\alpha} + n^\alpha \frac{\partial V_i^\alpha}{\partial x_i^\alpha}$$

Rewriting the continuity equation, Equation 45, with the second term expanded by means of this expression gives:

$$\frac{\partial n^\alpha}{\partial t} + \left(V_i^\alpha \frac{\partial n^\alpha}{\partial x_i^\alpha} + n^\alpha \frac{\partial V_i^\alpha}{\partial x_i^\alpha} \right) = S_{coll}^\alpha$$

We can now regroup the terms thus:

$$\left(\frac{\partial}{\partial t} + V_i^\alpha \frac{\partial}{\partial x_i^\alpha} \right) n^\alpha + n^\alpha \frac{\partial V_i^\alpha}{\partial x_i^\alpha} = S_{coll}^\alpha$$

to get another form of the continuity equation:

$$\frac{d}{dt} n^\alpha + n^\alpha \frac{\partial V_i^\alpha}{\partial x_i^\alpha} = S_{coll}^\alpha \quad (46)$$

where

$$\frac{d}{dt} \equiv \frac{\partial}{\partial t} + V_i^\alpha \frac{\partial}{\partial x_i^\alpha} \quad (47)$$

is the definition of the *convective derivative*, $\frac{d}{dt}$.

A.5 The First Velocity Moment (The Momentum Equation)

To obtain an equation for the momentum balance, we set $\phi = m^\alpha v_j^\alpha$ and substitute into Equation 42, the generalized equation of change, to obtain:

$$\begin{aligned} \underbrace{\frac{\partial n^\alpha \langle (m^\alpha v_j^\alpha) \rangle}{\partial t}}_1 + \underbrace{\frac{\partial n^\alpha \langle v_i^\alpha (m^\alpha v_j^\alpha) \rangle}{\partial x_i^\alpha}}_2 &= n^\alpha \left(\underbrace{\left\langle \frac{\partial (m^\alpha v_j^\alpha)}{\partial t} \right\rangle}_3 + \underbrace{\left\langle v_i^\alpha \frac{\partial (m^\alpha v_j^\alpha)}{\partial x_i^\alpha} \right\rangle}_4 + \underbrace{\left\langle a_i^\alpha \frac{\partial (m^\alpha v_j^\alpha)}{\partial v_i^\alpha} \right\rangle}_5 \right) \\ &= \underbrace{\int (m^\alpha v_j^\alpha) \bar{n} \frac{\delta f^\alpha}{\delta t}}_{6, coll} d\mathbf{v}^\alpha \end{aligned}$$

Since $\langle \phi \rangle = m^\alpha \langle v_j^\alpha \rangle = m^\alpha V_j^\alpha$ by Equation 26, we can transform the first term of the generalized equation of change:

$$\underbrace{\frac{\partial}{\partial t}(n^\alpha \langle m^\alpha v_j^\alpha \rangle)}_1 = \underbrace{\frac{\partial}{\partial t}(n^\alpha m^\alpha V_j^\alpha)}_{1'}$$

From Equation 20 and Equation 27 we can see that

$$\langle v_i^\alpha \phi \rangle = \langle v_i^\alpha (m^\alpha v_j^\alpha) \rangle = m^\alpha \langle v_i^\alpha v_j^\alpha \rangle = m^\alpha V_i^\alpha V_j^\alpha + m^\alpha \langle u_i^\alpha u_j^\alpha \rangle$$

so we can expand the second term of the generalized equation of change:

$$\underbrace{\frac{\partial}{\partial x_i^\alpha}(n^\alpha \langle v_i^\alpha (m^\alpha v_j^\alpha) \rangle)}_2 = \underbrace{\frac{\partial}{\partial x_i^\alpha}(n^\alpha m^\alpha V_i^\alpha V_j^\alpha)}_{2a'} + \underbrace{\frac{\partial}{\partial x_i^\alpha}(n^\alpha m^\alpha \langle u_i^\alpha u_j^\alpha \rangle)}_{2b'}$$

Since the velocity space, configuration space, and time coordinates are independent, the time and configuration space derivatives of ϕ are zero:

$$\frac{\partial \phi}{\partial t} = m^\alpha \frac{\partial v_j^\alpha}{\partial t} = 0 \qquad \frac{\partial \phi}{\partial x_i^\alpha} = m^\alpha \frac{\partial v_j^\alpha}{\partial x_i^\alpha} = 0$$

This means that the third and fourth terms of the generalized equation of change are also zero:

$$\underbrace{n^\alpha m^\alpha \left\langle \frac{\partial v_j^\alpha}{\partial t} \right\rangle}_3 = 0 \qquad \underbrace{n^\alpha m^\alpha \left\langle v_i^\alpha \frac{\partial v_j^\alpha}{\partial t} \right\rangle}_4 = 0$$

If we use the *Kronecker delta* δ_{ij} with the property that

$$\delta_{ij} = \begin{cases} 1 & i = j \\ 0 & i \neq j \end{cases}$$

we can express the partial derivative of ϕ with respect to the velocity as

$$\frac{\partial \phi}{\partial v_i^\alpha} = m^\alpha \frac{\partial v_j^\alpha}{\partial v_i^\alpha} = m^\alpha \delta_{ij}$$

because the partial derivative is equal to one when the indices are the same ($i = j$) and zero otherwise. Applying this notation to the fifth term of the generalized equation of change gives

$$\underbrace{n^\alpha \langle a_i^\alpha \frac{\partial(m^\alpha v_j^\alpha)}{\partial v_i^\alpha} \rangle}_5 = n^\alpha \langle a_i^\alpha m^\alpha \delta_{ij} \rangle = \underbrace{n^\alpha \langle a_i^\alpha m^\alpha \rangle}_{5'}$$

Finally, let A_j^α , the momentum exchanged in the j^{th} direction due to collisions, be defined as

$$\underbrace{A_j^\alpha}_{6'} \equiv m^\alpha v_j^\alpha S_{coll}^\alpha = \underbrace{\int m^\alpha v_j^\alpha \bar{n}^\alpha \frac{\delta f^\alpha}{\delta t}}_{6} \Big|_{coll} d\mathbf{v}^\alpha \quad (48)$$

Collecting the primed terms, we obtain a form of the equation for momentum balance:

$$\underbrace{\frac{\partial}{\partial t} (n^\alpha m^\alpha V_j^\alpha)}_1 + \underbrace{\frac{\partial}{\partial x_i^\alpha} (n^\alpha m^\alpha V_i^\alpha V_j^\alpha)}_2 + \underbrace{\frac{\partial}{\partial x_i^\alpha} (n^\alpha m^\alpha \langle u_i^\alpha u_j^\alpha \rangle)}_3 + \underbrace{n^\alpha \langle a_i^\alpha m^\alpha \delta_{ij} \rangle}_4 = \underbrace{A_j^\alpha}_{5'} \quad (49)$$

where the overbraces indicate terms of the generalized equation of change, Equation 42, and the underbraces indicate terms of this form of the momentum balance equation.

Each of the terms of the momentum balance equation, Equation 49, has a physical interpretation [6:80-82]. Term 1 is the time rate of change of the momentum density. Term 2 is the gradient of the macroscopic momentum flow (momentum density times velocity). Term 3 is the gradient of the "hidden" (microscopic) momentum flow, due to the random thermal motion of molecules. Term 4 is the change in momentum caused by external forces. Term 5 is the change in momentum

of particles of species α due to collisions with particles of other species. Any gain or loss through this term will appear in the momentum balance equation of another species.

It is possible to rewrite the first two terms of Equation 49 in terms of the continuity equation, Equation 46. Using the chain rule to expand each term gives

$$\underbrace{\frac{\partial}{\partial t}(n^\alpha m^\alpha V_j^\alpha)}_1 + \underbrace{\frac{\partial}{\partial x_i^\alpha}(n^\alpha m^\alpha V_i^\alpha V_j^\alpha)}_2 = \left(\underbrace{n^\alpha m^\alpha \frac{\partial V_j^\alpha}{\partial t}}_{1a} + \underbrace{m^\alpha V_j^\alpha \frac{\partial n^\alpha}{\partial t}}_{1b} \right) + \left(\underbrace{n^\alpha m^\alpha V_i^\alpha \frac{\partial V_j^\alpha}{\partial x_i^\alpha}}_{2a} + \underbrace{m^\alpha V_j^\alpha \frac{\partial n^\alpha V_i^\alpha}{\partial x_i^\alpha}}_{2b} \right)$$

Regrouping the terms on the right side of the equation gives

$$\underbrace{\frac{\partial}{\partial t}(n^\alpha m^\alpha V_j^\alpha)}_1 + \underbrace{\frac{\partial}{\partial x_i^\alpha}(n^\alpha m^\alpha V_i^\alpha V_j^\alpha)}_2 = n^\alpha m^\alpha \left(\underbrace{\frac{\partial V_j^\alpha}{\partial t}}_{1a} + \underbrace{V_i^\alpha \frac{\partial V_j^\alpha}{\partial x_i^\alpha}}_{2a} \right) + m^\alpha V_j^\alpha \left(\underbrace{\frac{\partial n^\alpha}{\partial t}}_{1b} + \underbrace{\frac{\partial n^\alpha V_i^\alpha}{\partial x_i^\alpha}}_{2b} \right)$$

(Continuity Equation)

where the quantity multiplying $m^\alpha V_j^\alpha$ on the right hand side is the left hand side of the continuity equation, Equation 45. If we substitute from the continuity equation, the first two terms of the momentum balance equation transform to:

$$\underbrace{\frac{\partial}{\partial t}(n^\alpha m^\alpha V_j^\alpha)}_1 + \underbrace{\frac{\partial}{\partial x_i^\alpha}(n^\alpha m^\alpha V_i^\alpha V_j^\alpha)}_2 = \underbrace{n^\alpha m^\alpha \frac{d}{dt} V_j^\alpha}_{1a \& 2a} + \underbrace{m^\alpha V_j^\alpha S_{coll}^\alpha}_{1b \& 2b}$$

where the convective derivative $\frac{d}{dt}$ is defined as in Equation 47.

To derive an expression for Term 3 in Equation 49, we need to look more closely at the kinetic energy and its relationship to pressure. The expectation value of the kinetic energy density of particles of species α and velocity v_i^α may be expanded using Equation 20 and Equation 27 to obtain:

$$\langle n^\alpha \frac{1}{2} m^\alpha v_i^\alpha v_i^\alpha \rangle = n^\alpha \frac{1}{2} m^\alpha \langle v_i^\alpha v_i^\alpha \rangle = n^\alpha \frac{1}{2} m^\alpha V_i^\alpha V_i^\alpha + n^\alpha \frac{1}{2} m^\alpha \langle u_i^\alpha u_i^\alpha \rangle$$

The first term in this expansion may be identified as the *macroscopic* kinetic energy, and the second term as the *microscopic* or *thermal* kinetic energy.

From the definition of the expectation value in Equation 18, we can write the thermal kinetic energy density as:

$$n^\alpha \frac{1}{2} m^\alpha \langle u_i^\alpha u_i^\alpha \rangle = n^\alpha \frac{1}{2} m^\alpha \frac{\int u_i^\alpha u_i^\alpha \bar{n}^\alpha f^\alpha d\mathbf{v}^\alpha}{\int \bar{n}^\alpha f^\alpha d\mathbf{v}^\alpha}$$

Suppose that $f^\alpha(u_j^\alpha)$ is approximately a Maxwellian distribution [29:492] [21:5], so

$$f^\alpha(u_j^\alpha) = A \exp \left\{ -\frac{m u_j^\alpha u_j^\alpha}{2T^\alpha} \right\}$$

where $A = \left(\frac{m}{2\pi T^\alpha} \right)^{3/2}$ is the normalization constant for the distribution. Substituting this Maxwellian distribution into the expression for the thermal kinetic energy gives:

$$n^\alpha \frac{1}{2} m^\alpha \langle u_i^\alpha u_i^\alpha \rangle = n^\alpha \frac{1}{2} m^\alpha \frac{\int u_i^\alpha u_i^\alpha \bar{n}^\alpha A \exp \left\{ -\frac{m u_i^\alpha u_i^\alpha}{2T^\alpha} \right\} d\mathbf{v}^\alpha}{\int \bar{n}^\alpha A \exp \left\{ -\frac{m u_i^\alpha u_i^\alpha}{2T^\alpha} \right\} d\mathbf{v}^\alpha}$$

Multiplying the numerator by $1 = \frac{T^\alpha}{T^\alpha}$ and rearranging terms enables us to form the argument of the exponent inside the integral and bring the constants $\bar{n}^\alpha A$ outside the integral, where they cancel:

$$n^\alpha \frac{1}{2} m^\alpha \langle u_i^\alpha u_i^\alpha \rangle = n^\alpha T^\alpha \underbrace{\frac{\bar{n}^\alpha A}{\bar{n}^\alpha A}}_{=1} \frac{\int \frac{m^\alpha u_i^\alpha u_i^\alpha}{2T^\alpha} \exp \left\{ -\frac{m u_i^\alpha u_i^\alpha}{2T^\alpha} \right\} d\mathbf{v}^\alpha}{\int \exp \left\{ -\frac{m u_i^\alpha u_i^\alpha}{2T^\alpha} \right\} d\mathbf{v}^\alpha}$$

The change of variables $\xi = \frac{m^\alpha u_i^\alpha u_i^\alpha}{2T^\alpha}$ implies

$$d\xi = \frac{m^\alpha u_i^\alpha}{T^\alpha} du_i^\alpha = \sqrt{\frac{2m^\alpha}{T^\alpha}} \sqrt{\frac{m^\alpha u_i^\alpha u_i^\alpha}{2T^\alpha}} du_i^\alpha = \sqrt{\frac{2m^\alpha}{T^\alpha}} \sqrt{\xi} du_i^\alpha$$

This expression for $d\xi$ may be solved for du_i^α to give

$$du_i^\alpha = \sqrt{\frac{T^\alpha}{2m^\alpha}} \frac{1}{\sqrt{\xi}} d\xi$$

Since V_i^α is a constant, Equation 33 and Equation 22 show that

$$d\mathbf{v}^\alpha = dv_i^\alpha = d(V_i^\alpha + u_i^\alpha) = \underbrace{dV_i^\alpha}_{=0} + du_i^\alpha = du_i^\alpha$$

so we can write

$$d\mathbf{v}_i^\alpha = \sqrt{\frac{T^\alpha}{2m^\alpha}} (\xi)^{(-1/2)} d\xi$$

Upon making the substitution of variables into the integral, the remaining constant term $\sqrt{\frac{T^\alpha}{2m^\alpha}}$ can come outside the integral, so the expression for the thermal kinetic energy density becomes:

$$n^\alpha \frac{1}{2} m^\alpha \langle u_i^\alpha u_i^\alpha \rangle = 3n^\alpha T^\alpha \underbrace{\frac{\sqrt{\frac{T^\alpha}{2m^\alpha}}}{\sqrt{\frac{T^\alpha}{2m^\alpha}}}}_{=1} \frac{\int (\xi)^{1/2} \exp \{-\xi\} d\mathbf{v}^\alpha}{\int (\xi)^{-1/2} \exp \{-\xi\} d\mathbf{v}^\alpha}$$

where the factor of 3 comes from summing over the index $i = x, y, z$. The gamma function $\Gamma(\zeta)$ is defined by

$$\Gamma(\zeta) \equiv \int_0^\infty t^{(\zeta-1)} e^{-t} dt \quad \zeta > 0$$

and has the property that

$$\Gamma(\zeta + 1) = \zeta \Gamma(\zeta)$$

Recognizing the gamma functions in the numerator and the denominator, we can transform the expression for the microscopic kinetic energy density to:

$$n^\alpha \frac{1}{2} m^\alpha \langle u_i^\alpha u_i^\alpha \rangle = 3n^\alpha T^\alpha \frac{\Gamma(\frac{3}{2})}{\Gamma(\frac{1}{2})} = 3n^\alpha T^\alpha \frac{\frac{1}{2}\Gamma(\frac{1}{2})}{\Gamma(\frac{1}{2})} = \frac{3}{2} n^\alpha T^\alpha = \frac{3}{2} p^\alpha$$

which demonstrates the basic relationship

$$n^\alpha \frac{1}{2} m^\alpha \langle u_i^\alpha u_i^\alpha \rangle = \frac{3}{2} n^\alpha T^\alpha = \frac{3}{2} p^\alpha \quad (50)$$

between the thermal kinetic energy density and the scalar pressure. Define the quantity ψ_{ij}^α as in Equation 1.19 in Braginskii [3:210] so that

$$\psi_{ij}^\alpha \equiv n^\alpha m^\alpha \langle u_i^\alpha u_j^\alpha \rangle \quad (51)$$

Then the quantity ψ_{ij}^α is a second-order tensor known as the *pressure tensor*¹. Suppose that ψ_{ij}^α is spherically symmetric, i.e., $i = j$. Then

$$\psi_{kk}^\alpha = n^\alpha m^\alpha \langle u_k^\alpha u_k^\alpha \rangle = 3n^\alpha T^\alpha = 3p^\alpha$$

as demonstrated above. The spherically symmetric part of the pressure tensor comprises its diagonal elements so that

$$\psi_{kk}^\alpha = \begin{bmatrix} p_x^\alpha & 0 & 0 \\ 0 & p_y^\alpha & 0 \\ 0 & 0 & p_z^\alpha \end{bmatrix}$$

where p_i^α is the pressure in the i^{th} direction. In an isotropic medium, $p_x^\alpha = p_y^\alpha = p_z^\alpha = p^\alpha$ where p^α is the scalar pressure. The trace of ψ_{kk}^α is thus

$$p_x^\alpha + p_y^\alpha + p_z^\alpha = 3p^\alpha$$

so that the symmetric part of the pressure tensor can be expressed as

$$p^\alpha \delta_{ij} = \frac{1}{3} n^\alpha m^\alpha \langle u_k^\alpha u_k^\alpha \rangle \delta_{ij}$$

If the pressure tensor is not spherically symmetric, as in the case where a magnetic field is present, it contains off-diagonal terms and thus may be written as the sum of its diagonal and

¹The symbol ψ was *not* chosen to represent the pressure tensor because of the abbreviation p.s.i., although the coincidence is interesting.

off-diagonal elements:

$$\psi_{ij}^\alpha = p^\alpha \delta_{ij} + \Pi_{ij}^\alpha$$

where Π_{ij}^α is the *viscosity stress tensor*, defined by:

$$\Pi_{ij}^\alpha = \psi_{ij}^\alpha - p^\alpha \delta_{ij} = n^\alpha m^\alpha \langle u_i^\alpha u_j^\alpha \rangle - \frac{1}{3} n^\alpha m^\alpha \langle u_k^\alpha u_k^\alpha \rangle \delta_{ij}$$

Thus Term 3 of Equation 49 can be separated into two components, one corresponding to the scalar pressure, the other to the stress tensor:

$$\underbrace{\frac{\partial}{\partial x_i^\alpha} (n^\alpha m^\alpha \langle u_i^\alpha u_j^\alpha \rangle)}_3 = \frac{\partial \psi_{ij}^\alpha}{\partial x_i^\alpha} = \frac{\partial p^\alpha \delta_{ij}}{\partial x_i^\alpha} + \frac{\partial \Pi_{ij}^\alpha}{\partial x_i^\alpha}$$

Equation 30 gives an expression for the acceleration that we can substitute into Term 4 of Equation 49:

$$\underbrace{n^\alpha \langle a_i^\alpha m^\alpha \delta_{ij} \rangle}_4 = n^\alpha \langle \frac{\sum F_i}{m^\alpha} m^\alpha \delta_{ij} \rangle = Zen^\alpha \langle \left(E_i + \frac{1}{c} [\epsilon_{ijk} v_j^\alpha B_k] \right) \delta_{ij} \rangle$$

Because ϵ_{ijk} and B_k are independent of v_i , we can bring them outside of the expectation value, so applying Equation 22 to break the velocity into its components gives:

$$\underbrace{n^\alpha \langle a_i^\alpha m^\alpha \delta_{ij} \rangle}_4 = Zen^\alpha \left(\langle E_i \rangle + \frac{1}{c} [\epsilon_{ijk} \langle V_j^\alpha \rangle B_k] + \frac{1}{c} [\epsilon_{ijk} \langle u_j^\alpha \rangle B_k] \right) \delta_{ij}$$

Since $\langle u_j \rangle = 0$ from Equation 23, $\langle V_j \rangle = V_j$ from Equation 24, and $\langle E_i \rangle = E_i$ because E_i is independent of v_i , the final version of Term 4 is

$$\underbrace{n^\alpha \langle a_i^\alpha m^\alpha \delta_{ij} \rangle}_4 = Zen^\alpha \left(E_i + \frac{1}{c} [\epsilon_{ijk} V_j^\alpha B_k] \right) \delta_{ij}$$

We can use Equation 22 to expand Term 5, A_j^α , into its components:

$$\begin{aligned} \underbrace{A_j^\alpha}_5 &= \int (m^\alpha u_j^\alpha) \bar{n}^\alpha \frac{\delta f^\alpha}{\delta t} \Big|_{coll} d\mathbf{v}^\alpha = \int m^\alpha (u_j^\alpha + V_j^\alpha) \bar{n}^\alpha \frac{\delta f^\alpha}{\delta t} \Big|_{coll} d\mathbf{v}^\alpha \\ &= \int m^\alpha u_j^\alpha \bar{n}^\alpha \frac{\delta f^\alpha}{\delta t} \Big|_{coll} d\mathbf{v}^\alpha + m^\alpha V_j^\alpha \int \bar{n}^\alpha \frac{\delta f^\alpha}{\delta t} \Big|_{coll} d\mathbf{v}^\alpha = \underbrace{R_j^\alpha}_{5a} + \underbrace{m^\alpha V_j^\alpha S_{coll}^\alpha}_{5b} \end{aligned}$$

where Equation 44 defines the net production, S_{coll}^α , and

$$R_j^\alpha \equiv \int \bar{n}^\alpha m^\alpha u_j^\alpha \frac{\delta f^\alpha}{\delta t} \Big|_{coll} d\mathbf{v}^\alpha \quad (52)$$

defines R_j^α , the net microscopic momentum exchanged in the j^{th} direction through collisions with species α .

Collecting the derived forms of Terms 1 through 5 gives the equation:

$$\underbrace{n^\alpha m^\alpha \frac{d}{dt} V_j^\alpha}_{1a \& 2a} + \underbrace{m^\alpha V_j^\alpha S_{coll}^\alpha}_{1b \& 2b} - \underbrace{\frac{\partial p \delta_{ij}}{\partial x_i^\alpha} - \frac{\partial \Pi_{ij}}{\partial x_i^\alpha}}_3 + \underbrace{Z e n^\alpha \left(E_i + \frac{1}{c} [\epsilon_{ijk} V_j^\alpha B_k] \right) \delta_{ij}}_4 = \underbrace{R_j^\alpha}_{5a} + \underbrace{m^\alpha V_j^\alpha S_{coll}^\alpha}_{5b}$$

If we cancel the terms $m^\alpha V_j^\alpha S_{coll}^\alpha$ that appear on both sides of the equation, we obtain the *momentum balance equation*, Equation 1.14 in Braginskii [3:209]:

$$\underbrace{n^\alpha m^\alpha \frac{dV_j^\alpha}{dt}}_{1 \& 2} - \underbrace{\frac{\partial p \delta_{ij}}{\partial x_i^\alpha}}_3 - \underbrace{\frac{\partial \Pi_{ij}}{\partial x_i^\alpha}}_4 + \underbrace{Z e n^\alpha \left(E_i + \frac{1}{c} [\epsilon_{ijk} V_j^\alpha B_k] \right) \delta_{ij}}_5 = \underbrace{R_j^\alpha}_{5, 7, 8, \& 9} \quad (53)$$

where the overbraces indicate the terms of the original form of the momentum balance equation, Equation 49, and the underbraces indicate the terms of the momentum balance equation as implemented in the model, Equation 9.

A.6 The Second Velocity Moment (The Energy Equation)

To get an equation for the energy balance, we begin with the generalized equation of change, Equation 42:

$$\underbrace{\frac{\partial(n^\alpha \langle \phi \rangle)}{\partial t}}_1 + \underbrace{\frac{\partial(n^\alpha \langle v_i^\alpha \phi \rangle)}{\partial x_i^\alpha}}_2 - n^\alpha \left(\underbrace{\langle \frac{\partial \phi}{\partial t} \rangle}_3 + \underbrace{\langle v_i^\alpha \frac{\partial \phi}{\partial x_i^\alpha} \rangle}_4 + \underbrace{\langle a_i^\alpha \frac{\partial \phi}{\partial v_i^\alpha} \rangle}_5 \right) = \underbrace{\int \phi \frac{\delta f^\alpha}{\delta t}}_6 \bigg|_{coll} dv^\alpha$$

and set ϕ equal to the kinetic energy, that is, $\phi = \frac{1}{2} m^\alpha v_j^\alpha v_j^\alpha$. Because of the independence of coordinates, the partial derivatives of ϕ with respect to t and x_i^α are both zero:

$$\frac{\partial \phi}{\partial t} = \frac{1}{2} m^\alpha \frac{\partial v_j^\alpha v_j^\alpha}{\partial t} = 0 \qquad \frac{\partial \phi}{\partial x_i^\alpha} = \frac{1}{2} m^\alpha \frac{\partial v_j^\alpha v_j^\alpha}{\partial x_i^\alpha} = 0$$

Therefore, Term 3 and Term 4 of the generalized equation of change are also both zero:

$$\underbrace{n^\alpha \langle \frac{\partial \phi}{\partial t} \rangle}_3 = n^\alpha \frac{1}{2} m^\alpha \underbrace{\langle \frac{\partial v_j^\alpha v_j^\alpha}{\partial t} \rangle}_{=0} = 0 \qquad \underbrace{n^\alpha \langle v_i^\alpha \frac{\partial \phi}{\partial x_i^\alpha} \rangle}_4 = n^\alpha \frac{1}{2} m^\alpha \underbrace{\langle v_i^\alpha \frac{\partial v_j^\alpha v_j^\alpha}{\partial x_i^\alpha} \rangle}_{=0} = 0$$

The partial derivative of ϕ with respect to v_i^α is

$$\frac{\partial \phi}{\partial v_i^\alpha} = \frac{1}{2} m^\alpha \frac{\partial (v_j^\alpha v_j^\alpha)}{\partial v_i^\alpha} = \begin{cases} 0 & i \neq j \\ \frac{1}{2} m^\alpha \frac{\partial (v_i^\alpha v_i^\alpha)}{\partial v_i^\alpha} & i = j \end{cases}$$

From the chain rule,

$$\frac{\partial (v_i^\alpha v_i^\alpha)}{\partial v_i^\alpha} = v_i^\alpha \frac{\partial v_i^\alpha}{\partial v_i^\alpha} + v_i^\alpha \frac{\partial v_i^\alpha}{\partial v_i^\alpha} = 2v_i^\alpha$$

which is just the familiar $d(v^2) = 2v dv$, so

$$\frac{\partial \phi}{\partial v_i^\alpha} = \frac{1}{2} m^\alpha \frac{\partial v_j^\alpha v_j^\alpha}{\partial v_i^\alpha} = \left(\frac{1}{2} m^\alpha \right) (2v_i^\alpha) = m^\alpha v_i^\alpha$$

The expectation values of ϕ and $v_i^\alpha \phi$ are

$$\langle \phi \rangle = \frac{1}{2} m^\alpha \langle v_j^\alpha v_j^\alpha \rangle \quad \langle v_i^\alpha \phi \rangle = \frac{1}{2} m^\alpha \langle v_i^\alpha v_j^\alpha v_j^\alpha \rangle$$

Substituting the values calculated above into the generalized equation of change transforms it to

$$\underbrace{\frac{\partial}{\partial t} \left(\frac{1}{2} n^\alpha m^\alpha \langle v_j^\alpha v_j^\alpha \rangle \right)}_1 + \underbrace{\frac{\partial}{\partial x_i^\alpha} \left(\frac{1}{2} n^\alpha m^\alpha \langle v_i^\alpha v_j^\alpha v_j^\alpha \rangle \right)}_2 - \underbrace{n^\alpha \langle m^\alpha a_i^\alpha v_i^\alpha \rangle}_5 = \underbrace{M_{coll}^\alpha}_6$$

where the new quantity M_{coll}^α , the exchange of energy due to collisions involving particles of species α , is defined by

$$M_{coll}^\alpha \equiv \frac{1}{2} m^\alpha \int v_j^\alpha v_j^\alpha \frac{\delta f^\alpha}{\delta t} dv^\alpha \quad (54)$$

We can decompose the velocity into its macroscopic and microscopic components, as in Equation 22, and substitute $v_i^\alpha = V_i^\alpha + u_i^\alpha$, for v_i^α in the equation of change. Using the relation for the product $\langle v_i^\alpha v_i^\alpha \rangle$ in Equation 27, the first term of the transformed equation of change becomes

$$\underbrace{\frac{\partial}{\partial t} \left(\frac{1}{2} n^\alpha m^\alpha \langle v_j^\alpha v_j^\alpha \rangle \right)}_1 = \underbrace{\frac{\partial}{\partial t} \left(\frac{1}{2} n^\alpha m^\alpha V_j^\alpha V_j^\alpha \right)}_{1a} + \underbrace{\frac{\partial}{\partial t} \left(\frac{1}{2} n^\alpha m^\alpha \langle u_j^\alpha u_j^\alpha \rangle \right)}_{1b}$$

From Equation 50, $\frac{1}{2} n^\alpha m^\alpha \langle u_j^\alpha u_j^\alpha \rangle = \frac{3}{2} n^\alpha T^\alpha$, so the first term can be written as

$$\underbrace{\frac{\partial}{\partial t} \left(\frac{1}{2} n^\alpha m^\alpha \langle v_j^\alpha v_j^\alpha \rangle \right)}_1 = \underbrace{\frac{\partial}{\partial t} \left(\frac{1}{2} n^\alpha m^\alpha V_j^\alpha V_j^\alpha \right)}_{1a} + \underbrace{\frac{\partial}{\partial t} \left(\frac{3}{2} n^\alpha T^\alpha \right)}_{1b}$$

where $n^\alpha T^\alpha = p^\alpha$ for an ideal gas.

The second term can be decomposed in a similar fashion using the expansion of the product $\langle v_i^\alpha v_j^\alpha v_j^\alpha \rangle$ in Equation 28.

$$\begin{aligned} \underbrace{\frac{\partial}{\partial x_i^\alpha} \left(\frac{1}{2} n^\alpha m^\alpha \langle v_i^\alpha v_j^\alpha v_j^\alpha \rangle \right)}_2 &= \frac{\partial}{\partial x_i^\alpha} \left\{ \frac{1}{2} n^\alpha m^\alpha (V_i^\alpha V_j^\alpha V_j^\alpha + 2 \langle u_i^\alpha u_j^\alpha \rangle V_j^\alpha + \langle u_j^\alpha u_j^\alpha \rangle V_i^\alpha + \langle u_i^\alpha u_j^\alpha u_j^\alpha \rangle) \right\} \\ &= \frac{\partial}{\partial x_i^\alpha} \left\{ \underbrace{\frac{1}{2} n^\alpha m^\alpha V_i^\alpha V_j^\alpha V_j^\alpha}_{2a} + \underbrace{n^\alpha m^\alpha \langle u_i^\alpha u_j^\alpha \rangle V_j^\alpha}_{2b} + \underbrace{\frac{1}{2} n^\alpha m^\alpha \langle u_j^\alpha u_j^\alpha \rangle V_i^\alpha}_{2c} + \underbrace{\frac{1}{2} n^\alpha m^\alpha \langle u_i^\alpha u_j^\alpha u_j^\alpha \rangle}_{2d} \right\} \end{aligned}$$

Term 2a is the gradient of the macroscopic transport of kinetic energy density at the mean velocity V_i^α :

$$\frac{\partial}{\partial x_i^\alpha} \left(\underbrace{\frac{1}{2} n^\alpha m^\alpha V_i^\alpha V_j^\alpha V_j^\alpha}_{2a} \right) = \frac{\partial}{\partial x_i^\alpha} \left(n^\alpha \underbrace{\frac{1}{2} m^\alpha (V^\alpha)^2}_{\text{Kinetic Energy}} V_i^\alpha \right)$$

Term 2b represents the work done by pressure, and Term 2c represents the macroscopic transport of microscopic (random thermal) energy at the mean velocity V_i^α . They can be written in terms of the pressure tensor $\psi_{ij}^\alpha \equiv n^\alpha m^\alpha \langle u_i^\alpha u_j^\alpha \rangle$. Substituting ψ_{ij}^α into Term 2b and swapping indices in Term 2c gives:

$$\frac{\partial}{\partial x_i^\alpha} \left(\underbrace{n^\alpha m^\alpha \langle u_i^\alpha u_j^\alpha \rangle V_j^\alpha}_{2b} + \underbrace{\frac{1}{2} n^\alpha m^\alpha \langle u_j^\alpha u_j^\alpha \rangle V_i^\alpha}_{2c} \right) = \frac{\partial}{\partial x_i^\alpha} \left(\psi_{ij}^\alpha V_j^\alpha + n^\alpha \underbrace{\frac{1}{2} m^\alpha \langle u_i^\alpha u_i^\alpha \rangle}_{\text{Thermal Energy}} V_j^\alpha \right)$$

Expanding $\psi_{ij}^\alpha = p^\alpha \delta_{ij} + \Pi_{ij}^\alpha$ as in the derivation of the moment equation and using the relationship

$\frac{1}{2} n^\alpha m^\alpha \langle u_i^\alpha u_i^\alpha \rangle = \frac{3}{2} p^\alpha \delta_{ij}$ from Equation 50, these two terms become

$$\begin{aligned} \frac{\partial}{\partial x_i^\alpha} \left(\underbrace{n^\alpha m^\alpha \langle u_i^\alpha u_j^\alpha \rangle V_j^\alpha}_{2b} + \underbrace{\frac{1}{2} n^\alpha m^\alpha \langle u_j^\alpha u_j^\alpha \rangle V_i^\alpha}_{2c} \right) &= \frac{\partial}{\partial x_i^\alpha} \left\{ (p^\alpha \delta_{ij} + \Pi_{ij}^\alpha) V_j^\alpha + \left(\frac{3}{2} p^\alpha \delta_{ij} \right) V_j^\alpha \right\} \\ &= \frac{\partial}{\partial x_i^\alpha} \left(\frac{5}{2} p^\alpha \delta_{ij} V_j^\alpha + \Pi_{ij}^\alpha V_j^\alpha \right) \end{aligned}$$

Contracting $\delta_{ij} V_j$ over the j index and substituting for p^α from the ideal gas law $p^\alpha = n^\alpha T^\alpha$ gives

$$\frac{\partial}{\partial x_i^\alpha} \left(\underbrace{n^\alpha m^\alpha \langle u_i^\alpha u_j^\alpha \rangle V_j^\alpha}_{2b} + \underbrace{\frac{1}{2} n^\alpha m^\alpha \langle u_j^\alpha u_j^\alpha \rangle V_i^\alpha}_{2c} \right) = \frac{\partial}{\partial x_i^\alpha} \left(\frac{5}{2} n^\alpha T^\alpha V_i^\alpha + \Pi_{ij}^\alpha V_j^\alpha \right)$$

Term 2d describes the transport of microscopic (random thermal) energy at the thermal velocity u_i^α . If we define the *heat flux vector* q_i to be

$$q_i^\alpha \equiv \frac{1}{2} n^\alpha m^\alpha \langle u_i^\alpha u_j^\alpha u_j^\alpha \rangle = n^\alpha \underbrace{\left\langle \frac{1}{2} m^\alpha u_j^\alpha u_j^\alpha \right\rangle}_{\text{Thermal Energy}} u_i^\alpha \quad (55)$$

as in Equation 1.21 in Braginskii [3:210], then Term 2d becomes

$$\frac{\partial}{\partial x_i^\alpha} \left(\underbrace{\frac{1}{2} n^\alpha m^\alpha \langle u_i^\alpha u_j^\alpha u_j^\alpha \rangle}_{2d} \right) = \frac{\partial q_i^\alpha}{\partial x_i^\alpha}$$

Term 5 represents the volumetric power density from the action of external forces. Substituting for the acceleration from Equation 30 we get

$$\underbrace{n^\alpha \langle m^\alpha a_i^\alpha v_i^\alpha \rangle}_5 = n^\alpha \langle m^\alpha \frac{\sum F_i^\alpha}{m^\alpha} v_i^\alpha \rangle = Z e n^\alpha \langle (E_i + \frac{1}{c} [\epsilon_{ijk} v_j^\alpha B_k]) v_i^\alpha \rangle =$$

Since the alternating unit tensor ϵ_{ijk} has the property that $\epsilon_{ijk} = -\epsilon_{jik}$, for every term $[\epsilon_{123} v_2^\alpha B_3] v_1^\alpha$, where 1, 2, and 3 represent some arbitrary assignment of the coordinates x , y , and z , there is a term $[\epsilon_{213} v_1^\alpha B_3] v_2^\alpha = -[\epsilon_{123} v_1^\alpha B_3] v_2^\alpha$ to cancel it. Therefore, $[\epsilon_{ijk} v_j^\alpha B_k] v_i^\alpha = 0$, and Term 5 becomes

$$\underbrace{n^\alpha \langle m^\alpha a_i^\alpha v_i^\alpha \rangle}_5 = Z e n^\alpha \langle E_i v_i^\alpha \rangle$$

Since E_i is not a function of velocity, it can come outside of the expectation value, so applying Equation 26, we are left with:

$$\underbrace{n^\alpha \langle m^\alpha a_i^\alpha v_i^\alpha \rangle}_5 = Z e n^\alpha E_i \langle v_i^\alpha \rangle = Z e n^\alpha E_i V_i^\alpha \quad (56)$$

Since $Z e n^\alpha V_i^\alpha$ is just J_i^α , the macroscopic electric current density in the i^{th} direction caused by particles of species α , Equation 56 is an expression for the $\mathbf{J} \cdot \mathbf{E}$ *Joule heating* of the plasma.

Term 6 represents the change in energy density due to collisions with particles of other species. The definition of M_{coll}^α in Equation 54 may be expanded using the velocity decomposition $v_i^\alpha = V_i^\alpha + u_i^\alpha$ from Equation 22 to get

$$\begin{aligned} M_{coll}^\alpha &\equiv \underbrace{\frac{1}{2} m^\alpha \int v_j^\alpha v_j^\alpha \bar{n}^\alpha \frac{\delta f^\alpha}{\delta t} \bigg|_{coll} d\mathbf{v}^\alpha}_6 = \frac{1}{2} m^\alpha \int (V_j^\alpha V_j^\alpha + 2V_j^\alpha u_j^\alpha + u_j^\alpha u_j^\alpha) \bar{n}^\alpha \frac{\delta f^\alpha}{\delta t} \bigg|_{coll} d\mathbf{v}^\alpha \\ &= \underbrace{\frac{1}{2} m^\alpha V_j^\alpha V_j^\alpha \int \bar{n}^\alpha \frac{\delta f^\alpha}{\delta t} \bigg|_{coll} d\mathbf{v}^\alpha}_{6a} + \underbrace{V_j^\alpha \int m^\alpha u_j^\alpha \bar{n}^\alpha \frac{\delta f^\alpha}{\delta t} \bigg|_{coll} d\mathbf{v}^\alpha}_{6b} + \underbrace{\frac{1}{2} m^\alpha \int u_j^\alpha u_j^\alpha \bar{n}^\alpha \frac{\delta f^\alpha}{\delta t} \bigg|_{coll} d\mathbf{v}^\alpha}_{6c} \end{aligned}$$

Term 6a contains S_{coll}^α as defined in Equation 44, and Term 6b contains R_j^α as defined in Equation 52. Rewriting the expression for M_{coll}^α in terms of these quantities gives

$$M_{coll}^\alpha = \frac{1}{2} m^\alpha V_j^\alpha V_j^\alpha S_{coll}^\alpha + V_j^\alpha R_j^\alpha + Q_{coll}^\alpha$$

where

$$Q_{coll}^\alpha \equiv \frac{1}{2} m^\alpha \int u_j^\alpha u_j^\alpha \frac{\delta f^\alpha}{\delta t} \bigg|_{coll} d\mathbf{v}^\alpha \quad (57)$$

defines the new quantity Q_{coll}^α , the thermal energy exchanged by the production or loss of particles of species α .

Collecting all of the transformations of the terms of the equation of change gives the *energy transport equation*:

$$\begin{aligned}
 \frac{\partial}{\partial t} \left(\underbrace{\frac{1}{2} n^\alpha m^\alpha V_j^\alpha V_j^\alpha}_{1} + \underbrace{\frac{3}{2} n^\alpha T^\alpha}_{2} \right) + \frac{\partial}{\partial x_i^\alpha} \left\{ \left(\underbrace{\frac{1}{2} n^\alpha m^\alpha V_j^\alpha V_j^\alpha}_{3} + \underbrace{\frac{5}{2} n^\alpha T^\alpha}_{4} \right) V_i^\alpha + \right. \\
 \left. + \left(\underbrace{\Pi_{ij}^\alpha V_j^\alpha}_{5} \right) + \underbrace{q_i^\alpha}_{6} \right\} = \underbrace{Z e n^\alpha E_i V_i^\alpha}_{7} + \underbrace{\frac{1}{2} m^\alpha V_j^\alpha V_j^\alpha S_{coll}^\alpha}_{8} + \underbrace{V_j^\alpha R_j^\alpha}_{9} + \underbrace{Q_{coll}^\alpha}_{10} \quad (58)
 \end{aligned}$$

where the overbraces mark the terms of the generalized equation of change and the underbraces the terms of the energy transport equation. This form of the energy transport equation appears in Braginskii [3:210] as Equation 1.20.

Appendix B. Collision Processes in Hydrogen Ion Sources

This appendix contains a listing of the primary reactions that can occur in a hydrogen plasma, grouped by the products produced and the reactants destroyed. In order to standardize reaction numbers with those used in the model, all entries, including reaction numbers \aleph and threshold energies ϵ_{th} , are based on the list in Smith and Glasser [32] except where cited. Reactions are listed in the order: e , H^- , H , H_2 , H^+ , H_2^+ , and H_3^+ . Reactions with the same first reactants are listed in the same order by the second reaction. For more specific information on reactions with fitted curves for cross sections and reaction rates, see Janev *et al.* [17].

B.1 Reactions That Release Electrons

\aleph	reaction	name	ϵ_{th}
7	$e + H^- \rightarrow e + H + e$	collisional detachment	0.75
19	$e + H \rightarrow e + H^+ + e$	ionization	13.6
3	$e + H_2(v=0) \rightarrow e + H^- + H^+$	polar dissociation	17.32
24	$e + H_2 \rightarrow e + H_2^+ + e$	ionization	15.4 [17:52]
20	$e + H_2^+ \rightarrow 2e + 2H^+$	dissociative ionization	16.243
8	$H^- + H \rightarrow e + 2H$	collisional detachment [11:32]	0.0 [17:230]
9	$H^- + H \rightarrow H_2(v=0) + e$	associative detachment	0.0 [17:230]
58	$H^- + H \rightarrow H_2(v=9) + e$	(inelastic) assoc. detach.	
10	$H^- + H_2 \rightarrow e + H + H_2$	collisional detachment	0.75
29	$H^- + H^+ \rightarrow e + H_2^+$	associative detachment	0.75 [17:222]
43	$H^- + H_2^+ \rightarrow e + H_3^+$	associative detachment	
31	$H + H \rightarrow e + H_2^+$	associative ionization [11:12]	
32	$H + H_2 \rightarrow e + H_3^+$	associative ionization [11:12]	

B.2 Reactions That Capture Electrons

N	reaction	name	ϵ_{th}
6	$e + H \rightarrow H^- + h\nu$	radiative attachment [11:43]	
1	$e + H_2(v=0) \rightarrow H^- + H$	dissociative attachment	3.4
2	$e + H_2(v=0) \rightarrow H^- + H^*$	dissoc. attach. (inelastic)	13.6
56	$e + H_2(v=9) \rightarrow H^- + H$	dissoc. attach. (superelastic)	0.1 [17:62]
26	$e + H^+ \rightarrow H + h\nu$	radiative recombination [11:47]	13.6 [17:32]
4	$e + H_2^+(v=0) \rightarrow H^- + H^+$	dissociative attachment	
16	$e + H_2^+ \rightarrow 2H$	dissociative recombination	0.33
17	$e + H_3^+ \rightarrow H_2 + H$	dissociative recombination	0.38
42	$e + H_3^+ \rightarrow H_2^+ + H^-$	dissociative recombination	

B.3 Reactions That Produce H^- Ions

N	reaction	name	ϵ_{th}
6	$e + H \rightarrow H^- + h\nu$	radiative capture	
1	$e + H_2(v=0) \rightarrow H^- + H$	dissociative attachment	3.4
2	$e + H_2(v=0) \rightarrow H^- + H^*$	dissoc. attachment (inelastic)	13.6
3	$e + H_2(v=0) \rightarrow e + H^- + H^+$	polar dissociation	17.32
56	$e + H_2(v=9) \rightarrow H^- + H$	dissociative attachment	
4	$e + H_2^+(v=0) \rightarrow H^- + H^+$	dissociative attachment	
42	$e + H_3^+ \rightarrow H_2^+ + H^-$	dissociative attachment	
22	$H + H \rightarrow H^- + H^+$	ion pair formation [11:10]	
30	$H + H_2 \rightarrow H^- + H_2^+$	ion pair formation [11:10]	
21	$H_2 + H_2^+ \rightarrow H^- + H^+ + H_2^+$	collisional dissociation	

B.4 Reactions That Destroy H^- Ions

N	reaction	name	ϵ_{th}
7	$e + H^- \rightarrow e + H + e$	collisional detachment	0.75
8	$H^- + H \rightarrow e + 2H$	collisional detachment [11:32]	0.0 [17:230]
9	$H^- + H \rightarrow H_2(v=0) + e$	associative detachment	0.0 [17:230]
58	$H^- + H \rightarrow H_2(v=9) + e$	associative detachment	
10	$H^- + H_2 \rightarrow e + H + H_2$	collisional detachment	0.75
11	$H^- + H^+ \rightarrow 2H$	mutual neutralization	
29	$H^- + H^+ \rightarrow e + H_2^+$	associative detachment	0.75 [17:222]
43	$H^- + H_2^+ \rightarrow H_3^+ + e$	associative detachment	
12	$H^- + H_2^+ \rightarrow H + H_2$	mutual neutralization	

B.5 Reactions That Produce H Atoms

N	reaction	name	ϵ_{th}
7	$e + H^- \rightarrow e + H + e$	collisional detachment	0.75
13	$e + H_2 \rightarrow 2H + e$	electronic dissociation	9.2
1	$e + H_2(v=0) \rightarrow H^- + H$	dissociative attachment	3.4
2	$e + H_2(v=0) \rightarrow H^- + H^*$	dissoc. attachment (inelastic)	13.6
56	$e + H_2(v=9) \rightarrow H^- + H$	dissoc. attachment (superelastic)	
26	$e + H^+ \rightarrow H + h\nu$	radiative capture	13.6 [17:32]
14	$e + H_2^+ \rightarrow H + H^+ + e$	electronic dissociation	3.45
16	$e + H_2^+ \rightarrow 2H$	dissociative recombination [11:49]	0.33
15	$e + H_3^+ \rightarrow e + H + H_2^+$	electronic dissociation	6.6
17	$e + H_3^+ \rightarrow H_2 + H$	dissociative recombination [11:49]	0.38
8	$H^- + H \rightarrow e + 2H$	collisional detachment [11:32]	0.0 [17:230]
10	$H^- + H_2 \rightarrow e + H + H_2$	collisional detachment	0.75

N	reaction	name	ϵ_{th}
11	$H^- + H^+ \rightarrow 2H$	mutual neutralization	1.83 [17:142] 0.0 [17:176]
12	$H^- + H_2^+ \rightarrow H + H_2$	mutual neutralization	
27	$H_2 + H^+ \rightarrow H_2^+ + H$	charge transfer [11:15]	
18	$H_2 + H_2^+ \rightarrow H + H_3^+$	ion rearrangement [11:31]	

B.6 Reactions That Destroy H Atoms

N	reaction	name	ϵ_{th}
19	$e + H \rightarrow e + H^+ + e$	ionization	13.6 0.0 [17:230]
6	$e + H \rightarrow H^- + h\nu$	radiative capture	
9	$H^- + H \rightarrow H_2(v=0) + e$	associative detachment	
58	$H^- + H \rightarrow H_2(v=9) + e$	assoc. detach. (inelastic)	
31	$H + H \rightarrow e + H_2^+$	associative ionization [11:12]	
22	$H + H \rightarrow H^- + H^+$	ion pair formation [11:10]	
32	$H + H_2 \rightarrow e + H_3^+$	associative detachment [11:33]	
30	$H + H_2 \rightarrow H^- + H_2^+$	ion pair formation [11:10]	
33	$H + H_3^+ \rightarrow H_2 + H_2^+$	ion rearrangement [11:31]	

B.7 Reactions That Produce H₂ Molecules

N	reaction	name	ϵ_{th}
40	$e + H_3^+ \rightarrow e + H_2 + H^+$	electronic dissociation	0.38 0.0 [17:230]
17	$e + H_3^+ \rightarrow H_2 + H$	dissociative recombination [11:49]	
9	$H^- + H \rightarrow H_2(v=0) + e$	associative detachment	
58	$H^- + H \rightarrow H_2(v=9) + e$	associative detachment (inelastic)	
12	$H^- + H_2^+ \rightarrow H + H_2$	mutual neutralization	
33	$H + H_3^+ \rightarrow H_2 + H_2^+$	ion rearrangement [11:31]	

B.8 Reactions That Destroy H_2 Molecules

N	reaction	name	ϵ_{th}
1	$e + H_2(v=0) \rightarrow H^- + H$	dissociative attachment	3.4
2	$e + H_2(v=0) \rightarrow H^- + H^*$	dissociative attachment	13.6
3	$e + H_2(v=0) \rightarrow e + H^- + H^+$	polar dissociation	17.32
56	$e + H_2(v=9) \rightarrow H^- + H$	dissociative attachment	
13	$e + H_2 \rightarrow 2H + e$	electronic dissociation	9.2
24	$e + H_2 \rightarrow e + H_2^+ + e$	ionization	15.4 [17:52]
30	$H + H_2 \rightarrow H^- + H_2^+$	ion pair formation [11:10]	
32	$H + H_2 \rightarrow e + H_3^+$	associative ionization [11:12]	
27	$H_2 + H^+ \rightarrow H_2^+ + H$	charge transfer [11:15]	1.83 [17:142]
18	$H_2 + H_2^+ \rightarrow H + H_3^+$	ion rearrangement [11:31]	0.0 [17:176]
21	$H_2 + H_2^+ \rightarrow H^- + H^+ + H_2^+$	collisional dissociation	

B.9 Reactions That Release H^+ Ions

N	reaction	name	ϵ_{th}
19	$e + H \rightarrow e + H^+ + e$	ionization	13.6
20	$e + H_2^+ \rightarrow 2e + 2H^+$	dissociative ionization	16.243
14	$e + H_2^+ \rightarrow H + H^+ + e$	electronic dissociation	3.45
4	$e + H_2^+(v=0) \rightarrow H^- + H^+$	dissociative attachment	
40	$e + H_3^+ \rightarrow e + H_2 + H^+$	electronic dissociation	
22	$H + H \rightarrow H^- + H^+$	ion pair formation [11:10]	
21	$H_2 + H_2^+ \rightarrow H^- + H^+ + H_2^+$	collisional dissociation	

B.10 Reactions That Capture H^+ Ions

N	reaction	name	ϵ_{th}
26	$e + H^+ \rightarrow H + h\nu$	radiative capture	13.6 [17:32]
29	$H^- + H^+ \rightarrow e + H_2^+$	associative detachment	0.75 [17:222]
11	$H^- + H^+ \rightarrow 2H$	mutual neutralization	
27	$H_2 + H^+ \rightarrow H_2^+ + H$	charge transfer [11:15]	1.83 [17:142]

B.11 Reactions That Produce H_2^+ Ions

N	reaction	name	ϵ_{th}
24	$e + H_2 \rightarrow e + H_2^+ + e$	ionization	15.4 [17:52]
15	$e + H_3^+ \rightarrow e + H + H_2^+$	electronic dissociation	6.6
42	$e + H_3^+ \rightarrow H_2^+ + H^-$	dissociative attachment	
29	$H^- + H^+ \rightarrow e + H_2^+$	associative detachment	0.75 [17:222]
31	$H + H \rightarrow e + H_2^+$	associative ionization [11:12]	
30	$H + H_2 \rightarrow H^- + H_2^+$	ion pair formation [11:10]	
33	$H + H_3^+ \rightarrow H_2 + H_2^+$	ion rearrangement [11:31]	
27	$H_2 + H^+ \rightarrow H_2^+ + H$	charge transfer [11:15]	1.83 [17:142]

B.12 Reactions That Destroy H_2^+ Ions

N	reaction	name	ϵ_{th}
20	$e + H_2^+ \rightarrow 2e + 2H^+$	dissociative ionization	16.243
14	$e + H_2^+ \rightarrow H + H^+ + e$	electronic dissociation	3.45
4	$e + H_2^+ (v=0) \rightarrow H^- + H^+$	dissociative attachment	
16	$e + H_2^+ \rightarrow 2H$	dissociative recombination [11:49]	0.33
12	$H^- + H_2^+ \rightarrow H + H_2$	mutual neutralization	

N	reaction	name	ϵ_{th}
43	$H^- + H_2^+ \rightarrow H_3^+ + e$		
18	$H_2 + H_2^+ \rightarrow H + H_3^+$	ion rearrangement [11:25]	0.0 [17:176]

B.13 Reactions That Produce H_3^+ Ions

N	reaction	name	ϵ_{th}
43	$H^- + H_2^+ \rightarrow H_3^+ + e$		
32	$H + H_2 \rightarrow e + H_3^+$	associative ionization [11:12]	
18	$H_2 + H_2^+ \rightarrow H + H_3^+$	ion rearrangement [11:25]	0.0 [17:176]

B.14 Reactions That Destroy H_3^+ Ions

N	reaction	name	ϵ_{th}
15	$e + H_3^+ \rightarrow e + H + H_2^+$	electronic dissociation	6.6
40	$e + H_3^+ \rightarrow e + H_2 + H^+$	electronic dissociation	
42	$e + H_3^+ \rightarrow H_2^+ + H^-$	dissociative recombination	
17	$e + H_3^+ \rightarrow H_2 + H$	dissociative recombination [11:49]	0.38
33	$H + H_3^+ \rightarrow H_2 + H_2^+$	ion rearrangement [11:25]	

B.15 Elastic Scattering Reactions

#	reaction	name	ϵ_{th}
48	$e + H \rightarrow e + H$	elastic scattering	0.0
34	$e + H_2 \rightarrow e + H_2$	elastic scattering	0.0
50	$H^- + H \rightarrow H^- + H$	elastic scattering	0.0
5	$H^- + H \rightarrow H + H^-$	charge exchange	0.0 [17:228]
35	$H^- + H_2 \rightarrow H^- + H_2$	elastic scattering	0.0
25	$H^- + H^+ \rightarrow H^+ + H^-$	double charge exchange	

N	reaction	name	ϵ_{th}
53	$H + H \rightarrow H + H$	elastic scattering	0.0
47	$H + H_2 \rightarrow H + H_2$	elastic scattering	0.0
49	$H + H^+ \rightarrow H + H^+$	elastic scattering	0.0
23	$H + H^+ \rightarrow H^+ + H$	charge exchange	0.0 [17:128]
51	$H + H_2^+ \rightarrow H + H_2^+$	elastic scattering	0.0
52	$H + H_3^+ \rightarrow H + H_3^+$	elastic scattering	0.0
46	$H_2 + H_2 \rightarrow H_2 + H_2$	elastic scattering	0.0
36	$H_2 + H^+ \rightarrow H_2 + H^+$	elastic scattering	0.0
44	$H_2 + H_2^+ \rightarrow H_2 + H_2^+$	elastic scattering	0.0
28	$H_2 + H_2^+ \rightarrow H_2^+ + H_2$	charge transfer	
45	$H_2 + H_3^+ \rightarrow H_2 + H_3^+$	elastic scattering	0.0

B.16 Excitation and De-excitation Reactions

#	reaction	name	ϵ_{th}
37	$e + H_2(v=0) \rightarrow e + H_2(v=1)$	vibrational excitation	0.5 [17:34]
38	$e + H_2(v=0) \rightarrow e + H_2(v=2)$	vibrational excitation	1 [17:36]
39	$e + H_2(v=0) \rightarrow e + H_2(v=3)$	vibrational excitation	1.45
54	$e + H_2(v=0) \rightarrow e + H_2(v=9)$	vibrational excitation	
55	$e + H_2(v=0) \rightarrow H_2^-(C, B)$		
	$\rightarrow e + H_2(v=9) + h\nu$	vibrational excitation	
57	$e + H_2(v=9) \rightarrow e + H_2(v=0)$	vibrational de-excitation	
41	$e + H(1s) \rightarrow e + H(2\ell)$	electronic excitation	10.2 [17:18]

Appendix C. Glossary of Variables

C.1 Roman Letters

variable	Significance
A	Arbitrary or normalization constant. Momentum exchanged due to collisions: $A_j^\alpha \equiv m^\alpha v_j^\alpha S_{coll}^\alpha$.
B	Magnitude of the magnetic filter field.
c	Speed of light.
d	Drag: $d^\alpha = n^\alpha m^\alpha \nu^{\alpha n}$, $d = \frac{d^e d^i}{mn}$.
e	Electron charge. (Superscript) Electron: <i>E.g.</i> , T^e , Γ^e .
E	Electric field.
f	Probability distribution function for a single particle.
H	Magnetic intensity: $\mu H_i = B_i$.
i	(Subscript) First index: <i>E.g.</i> , $v_i v_j$. (Superscript) Ion: <i>E.g.</i> , T^i , Γ^i .
j	(Subscript) Second index: <i>E.g.</i> , $v_i v_j$. (Subscript) Integration bin number: <i>E.g.</i> , T_{j+1} .
J	Current density: The current density in the i^{th} direction is $J_i = Z e n^\alpha V_i^\alpha$.
k	Reaction rate: $k_R \equiv \langle \sigma_R v \rangle$. (Subscript) Third index.
ℓ	Dimension of length.
m	Mass: $m \equiv m^e + m^i$.
M	Energy exchange due to collisions: $M_{coll}^\alpha \equiv \frac{1}{2} m^\alpha \int v_j^\alpha v_j^\alpha \frac{\delta f^\alpha}{\delta t} \bigg _{coll} d\mathbf{v}^\alpha$.

variable	Significance
n	Density $n^\alpha(\mathbf{x}, t)$ at point \mathbf{x} and time t : $n^\alpha(\mathbf{x}, t) = \int \bar{n}^\alpha f^\alpha(\mathbf{v}, \mathbf{x}, t) d\mathbf{v}^\alpha$. Average density: $\bar{n}^\alpha = N^\alpha / \mathcal{V}$.
N	Number of particles.
p	Pressure: $p^\alpha = n^\alpha T^\alpha$ for an ideal gas.
\mathcal{P}	General polynomial: $\mathcal{P}(x^\alpha)$.
q	Heat flux tensor: $q_i^\alpha \equiv \frac{1}{2} n^\alpha m^\alpha \langle u_i^\alpha u_j^\alpha u_j^\alpha \rangle$.
Q	Thermal energy exchange due to collisions: $Q_{coll}^\alpha \equiv \frac{1}{2} m^\alpha \int u_j^\alpha u_j^\alpha \bar{n}^\alpha \frac{\delta f^\alpha}{\delta t} \bigg _{coll} d\mathbf{v}^\alpha$.
R	Momentum exchanged due to collisions: $R_j^\alpha \equiv \int m^\alpha u_j^\alpha \bar{n}^\alpha \frac{\delta f^\alpha}{\delta t} \bigg _{coll} d\mathbf{v}^\alpha$.
S	Net production of particles through collisions: $S_{coll}^\alpha \equiv \int \bar{n}^\alpha \frac{\delta f^\alpha}{\delta t} \bigg _{coll} d\mathbf{v}^\alpha$.
t	Time.
T	Temperature (in units of energy).
u	Random (thermal, microscopic) velocity.
v	Total velocity: $v_i = V_i + u_i$.
V	Average (drift) velocity.
\mathcal{V}	Total volume.
x	Argument to general polynomial $\mathcal{P}(x^\alpha)$: $x^\alpha \equiv \omega^\alpha \tau^\alpha$. Coordinate direction of magnetic filter field.
y	Coordinate direction perpendicular to x and z .
z	Axial coordinate direction.
Z	Charge state: $Z = -1$ for electrons, and $Z = +1$ for positive ions.

C.2 Greek and Hebrew Letters

variable	Significance
α	First general species.
β	Second general species.
Γ	Particle flux: $\Gamma_i^\alpha \equiv n^\alpha V_i^\alpha$. Gamma function: $\Gamma(\zeta) \equiv \int_0^\infty t^{(\zeta-1)} e^{-t} dt$.
δ	Kronecker delta function δ_{ij} .
ϵ	Alternating unit tensor ϵ_{ijk} .
ε	Energy.
ζ	General function.
η	Coefficient of viscosity: $\eta^\alpha = n^\alpha T^\alpha \tau^\alpha (\mathcal{P}(x^\alpha))$.
κ	Coefficient of thermal conductivity: $\kappa^\alpha = \frac{n^\alpha T^\alpha \tau^\alpha}{m^\alpha} (\mathcal{P}(x^\alpha))$.
λ	Mean free path: $\lambda_{\text{mfp}} = \frac{1}{n^\alpha \sigma_N}$.
μ	Magnetic susceptibility: $\mu H_i = B_i$.
ν	Collision frequency: $\nu^\alpha \equiv \frac{1}{\tau^\alpha}$.
π	Ratio of circumference of a circle to its diameter.
Π	Viscosity stress tensor: $\Pi_{ij}^\alpha = \psi_{ij}^\alpha - p^\alpha \delta_{ij}$.
σ	Collision cross section.
τ	Time between collisions: $\tau^\alpha \equiv \frac{1}{\nu^\alpha}$.
ϕ	Generalized power of the velocity: $\phi = 1$, $\phi = mv$, and $\phi = \frac{1}{2}mv^2$.
Φ	Electrical potential.
χ	Alternative symbol for κ .
ψ	Pressure tensor: $\psi_{ij}^\alpha \equiv n^\alpha m^\alpha \langle u_i^\alpha u_j^\alpha \rangle$.
ω	Gyrofrequency of species α : $\omega_c^\alpha = \frac{eB}{m^\alpha c}$.
\aleph	Unspecified reaction number: <i>E.g.</i> , k_N .

Bibliography

1. Bailey, Wm. F. and R. G. Jones. "Electron Energy Distributions in Magnetic Multicusp Hydrogen Discharges." *Production and Neutralization of Negative Ions and Beams Fourth International Symposium*, 16-25. New York: American Institute of Physics Conference Proceeding No. 158, 1987.
2. Bell, 2Lt David E. *A Moment Approach to Modeling Negative Ion Sources*. MS thesis, AFIT/GEP/ENP/87D-2. School of Engineering, Air Force Institute of Technology (AU), Wright-Patterson AFB OH, December 1987 (AD-A1888858).
3. Braginskii, S. I. "Transport Processes in a Plasma." *Reviews of Plasma Physics*, 1: 205-311 (1965).
4. Bruneteau Mordin, Anne Marie. *Etude sur L'ion Negatif D'Hydrogene Dans des Decharges à Basse Pression*. Ph.D. dissertation. Université de Paris-Sud (Centre d'Orsay), July 1983 (Orsay order number 2740). (In French.)
5. Carlson, Neil, and Keith Miller. "DIRK 2—A Solver for Linearly Implicit Systems of O. D. E.'s Using a Diagonally Implicit Runge-Kutta Method of Order 2." Revision 2.2. Berkeley: University of California Department of Mathematics, September 1984.
6. Cercignani, Carlo. *Applied Mathematical Sciences, Vol. 67: The Boltzmann Equation and Its Applications*. New York: Springer Verlag, 1988 (ISBN 0-387-96637-4).
7. Chan, Chun Fai, C. F. Burrell, and William S. Cooper. "Model of Positive Ion Sources for Neutral Beam Injection." *Journal of Applied Physics*, 54: 6119-6137 (November 1983).
8. Ehlers, K. W., and K. N. Leung. "Further Study on a Magnetically Filtered Multicusp Ion Source." *Review of Scientific Instruments*, 53: 1423-1428 (September 1982).
9. Glasser, Alan H., and Kenneth Smith. "POS—A 1-D Time-Dependent H^+ Ion Source Code." *Computer Physics Communications*, 55: 409-424 (1989).
10. Golant, Viktor Evgen'evich, Aleksei Petrovich Zhilinskiĭ, and Igor Evgen'evich Sakharov. *Fundamentals of Plasma Physics*. New York: John Wiley and Sons, 1980 (ISBN 0-471-04593-4). (Translation of *Osnovy Fiziki Plazmy*, Izdatel'stvo Atomizdat, 1977. Translated by K. Z. Vedeneyeva and V. F. Agranat. Translation edited by Sanborn C. Brown.)
11. Green, S. A., and T. D. Wyatt. *Atomic and Space Physics*. New York: Addison Wesley, 1968. (Citations are not to page numbers but to the equation numbers of Table 1, pp. 156-157, in Chapter 3, "Solar-Terrestrial Relations.")
12. Hagen, O. F., and P. R. W. Henkes. "A Surface Conversion Source of H^- with Hot Walls and Variable Converter Temperature." *Production and Neutralization of Negative Ions and Beams Fourth International Symposium*, 384-394. New York: American Institute of Physics Conference Proceeding No. 158, 1987.
13. Hilbun, Capt William M. *Electron Kinetic Studies Utilizing the Solution of the Time-Dependent Collisional Boltzmann Equation*. MS Thesis, AFIT/GEP/ENP/90D-1. School of Engineering, Air Force Institute of Technology (AU), Wright-Patterson AFB OH, 1990 (AD-A230753).
14. Hiskes, J. R. "Review of Processes in the Theory of Volume Production." *Production and Neutralization of Negative Ions and Beams Fourth International Symposium*, 2-15. New York: American Institute of Physics Conference Proceeding No. 158, 1987.

15. —. "Electron Excitation of $H_2(v'')$ Levels to Yield Vibrationally Excited H_2 Molecules." *Production and Neutralization of Negative Ions and Beams Fourth International Symposium*, 32-36. New York: American Institute of Physics Conference Proceeding No. 158, 1987.
16. Holt, E. H., and R. W. Haskell. *Foundations of Plasma Dynamics*. New York: The Macmillan Company, 1965.
17. Janev, Ratko K., William D. Langer, Kenneth Evans, Jr., and Douglass E. Post, Jr. *Elementary Processes in Hydrogen-Helium Plasmas: Cross Sections and Reaction Rate Coefficients*. Heidelberg: Springer Verlag, 1987 (ISBN 0-387-17588-1).
18. Johnson, Jeremy David. *Characteristics of a Multipole Volume H^- Plasma*. Ph.D. dissertation. University of Aston, Birmingham, England, October 1987.
19. Jones, Capt Ricky G. *Plasma Transport in a Magnetic Multicusp Negative Hydrogen Ion Source*. Ph.D. Dissertation. School of Engineering, Air Force Institute of Technology (AU), Wright-Patterson AFB OH, 1991.
20. Koch, C. and G. Matthieussent. "Collisional Diffusion of a Plasma in Multipolar and Picket Fence Devices." *Phys. Fluids*, 26: 545-555 (February 1983).
21. Krall, Nicholas A., and Alvin W. Trivelpiece. *Principles of Plasma Physics*. San Francisco: San Francisco Press, Inc., 1986 (reprint—ISBN 0-911302-58-1).
22. Leung, K. N. "Self-Extraction Negative Ion Source." *Review of Scientific Instruments*, 53: 803-809 (1982).
23. —, K. W. Ehlers, and M. Bacal. "Extraction of Volume-Produced H^- Ions from a Multicusp Source." *Review of Scientific Instruments*, 54: 56-61 (January 1983).
24. —, K. W. Ehlers, and L. V. Pyle. "Optimization of H^- Production in a Magnetically Filtered Multicusp Source." *Review of Scientific Instruments*, 56: 364-368 (March 1985).
25. —. "Ion Source Development at Lawrence Berkeley Laboratory." Supplement to the *Proceedings of the Fourteenth Symposium on Ion Sources and Ion-Assisted Technology (ISIAT '91)*, edited by Toshinori Tagaki.
26. McAdams, R., A. J. T. Holmes, M. P. S. Nightingale, L. M. Lea, M. D. Hinton, A. F. Newman, T. S. Green. "The Production and Formation of Intense H^- Beams." *Production and Neutralization of Negative Ions and Beams Fourth International Symposium*, 298-308. New York: American Institute of Physics Conference Proceeding No. 158, 1987.
27. Minor, Capt Bryan. Unpublished work toward a Ph.D. degree in physics. School of Engineering, Air Force Institute of Technology, Wright-Patterson AFB OH, 1991.
28. Prokhorov, A. M. (ed.) *Sovetskii Entsiklopedicheski Slovar'*. Moscow: Izdatel'stvo "Sovetskaya Entsiklopediya," 1987. (In Russian.)
29. Rumer, Yu. B., and M. Sh. Ryvkin. *Thermodynamics, Statistical Physics, and Kinetics*. Moscow: Mir Publishers, 1980. (Translation from the Russian by S. Semyonov of *Termodinamika, Statisticheskaya Fizika, i Kinetika*. Moscow: Izdatel'stvo "Nauka," 1977.)
30. Seger, Capt Gaylord E., III. *A Numerical Solution of the Time-Dependent Boltzmann Equation*. MS Thesis, AFIT/GEP/ENP/89D-10. School of Engineering, Air Force Institute of Technology (AU), Wright-Patterson AFB OH, 1989. AD-A216397.
31. Seidl, M., W. E. Carr, J. L. Lopes, S. T. Melnychuk, and G. S. Tompa. "Surface Production of Negative Hydrogen Ions by Hydrogen and Cesium Ion Bombardment." *Production and Neutralization of Negative Ions and Beams Fourth International Symposium*, 432-445. New York: American Institute of Physics Conference Proceeding No. 158, 1987.

32. Smith, Kenneth, and Alan H. Glasser. "Data Base of Cross Sections and Reaction Rates for Hydrogen Ion Sources." *Computer Physics Communications*, 54: 391-407 (1989).
33. Stevens, Ralph R., Jr., R. L. York, K. N. Leung, K. W. Ehlers. "Operation of a Magnetically Filtered Multicusp Volume Source." *Production and Neutralization of Negative Ions and Beams Fourth International Symposium*, 271-281. New York: American Institute of Physics Conference Proceeding No. 158, 1987.
34. Stutzin, Geoffrey Carlos. "Spectroscopic Measurement of $H(1S)$ and $H_2(v'', J'')$ in an H^- Ion Source Plasma." Ph.D. dissertation. Department of Physics, University of California, Berkeley and Accelerator and Fusion Research Division, Lawrence Berkeley Laboratory, University of California, Berkeley, CA 94720, August 1990 (Lawrence Berkeley Laboratory report LBL-30541).
35. Vitko, Capt Todd R. *A Handbook of pos*. Unpublished Masters report. School of Engineering (Department of Physics), Air Force Institute of Technology (AU), Wright-Patterson AFB OH, 1992.

Vita

Vita brevis est, sed aeternitas sempiterna erit. Pro utra vivas?

Born in Hillsboro, Oregon, on 11 March 1959, Captain Vitko attended public schools in southwest Portland. He graduated from the Air Force Academy on 27 May 1981 with a Bachelor of Science degree in physics, a commission as a second lieutenant, and the Eagle and Fledgelings award for the outstanding cadet in the Russian language. Capt Vitko graduated from Undergraduate Navigator Training (UNT) in February 1982 and from KC-135 Combat Crew Training School (CCTS) in July 1982. He served as a KC-135A navigator and instructor navigator for the 924 Air Refueling Squadron (SAC) at Castle AFB, California, from July of 1982 through November of 1985, and as an EC-135 navigator, instructor navigator, assistant flight commander, and chief of current operations at the 10th Airborne Command and Control Squadron (USAFE) at RAF Mildenhall, England, from December 1985 to April 1990. He married Ruth Walker of Farmland, Indiana on 30 December 1990.

Capt Vitko arrived at the Air Force Institute of Technology in May of 1990 and graduated with a Master of Science degree in physics in March of 1992.

Permanent address: P.O. Box 205
Irvine, Kentucky 40336

REPORT DOCUMENTATION PAGE			Form Approved OMB No. 0704-0188	
<small>Public reporting burden for this collection of information is estimated to average 1 hour per response, including the time for reviewing instructions, searching existing data sources, gathering and maintaining the data needed, and completing and reviewing the collection of information. Send comments regarding this burden estimate or any other aspect of this collection of information, including suggestions for reducing this burden, to Washington Headquarters Services, Directorate for Information Operations and Reports, 1215 Jefferson Davis Highway, Suite 1204, Arlington, VA 22202-4302, and to the Office of Management and Budget, Paperwork Reduction Project (0704-0188), Washington, DC 20503.</small>				
1. AGENCY USE ONLY (Leave blank)		2. REPORT DATE March 1992		3. REPORT TYPE AND DATES COVERED Master's Thesis
4. TITLE AND SUBTITLE NUMERICAL ANALYSIS OF PLASMA TRANSPORT IN TANDEM VOLUME MAGNETIC MULTICUSP ION SOURCES			5. FUNDING NUMBERS	
6. AUTHOR(S) Todd R. Vitko, Captain, USAF				
7. PERFORMING ORGANIZATION NAME(S) AND ADDRESS(ES) Air Force Institute of Technology, WPAFB OH 45433-6583			8. PERFORMING ORGANIZATION REPORT NUMBER AFIT/GEP/ENP/92M-01	
9. SPONSORING / MONITORING AGENCY NAME(S) AND ADDRESS(ES) DR ALAN GARSCADDEN WL/POOC-3 WPAFB OH 45433			10. SPONSORING / MONITORING AGENCY REPORT NUMBER	
11. SUPPLEMENTARY NOTES				
12a. DISTRIBUTION / AVAILABILITY STATEMENT Approved for public release; distribution unlimited.			12b. DISTRIBUTION CODE	
13. ABSTRACT (Maximum 200 words) A one-dimensional fluid model of plasma transport in tandem volume magnetic multicusp ion sources is explored. The model, the positive ion source code <u>pos</u> , by Glasser and Smith, calculates plasma density, drift velocity, electron temperature, and ion temperature in an ion source. The usefulness of the model is limited: (1) The plasma density trend runs opposite to experimental results, and electron temperatures are an order of magnitude higher than experimentally observed. (2) Simplification of the reaction chemistry leads to a plasma balance between ionization and outflow instead of the correct balance between ionization and recombination. (3) Wall losses are neglected. (4) There are inconsistencies in the derivations of some equations. (5) The final solution depends on the choice of an initial estimated solution. (6) Results of the model are not totally reproducible. (7) Numerical instabilities develop upon modification of terms or variation of initial conditions outside of a narrow range. Calculations of the plasma potential from the results of the model are qualitatively correct.				
14. SUBJECT TERMS Boltzmann Equation, Ion Sources, Plasma Simulation, Electron Temperature, Plasma Density, Ion Temperature, Hydrogen Ions, Magnetic Filters, Hydrogen Plasma Chemistry			15. NUMBER OF PAGES 134	
			16. PRICE CODE	
17. SECURITY CLASSIFICATION OF REPORT Unclassified	18. SECURITY CLASSIFICATION OF THIS PAGE Unclassified	19. SECURITY CLASSIFICATION OF ABSTRACT Unclassified	20. LIMITATION OF ABSTRACT UL	